POLITECNICO
MILANO 1863

Scalable Adaptive Simulation of Organic Thin-Film Transistors

Doctoral Dissertation of
Pasquale Claudio Africa

Supervisor:
Carlo de Falco

Chair of the Ph.D. Programme:
Irene Maria Sabadini

Ph.D. Programme:
Mathematical Models and Methods in Engineering
XXXI cycle

Department of Mathematics
Politecnico di Milano

Table of contents

Table of contents

List of acronyms

AC Alternating Current

ADR Advection-Diffusion-Reaction

BTE Boltzmann Transport Equation

BiCGSTAB Bi-Conjugate Gradient STABilized

CF Capacitance-Frequency

CG Conjugate Gradient

CSR Compressed Sparse Row

CV Capacitance-Voltage

DD Drift-Diffusion

DNA Deoxyribonucleic Acid

DOS Density of States

ECDM Extended Correlated Disorder Model

EGDM Extended Gaussian Disorder Model

FET Field-Effect Transistor

FVSG Finite-Volume Scharfetter-Gummel

GMRES Generalized Minimal Residual

HOMO Highest Occupied Molecular Orbital

HPC High Performance Computing

IV Current-Voltage

List of acronyms

LUMO Lowest Unoccupied Molecular Orbital

MIS Metal-Insulator-Semiconductor

MNA Modified Nodal Analysis

NLP Non-Linear Poisson

ODE Ordinary Differential Equation

OLED Organic Light-Emitting Diode

OPV Organic Photovoltaics

OTFT Organic Thin-Film Transistor

P(NDI2OD-T2) Poly{[N,N'-bis(2-octyldodecyl)-naphthalene-1,4,5,8-bis(dicarboximide)-2,6-diyl]-alt-5,5'-(2,2'-bithiophene)}

PBTTT Poly(2,5-bis(3-tetradecylthiophen-2-yl)thieno[3,2-b]thiophene)

PDE Partial Differential Equation

PMMA Poly(methyl methacrylate)

RFID Radio-Frequency Identification

TFQMR Transpose-Free Quasi-Minimal Residual

List of figures

List of listings

Abstract

The present research project focuses on mathematical models and numerical methods for the simulation of Organic Thin-Film Transistors (OTFTs), which are Field-Effect Transistors (FETs) produced by depositing thin films of an organic semiconductor layer over a non-conducting substrate, such as glass, and are being adopted in the development of technological products such as flexible displays, integrated circuits, sensors, memories and e-paper.

The discovery of electrical conduction properties of a class of organic materials represents a potential breakthrough opening the way to a plethora of highly innovative products taking advantage of the peculiar properties of such semiconductors, including the ability of being produced at a low cost and deposited on flexible substrates and bio-compatibility.

The disordered morphology and energetic structure of organic semiconductor materials warrants for the development of suitable mathematical models and numerical methods for dealing with the peculiar properties of charge transport in OTFTs. Furthermore, the typically extreme form-factors of such devices constitute a challenge for numerical simulations which demands for an efficient implementation based on advanced High Performance Computing (HPC) techniques.

We develop a hierarchy of mathematical models based on Partial Differential Equations (PDEs) to describe charge transport in OTFTs. The basis of such model hierarchy is the well known Drift-Diffusion (DD) system of equations suitably adapted and extended in order to account for physical phenomena, such as energy barrier lowering and charge injection at metal-semiconductor interfaces, and state-of-the-art constitutive relations that are representative of the molecular disorder of organic semiconductor materials. A particular attention has been devoted to ensure that the presented models provide a consistent representation of the simulated system under equilibrium, transient and time harmonic regimes of operation. The models are firstly presented in a one-dimensional framework to derive a computationally efficient parameter estimation procedure used to characterize relevant physical properties of such materials. Then they are extended to 2D and 3D geometries in order to account in a more natural way for a set of inherently multi-dimensional phenomena such as the non-planarity of semiconductor-insulator interfaces due to the solution processing of the materials, par-

Abstract

asitic capacitances due to coupling between metal layers, the bending of energy bands at the semiconductor-substrate interface away from contacts and the contact resistance due to current-crowding effects.

Robust numerical methods are required to simulate the above described models. We propose a one-dimensional numerical formulation based on a modification of the Scharfetter-Gummel discretization scheme that is thermodynamically consistent even in those cases where the classical Einstein relation between the mobility and the diffusivity coefficient does not hold. Then the formulation is extended to meshes of quadtrees (2D) and octrees (3D), that are hierarchical, non-conforming Cartesian grids, by developing a strictly monotone discretization scheme that guarantees non-negative and oscillation-free solutions for problems with steep boundary and interior layers. To increase the accuracy of the numerical scheme we construct difference formulas that enable to recover higher order approximations of the solution gradient and the solution itself: the recovered gradient and solution are exploited to build proper *a posteriori* error estimators to drive a metric-based mesh adaptation procedure. The advantages of the proposed approach in terms of efficiency with respect to a standard solve-mark-refine technique are discussed. Finally, the properties of a set of robust linearization methods are investigated, with a special focus on those preserving the positivity of density variables throughout the simulation algorithm.

From an implementation perspective, recent progresses in data structures and algorithms for creating, hierarchically refining, balancing and partitioning meshes of quad- and oct-trees has brought this class of grids to the forefront of the research interests in the HPC community as a key tool for attaining extreme scalability. Achieving this goal drives the development of an efficient, parallel, scalable code. The implementation strategies followed in our code will be examined and motivated.

The formulation of state-of-the-art physical models and their interpretation was led with the support of Prof. Dario Natali of the Department of Electronics, Information and Bioengineering (DEIB), while the derivation of the discretization scheme on quadtrees and the definition of the mesh adaptation algorithms were developed in collaboration with Prof. Simona Perotto of the Department of Mathematics of Politecnico di Milano. We also acknowledge researchers from the Center of Nano Science and Technology of the Italian Institute of Technology (IIT) for collecting and providing experimental measurements used to validate the mathematical models presented.

Keywords: organic thin-film transistor; organic semiconductors; charge transport; Schottky barrier; charge injection; Einstein relation; drift-diffusion; Scharfetter-Gummel; hpc; scalability; quadtree; mesh adaptation

16

Sommario

Il presente progetto di ricerca ha come oggetto di studio modelli matematici e metodi numerici per la simulazione di Transistor Organici a Film Sottile (OTFT), che sono transistor a effetto di campo prodotti depositando pellicole sottili di un semiconduttore organico su un sottostrato composto da materiale isolante, ad esempio il vetro, e che vengono adottati nello sviluppo di prodotti tecnologici come display flessibili, circuiti integrati, sensori, memorie e carta elettronica.

La scoperta di proprietà di conduttività elettrica in una classe di materiali organici in anni recenti ha rappresentato un importante passo verso lo sviluppo di prodotti altamente innovativi che beneficiano di peculiarità di tali semiconduttori come la possibilità di essere prodotti a basso costo, deposti su supporti flessibili e la loro biocompatibilità.

La morfologia disordinata e la struttura energetica di semiconduttori organici giustifica lo sviluppo di modelli matematici e metodi numerici che opportunamente tengano conto delle proprietà fisiche del trasporto di carica negli OTFT. Inoltre, i rapporti di forma tipicamente estremi di tali dispositivi costituiscono una sfida computazionale per le simulazioni numeriche, esigendo dunque un'implementazione efficiente basata su tecniche avanzate di High Performance Computing (HPC).

Verrà presentata una gerarchia di modelli matematici a derivate parziali per descrivere il trasporto di carica negli OTFT. Tali modelli si basano sul sistema Drift-Diffusion (DD), propriamente adattato ed esteso al fine di tener conto di fenomeni fisici, tra cui l'abbassamento di barriera e l'iniezione di carica in corrispondenza di interfacce metallo-semiconduttore, e relazioni costitutive corrispondenti allo stato dell'arte che sono rappresentativi del disordine molecolare tipico dei semiconduttori organici. Un'attenzione particolare è stata rivolta a garantire che i modelli presentati forniscano una rappresentazione consistente del sistema simulato nei diversi regimi di funzionamento di equilibrio, transitorio e in frequenza. I modelli saranno dapprima presentati in un contesto monodimensionale per derivare un algoritmo di stima di parametri computazionalmente efficiente, usato per caratterizzare proprietà fisiche rilevanti di tali materiali. Successivamente verranno estesi a geometrie 2D e 3D per tener conto in maniera più naturale di alcuni fenomeni intrinsecamente multidimensionali come la non planarità delle interfacce semiconduttore-isolante causata da difetti dovuti al processo produttivo, contributi parassitici di capacità dovuti all'accoppiamento tra strati metallici,

Sommario

la curvatura delle bande energetiche in corrispondenza di interfacce semiconduttore-sottostrato e la resistenza di contatto dovuta a effetti di current-crowding.

Metodi numerici robusti sono necessari per simulare i modelli sopra descritti. Verrà proposta una formulazione numerica monodimensionale basata su una modifica dello schema di discretizzazione di Scharfetter-Gummel che è termodinamicamente consistente anche in quei sistemi fisici in cui la relazione di Einstein tra i coefficienti di mobilità e diffusività non sia soddisfatta. Quindi la formulazione è estesa a mesh di quadtree (2D) e octree (3D), ossia griglie cartesiane gerarchiche non conformi, sviluppando uno schema di discretizzazione strettamente monotono che garantisca soluzioni non negative e prive di oscillazioni numeriche per problemi con strati limite di bordo o interni. Per aumentare l'accuratezza dello schema numerico vengono presentate formule alle differenze che permettono di ricostruire approssimazioni di ordine più elevato per il gradiente della soluzione e della soluzione numerica stessa: il gradiente e la soluzione ricostruiti sono impiegati per definire opportuni stimatori *a posteriori* dell'errore a partire dai quali calcolare una metrica che guidi l'adattazione della griglia di calcolo. Verranno discussi i vantaggi, in termini di efficienza, dell'approccio proposto rispetto a una tecnica standard di solve-mark-refine. Infine, le proprietà di alcuni metodi di linearizzazione robusti, in particolare di quelli che permettono di preservare la positività di densità fisiche durante lo schema di risoluzione, verranno analizzate.

Dal punto di vista dell'implementazione, recenti progressi nelle strutture dati e negli algoritmi per creare, raffinare gerarchicamente, bilanciare e partizionare mesh di quad- e oct-tree ha portato questa classe di griglie al vertice degli interessi di ricerca della comunità HPC come strumento per raggiungere estrema scalabilità. Tale obiettivo giustifica l'implementazione di un codice efficiente, parallelo e scalabile. Le strategie implementative seguite in fase di sviluppo saranno esaminate e motivate.

La formulazione di modelli fisici corrispondenti allo stato dell'arte e la loro interpretazione è stata condotta con il supporto del Prof. Dario Natali del Dipartimento di Elettronica, Informazione e Bioingegneria (DEIB), mentre la derivazione dello schema di discretizzazione su griglie di quadtree e la definizione degli algoritmi di adattazione di griglia sono state sviluppate in collaborazione con la Prof.ssa Simona Perotto del Dipartimento di Matematica del Politecnico di Milano. Un sentito ringraziamento è rivolto ai ricercatori del Centro per le Nanoscienze e Tecnologia dell'Istituto Italiano di Tecnologia (IIT) per aver raccolto e fornito le misure sperimentali utilizzate nella validazione dei modelli matematici presentati.

Parole chiave: transistor organici a film sottile; semiconduttori organici; trasporto di carica; barriera Schottky; iniezione di carica; relazione di Einstein; drift-diffusion; Scharfetter-Gummel; hpc; scalabilità; quadtree; adattazione di mesh

Acknowledgments

A Ph.D. is not just a Ph.D.

It is a stairway to walk up step-by-step, crawling, keeping the head down looking at the next move rather than at the unseen ceiling. Day after day, every new step you linger on is a discovery: seldom it is a quiet contribution to a body of knowledge; most of the times it is about yourself. You find out that being curious is the key not to get stuck, you realize that overcoming your limits is harder, yet more gratifying than stopping and giving up.

It's a luck not to feel alone along this path.

First of all I would like to express my deepest gratitude to Prof. Carlo de Falco, who taught me patiently how to overstep every single difficulty I inevitably faced through this research work.

I am profoundly thankful to Prof. Dario Natali for sharing his endless knowledge about the characterization and modeling of semiconductor devices, and indebted with Prof. Simona Perotto for her precious scientific contributions about mesh adaptation and invaluable human support.

I am also grateful for all the ideas or feelings shared with every colleague I met and with every student, if any, I was able to motivate, to inspire or to support.

This thesis would not have been possible without the all the inestimable laughs, *pausa*, thoughts and tears shared with every single friend who has been part of the *Sesto piano* during the past three years: after all, a burden shared is a burden halved. Simply, thank you all.

Un dottorato è più che solo un dottorato.

È una scalinata da salire gradino dopo gradino, avanzando lentamente e con la testa

Part I.

Introduction

1. Synopsis

This thesis is devoted to presenting mathematical models and numerical methods for the simulation of a class of organic electronic devices, specifically OTFTs.

Part I of this document is intended to describe the engineering applications that warrant for a mathematical investigation of organic semiconductors. The factors that motivate research in this field are presented in chapter 2, together with the possibilities of application of this kind of technology in lighting, photovoltaics, the production of flexible displays and other electronic components such as memories, batteries, ... OTFTs in particular will be the specific subject of chapter 3, giving a portrait of what makes them a key component for electronic circuits.

Part II contains the derivation of the physical models and the constitutive relations that describe charge transport in the devices under consideration, and the corresponding mathematical formulation. In particular, chapter 4 describes the physical phenomena behind charge transport in organic semiconductors, pointing out the differences with respect to classical silicon-based technologies. Relying on the DD equations, chapter 5 will present accurate models of the physics of energy barrier lowering and charge injection at metal-semiconductor interfaces and state-of-the-art constitutive relations that are representative of the molecular disorder of organic semiconductor materials, as discussed in [Afr+17]. Another original contribution of this research project is contained in chapter 6, that presents a hierarchy of mathematical formulations that have been shown to provide a consistent representation of the considered physical systems under thermal equilibrium, transient and time harmonic regimes of operation. The DD system has been coupled with an additional algebraic equation, derived in section 6.1.1, that is needed in order to provide consistence with the thermodynamic limit at the discrete level for arbitrary constitutive relations for the Density of States (DOS). Such mathematical formulation is the topic of [AFN19].

The disordered morphology and energetic structure of organic semiconductor devices warrants for the development of suitable numerical methods, subject of part III. Furthermore, the typically extreme form-factors of such devices and the high level of accuracy required for a meaningful comparison of simulation results to experimental data constitute a challenge which demands for an efficient implementation based on advanced HPC techniques. An adaptive time-advancing scheme is derived in chapter 7, while the prop-

erties of a set of robust linearization methods are investigated in chapter 8. Chapter 9 describes, in a one-dimensional framework, the derivation and the numerical properties of the Scharfetter-Gummel discretization method, an automatic upwind scheme satisfying a discrete maximum principle that makes it positivity-preserving, as required by the constraint of a non-negative electron density. Following the formulation anticipated in section 6.1.1, a modification of the Scharfetter-Gummel scheme for arbitrary DOS shapes that don't necessarily match with the classical Einstein relation, is also proved to be thermodynamically consistent. Furthermore, 2D and 3D simulations are required in order to account in a more natural way for a set of inherently multi-dimensional phenomena, such as the non-planarity of semiconductor-insulator interfaces due to the solution processing of the materials, parasitic capacitances due to coupling between metal layers, the bending of energy bands at the semiconductor-substrate interface away from contacts and the contact resistance due to current-crowding effects. This motivates the extension, proposed in chapter 10, of the above-described discretization scheme to meshes of quad-trees (2D) and oct-trees (3D), that are hierarchical, non-conforming Cartesian grids, by developing a strictly monotone discretization scheme that guarantees non-negative and oscillation-free solutions for problems with steep boundary and interior layers. To increase the accuracy of the numerical scheme we also derive a new recovery metric-based mesh adaptation procedure for quadtree meshes. The theoretical and numerical results obtained are the main subject of [AFP19]. The goal of achieving extreme scalability drives the development of an efficient, parallel, scalable code. The implementation strategies followed will be examined and motivated.

Results of numerical simulations of both theoretical and application-motivated test cases are discussed in part IV. In chapter 11 the mesh adaptation algorithm is tested on linear stationary Advection-Diffusion-Reaction (ADR) problems and on a time-dependent system with a propagating front. A scalability result is also shown. Results of the application of the thermodynamic consistent discrete formulation to the solution of a propagating charge packet problem in semiconductors characterized by different DOS shapes are presented in chapter 12. In chapter 13 the models and the methods described are applied in a one-dimensional framework to derive a computationally efficient parameter estimation procedure used to characterize relevant physical properties of organic materials. The procedure relies on comparing simulation results to experimental data and has been tested on two benchmark organic semiconductors, providing a very satisfactory fit that proves the effectiveness of the procedure and the physical meaningfulness of the values extracted. Results of stationary and transient 2D simulations of OTFTs are presented in chapters 14 and 15, respectively. Finally, chapter 16 concludes the discussion and presents some possible extensions of the work presented in this document.

2. Organic electronics

Organic semiconductors are outstanding candidates for becoming the material platform for the development of large area, low cost, flexible electronics . Since they can be processed from solution, they can be formulated as functional inks and deposited by means of printing techniques adapted from graphical arts (ink-jet, screen printing, spray coating, flexography to cite but a few) .

Several factors have motivated a continuous research in organic semiconductor technologies, such as easy and low cost fabrication of large area circuits, mechanical flexibility, high transparency and bio-compatibility [CN15]. The molecular nature of organic materials allows sub-micron structures to be created at a low cost using soft-lithography, self-assembly or printing techniques instead of expensive conventional optical lithography used for inorganic (often silicon-based) devices [Kat14; Ben+14]. Moreover, organic sensors and transistors can be produced without the need of heavy metals or other harmful materials, thus guaranteeing bio-compatibility and the possibility to implant them in biological tissues. Ultimately, since they don't need to be processed at high temperatures, sensible substrates such as plastic or textiles can be exploited for the fabrication.

However, when drawing comparisons between plastic and silicon circuitry one must be aware that the two systems are deeply different and their behavior and performances do not necessarily match. A major drawback of organic devices is a lower charge carrier mobility, *i.e.* the ability of charged particles to move in response to an electric field, due to weak intermolecular interactions in the solid state. Their electronic performance has been constantly improving over the past years, as shown in fig. 2.1, leading to devices which compare well to, or even outperform, those based on amorphous silicon. Therefore, organic materials should not be expected to replace silicon as the favored basis for electronic circuits, but to enable research for new and emerging applications.

An important trend is that key industry sectors are implementing a variety of products based on organic and printed electronics. In particular, a strong engagement and product introduction is seen in the automotive, consumer electronics, packaging and medical/pharmaceutical sectors.

New possibilities of this kind of technology can be grouped into five clusters [OEA]:

1. lighting (Organic Light-Emitting Diodes (OLEDs));
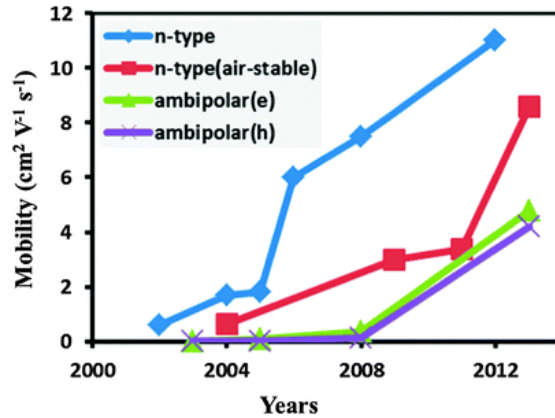
Figure 2.1.: Recent mobility trend for a class of organic semiconductors. Source: [Zho+14].

2. light-harvesting (photovoltaics);

3. flexible displays;

4. electronics and components (memories, batteries, . . .);

5. integrated smart systems (smart objects, sensors and smart textiles).

2.1. Lighting

OLED-based lighting is seen as the most promising approach for future lighting due to superior efficiency, flexibility, and high durability. Moreover, devices like white emitting OLEDs for general lighting, monochrome OLED lamps for automotive or signage applications, are growing in importance. The market is expected to grow steadily, especially if some key challenges, such as continued lowering of production costs, are met.

2.2. Photovoltaics

Organic Photovoltaics (OPV) is an recent energy technology. OPV devices typically consist of a semi-transparent substrate and a photo-absorbing organic layer. They can be made on flexible substrates, thus enabling power sources to be suitable for many

emerging applications, such as wearable and mobile devices. The production of this kind of devices guarantees a much shorter payback time than inorganic technology, although efficiency and lifetime are still under improvement.

2.3. Flexible displays

Flexible displays are an extension of flat panel displays that successfully replaced cathode-ray tubes for use in computers and televisions and made the existence of laptops, tablets, e-readers, smartphones possible. Flexible organic-based displays can dispense with some key issues of current flat ones, such as the presence of breakable and heavy glass and the inability to be bent or used with different form factors. The market is starting to demonstrate a variety of flexible displays, from mobile phone to watches, and it is growing to lead into wider availability of flexible consumer electronics.

2.4. Electronics and components

Electronics and components include, for example, printed memories and flexible batteries.
Printed memories are needed for information storage. Micro-circuits printed on labels can hold product information such as lot codes, serial numbers, expiration dates and geographic codes, which can keep counterfeiters at bay.
Flexible batteries are of central importance in solving the issue of power supply in gaming as well as in mobile and wellness devices, besides being employed in *smart packaging* applications.
Active (such as transistors, diodes, logic circuits and display elements) and **passive** (resistors, capacitors, inductors, tubes) **components** can also be printed.
An area that was recently interested by intense research activity is that of **transparent conductive films**, to be used in optical devices, photovoltaics, electromagnetic shielding and for touch sensors in mobile devices.

2.5. Integrated smart systems

Smart objects bring multiple functionalities to perform complex tasks without the need for external hardware; integrated smart systems are being used in the development of sensors and smart textiles.

Sensors allow to detect information from the surroundings. Organic-based force sensors, for example, have found use as part of touch screen displays in consumer devices, but also in health care and automotive applications. More specifically, photodetectors are gaining importance in the market of logistics, environmental monitoring, and medical imaging.

Smart textiles are able to alter their properties in response to external stimuli; these functionalities are being embedded, for example, into clothing. Organic and printed electronics opens new possibilities in health monitoring with enhanced comfort for the wearer; the ability to process and transmit data makes *wearable electronics* a reality.

3. Organic Thin-Film Transistors (OTFTs)

Organic electronics is moving ahead on its journey towards reality: the continuous progress made in the field of organic semiconductors has achieved important goals such as relatively high charge carrier mobility, thus offering ample opportunities for organic-based printed integrated circuits [MN15].

FETs are nowadays the basis for all electronic circuits and processors. The ability to create transistors from organic materials raises exciting possibilities for low cost electronics. In particular OTFTs, which are FETs made by depositing thin films of an organic semiconductor layer over a non-conducting substrate (such as glass), are being adopted in the development of products such as backplanes of flexible displays and circuits for sensor applications.

Research on organic FETs over the past 25 years has contributed greatly to the scientific understanding of the fundamental charge transport physics of conjugated polymer and small-molecule organic semiconductors [Sir14]. These materials provide unique realizations of systems where transport is intermediate between conventional low-mobility transport in amorphous glasses and high-mobility transport in crystalline materials.

3.1. Mechanism of operation

A FET is a three-terminal component where the current flow between the *source* and the *drain* contacts is controlled by the voltage applied to the *gate* terminal (see fig. 3.1) [Ben+14]. It can be used as a single component to amplify a current or combined with other transistors into an integrated circuit.

The metallic gate, the insulator layer and the bulk semiconductor act in effect as a capacitor, with the gate forming one plate, the insulator acting as a dielectric spacer, and the semiconductor forming the other plate: this is called a Metal-Insulator-Semiconductor (MIS) capacitor. Therefore, when applying a bias across the plates, opposite and equal charges accumulate at the insulator-semiconductor interface. This capacitive effect determines the charge density in the channel (the region between the source and drain electrodes where charge carriers actually flow); when applying a higher bias than a threshold gate voltage V_T the conductivity becomes substantial and the device turns
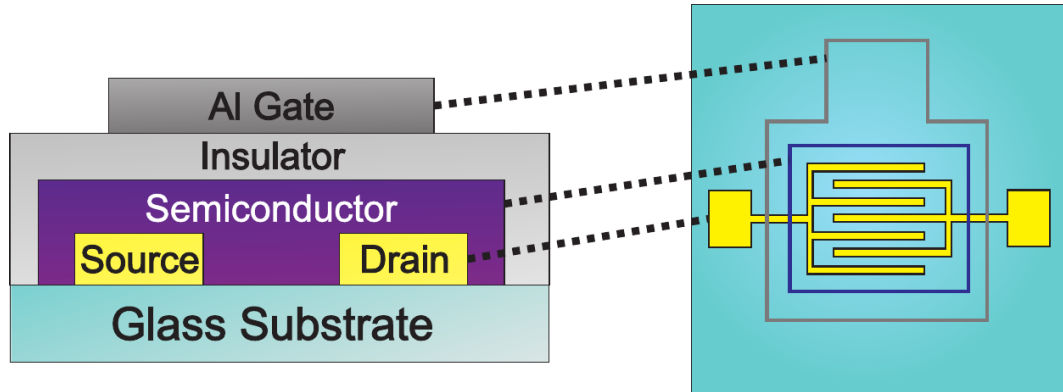
Figure 3.1.: Schematic of a thin film transistor (side view and top view). Source: [Mad+15].

on. Then the motion of charge carriers from source to drain through the semiconductor layer takes place on applying a suitable drain-to-source potential V_{DS} [KKN14].

3.2. Applications and perspectives

OTFTs are extremely useful in applications such as flexible integrated circuits, sensors, organic memories, e-paper and Radio-Frequency Identification (RFID) tags; moreover, they have turned out to be promising backplane drivers in OLED-based flexible displays (see figs. 3.2 and 3.3) [KKN14]. Recent advancements in organic material fabrication techniques direct the researchers to make use of flexible substrates, such as paper, plastic, glass and fiber, for low cost and light weight flexible applications.

OTFTs find also extensive applications in organic inverters and ring oscillators. Few recent examples of use are described in the following subsections [KKN14].

RFID tags

A potentially emerging area for OTFTs is Radio-Frequency Identification of an object. Organic RFIDs are useful in different kind of applications, such as electronic product coding/labeling, supply chain management, medical science, toll bridges and identification of inventory in retail shops. Developments in low temperature fabrication techniques for organic materials encourage to make use of them in RFID tags instead of their silicon-based counterparts which are almost three orders more expensive.

Figure 3.2.: Photographs of A) flexible electrophoretic displays; B) plastic-printed microprocessors. Source: [Sir14].
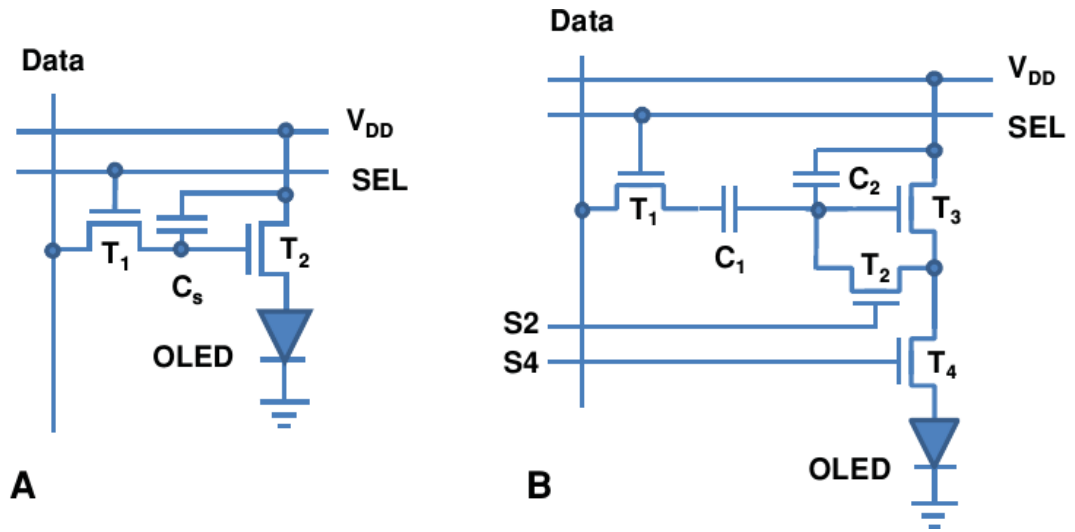
Figure 3.3.: Pixel circuits for active matrix OLEDs. The letter T denotes OTFTs. Source: [Sir14].

Organic DNA sensors

OTFTs are promising for application in flexible Deoxyribonucleic Acid (DNA) sensors due to their quick response time. This can enable the deployment of DNA micro-array techniques for disposable diagnosis toolkits. These sensors are often used to detect and quantify the nucleic acids for forensic analysis and pharmacogenomic research, by transforming a chemical binding event into electrical signals that can be easily measured and analyzed.

References

[AFN19]   P. C. Africa, C. de Falco, and D. Natali. "A Note on Thermodynamically Consistent Flux Discretization". In: *In preparation* (2019) (cit. on pp. 23, 59, 93).

[AFP19]   P. C. Africa, C. de Falco, and S. Perotto. "Scalable Recovery-based Adaptation on Quadtree Meshes". In: *In preparation* (2019) (cit. on pp. 24, 97, 133).

[Afr+17]   P. C. Africa, C. de Falco, F. Maddalena, M. Caironi, and D. Natali. "Simultaneous Extraction of Density of States Width, Carrier Mobility and Injection Barriers in Organic Semiconductors". In: *Scientific Reports* 7.1 (2017), p. 3803 (cit. on pp. 23, 54, 55, 161).

[Ben+14]   A. J. Ben-Sasson, M. Greenman, Y. Roichman, and N. Tessler. "The Mechanism of Operation of Lateral and Vertical Organic Field Effect Transistors". In: *Israel Journal of Chemistry* 54.5-6 (2014), pp. 568–585 (cit. on pp. 25, 29).

[CN15]   M. Caironi and Y.-Y. Noh. *Large Area and Flexible Electronics*. Wiley–VCH, 2015 (cit. on p. 25).

[Kat14]   S. Katsuaki. *Introduction to Printed Electronics*. Springer New York, 2014 (cit. on p. 25).

[KKN14]   B. Kumar, B. K. Kaushik, and Y. S. Negi. "Perspectives and Challenges for Organic Thin Film Transistors: Materials, Devices, Processes and Applications". In: *Journal of Materials Science: Materials in Electronics* 25.1 (2014), pp. 1–30 (cit. on p. 30).

[Mad+15]   F. Maddalena, C. de Falco, M. Caironi, and D. Natali. "Assessing the Width of Gaussian Density of States in Organic Semiconductors". In: *Organic Electronics* 17 (2015), pp. 304–318 (cit. on pp. 30, 47, 51, 161–164, 168, 170, 173, 175, 177).

[MN15]   S. Mandal and Y.-Y. Noh. "Printed Organic Thin-Film Transistor-based Integrated Circuits". In: *Semiconductor Science and Technology* 30.6 (2015), p. 064003 (cit. on p. 29).

References

[OEA]   *OE - A Roadmap for Organic and Printed Electronics, 6th Edition*. White Paper. Organic and Printed Electronics Association, 2015. URL: `http://www.oe-a.org` (cit. on p. 25).

[Sir14]   H. Sirringhaus. "25th Anniversary Article: Organic Field-Effect Transistors: The Path beyond Amorphous Silicon". In: *Advanced Materials* 26.9 (2014), pp. 1319–1335 (cit. on pp. 29, 31, 32).

[Zho+14]   K. Zhou, H. Dong, H.-l. Zhang, and W. Hu. "High Performance N-type and Ambipolar Small Organic Semiconductors for Organic Thin Film Transistors". In: *Physical Chemistry Chemical Physics* 16.41 (2014), pp. 22448–22457 (cit. on p. 26).

Part II.

Physics of organic semiconductors and mathematical models

4. Charge transport

As anticipated in the introduction, while physical mechanisms governing charge transport in organic semiconductors are inherently different from those in well known crystalline inorganic materials such as, e.g., silicon, the mathematical models used to simulate such phenomena are strongly correlated. For this reason, it is common practice to introduce the physical bases of charge transport in inorganic semiconductors (section 4.1) in order to mark the differences with respect to organic ones (section 4.2).

4.1. Inorganic semiconductors

Atoms in ordered inorganic semiconductors (such as silicon) are kept together by covalent bonds which originate a perfectly regular, crystalline solid. Typically inorganic semiconductors are built from elements in group IV of the periodic table (Si, Ge, . . .), possibly compounded with elements belonging to group III or V (GeAs, InAs, InP, . . .). In such systems electronic states are clearly defined and give rise to an *energy-band structure*: charge carriers are confined to a number of bands of admissible energy levels (*valence band* and *conduction band*), separate by an *energy gap* consisting of forbidden energy levels (see fig. 4.1).

Charge carriers in the *transport* bands are said to be *delocalized* as their wave functions are spread across more than one atom and hence particles occupying such states can be located anywhere in the whole crystal. Occasionally their motion is hampered by *scattering* phenomena due to imperfections in the crystalline structure such as dopants or phonons, generated by vibrational motions of the lattice. In a wave-only view, carriers are plane waves propagating in a periodic potential generated by atomic nuclei and charges occupying inner energetic levels in the periodic lattice.

As a consequence of the band transport described above, a crystalline semiconductor can be approximated as a charged rarefied gas, where particles are free to move; hence typical transport models can be deduced from the Boltzmann Transport Equation (BTE):

$$\frac{\partial f}{\partial t} + \frac{d\mathbf{x}}{dt} \cdot \nabla_{\mathbf{x}} f + \frac{d\mathbf{p}}{dt} \cdot \nabla_{\mathbf{p}} f = 0,$$
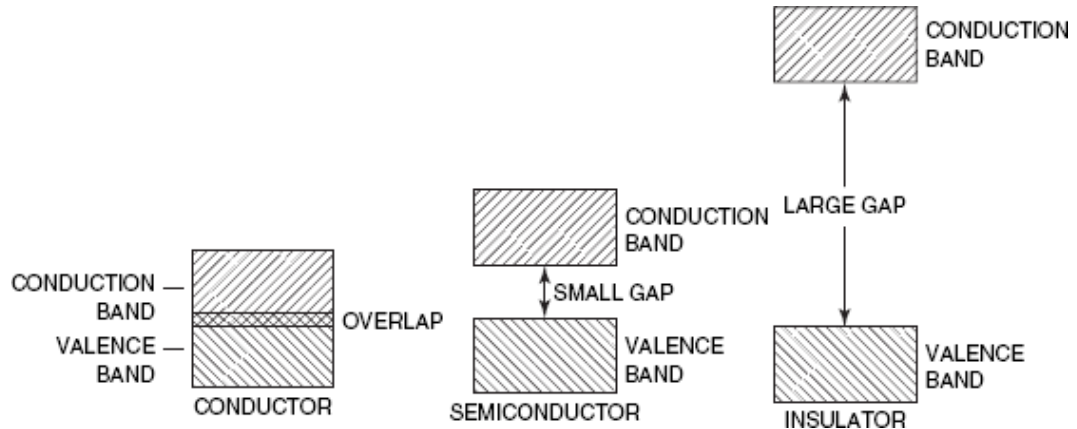
Figure 4.1.: Valence and conduction bands in different materials. Source: [Hec11].

where $f = f(\mathbf{x}, \mathbf{p}, t)$ denotes the distribution function of a generic charge carrier in the seven-dimensional space of spatial coordinates ($\mathbf{x}$), momentum ($\mathbf{p}$) and time (t). The classical DD model is the zero-order moment in the hierarchical expansion of Boltzmann's equation [Jer96; MRS90; AR99; AR00].

The amount of available free charge carriers in inorganic semiconductors may be artificially tuned by introducing dopant impurities (see section 4.3), which are easily ionized by thermal excitation even at room temperature.

4.2. Organic semiconductors: energetic disorder

Unlike inorganic semiconductors, an organic semiconducting material is a molecular solid whose molecules are kept together by *van der Waals' interactions* acting between permanent and induced dipoles and are relatively weak compared to covalent bonds. As a result, organic semiconductors have an up to 80% lower relative dielectric permittivity, therefore Coulomb interactions between charges are stronger. Weak intermolecular interactions and common production techniques of organic semiconductor materials often lead to high levels of topological and energetic disorder [CB12]; these systems can be distinguished into the *amorphous* and *semi-crystalline* categories [Kax03]:

- in **amorphous solids** there is no long-range order of any type, even though the local arrangement of atoms has a certain degree of regularity;

- **quasi-crystals** show certain symmetries such as rotations, reflections or an un-

Figure 4.2.: Localization and delocalization of energetic states. Source: photonicswiki.

derlying regular pattern, but they are not compatible with a three-dimensional periodicity; these crystalline regions attain nano- to micro-metric dimensions.

Each molecule is characterized by the Highest Occupied Molecular Orbital (HOMO) and Lowest Unoccupied Molecular Orbital (LUMO) (called the *frontier orbitals*): current conduction occurs when excited charges jump from a frontier orbital (which is the LUMO for electrons and HOMO for holes) to the same frontier orbital of an adjacent molecule.

In contrast to ordered crystalline semiconductors (with well-defined energy structures consisting of bands and gaps), the energy spectrum of a disordered material can be treated as quasi-continuum [Wei+06]. Instead of bands and gaps one can distinguish between extended and localized states[1] (see fig. 4.2), where, according to the definition given in [And78] by P. W. Anderson (Nobel Prize in Physics, 1977), a charge carrier wave function is respectively spread over the whole volume or localized to a restricted region. Localized sites can be interpreted as segments of a conjugated polymer chain and are responsible for the flow of charge, as charge carriers spend most of their time localized in a precise energetic state on a molecule.

Charge transport occurs by means of a *hopping mechanism* (see fig. 4.3), which is a phonon-assisted and thermally activated quantum tunneling effect (where a particle tunnels through an energetic barrier that would not be possible to overcome *classically*) from one site to another neighboring site. This is why in organic materials hopping events are promoted by high temperatures (which allow for higher molecular vibration amplitude), while in inorganic semiconductors the mobility decreases with temperature.

---

[1]In a mathematical formalism, a *quantum state* is a vector in an Hilbert space over a complex field. It is often referred to as a *wave function* [Gri05b], which encodes all the information about positions and momenta of a system of particles.

Usually, the conductivity σ is found to be thermally activated as:

$$\sigma(T) = \sigma_0 \exp\left(-\frac{E_{act}}{k_B T}\right),$$

where σ_0 is the (theoretical) maximum conductivity $[\text{O}\,m^{-1}]$, k_B the Boltzmann constant $[J \cdot K^{-1}]$, T the temperature [K] and E_{act} the activation energy [J].

Many hopping models are based on the solution of a *Master equation* [Wei+06], which consists of a discrete balance of hopping probabilities from each site to neighboring ones and will be described in more details in section 5.1.

4.3. Doping

Doping, *i.e.* introducing charged impurities into a pure (intrinsic) lattice, led to the breakthrough of conventional semiconductor technologies; it granted the possibility to control the flow of charge carriers, giving rise to the design of $p-n$ junctions, the *building blocks* of most electronic devices. Furthermore, doping may be used to enhance device performances by adjusting the conductivity and the position of the Fermi level.

Organic semiconductors can be doped by adding electron acceptors or donors, but doping techniques are still under study. Because of the weak van der Waals' interactions between molecules, organic materials are less sensitive to impurities and structural defects than crystalline semiconductors but, because of stronger Coulomb interactions between charges, dopant concentrations have to be considerably higher for organic materials, thus affecting the molecular assembly, the morphology, and the electronic properties of the film (mobility, energy levels distribution, . . .).

Doping can be described as a two-step process:

1. the dopant is ionized, transferring an electron (hole) to the host material and leaving a hole (electron) on the dopant; the ionization energy corresponds to the difference between the HOMO level and the vacuum energy level;

2. the electron (hole) has to dissociate against the Coulomb attraction of the hole (electron) left on the dopant.

The second step is harder to achieve in the case of organic semiconductors because of their lower relative permittivity.

Two major drawbacks of doping organic semiconductors are the instability of the dopant concentration, which is usually not constant in time, and the difficulty to control the doping level inside the device, because of a lower doping efficiency (defined as
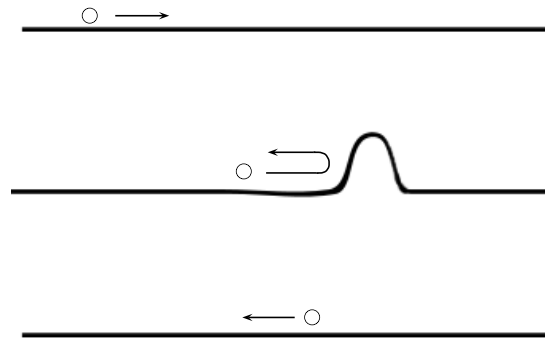
(a) Band transport. In a crystal (the straight line) charge carriers are delocalized. Lattice vibrations disrupt the symmetry, thus limiting the carriers mobility.
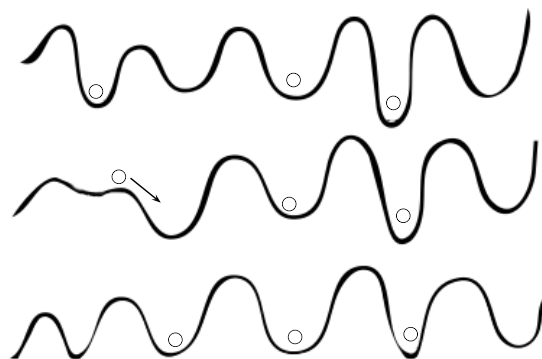
(b) Hopping transport. Carriers are localized due to defects or disorder, so the lattice vibrations are essential for a carrier to move from one site to another.

Figure 4.3.: Charge transport in inorganic and organic semiconductors. Source: [PS99].

the ratio of the density of free charge carriers to the density of dopants) due to the molecular disorder. This is why these materials are often used as intrinsic and charges are preferred to be injected through metal electric contacts.

5. Physical models

5.1. Discrete modeling: the master equation

By considering the semiconductor as a system of localized quantum states (that may or may not be occupied by charged particles), the general transport equation describing the balance of hopping events between a state i and a state j is the *Master equation* [Mei+06]:

$$\frac{dp_i}{dt} + W_{ij}p_i(1 - p_j) - W_{ji}p_j(1 - p_i) = 0, \qquad \forall i, j, \tag{5.1}$$

and its stationary limit

$$W_{ij}p_i(1 - p_j) - W_{ji}p_j(1 - p_i) = 0, \qquad \forall i, j,$$

where
  p_i is the time-averaged probability of occupation of the state i by a charge;
  W_{ij} is the transition rate for hopping from site i to site j.

  The penalty terms $(1 - p_i)$ and $(1 - p_j)$ account for Pauli's exclusion principle by prescribing that only one charge carrier can occupy a site. By assuming that hopping of carriers from site to site occur by means of a thermally assisted tunneling process, the coefficients W_{ij} can be expressed by the *Miller-Abrahams model* [MA60]:

$$W_{ij} = \begin{cases} \nu_0 \exp\left(-2\varpi R_{ij} - \frac{\mathcal{E}_j - \mathcal{E}_i}{k_B T}\right), & \mathcal{E}_j \geq \mathcal{E}_i, \\ \nu_0 \exp\left(-2\varpi R_{ij}\right), & \mathcal{E}_j < \mathcal{E}_i, \end{cases} \tag{5.2}$$

where
  k_B is the Boltzmann constant $\left[J \cdot K^{-1}\right]$;
   T is the temperature [K];
  ν_0 is the *attempt-to-escape* frequency rate;
  R_{ij} $= \left|\mathbf{R}_j - \mathbf{R}_i\right|$ is the distance between site i and site j [m];
   ϖ is the inverse localization length of the states considered $\left[m^{-1}\right]$;
  $\mathcal{E}_i$ is the energy of site i [J].

Equation (5.1) can be solved by drawing the on-site energies $\mathcal{E}_i$ randomly from a given distribution representing the Density of States (further details about the choice of this function will be given in section 5.4). The equilibrium distribution of charges according to eq. (5.1) is usually computed by means of a Monte Carlo method by simulating the evolution of an initial population until equilibrium is reached [SBS81; Bäs93; Bou+09]. Once the solution has been computed, the mobility coefficient $\mu \left[\mathrm{m^2 V^{-1} s^{-1}}\right]$ related to a generic charge carrier is given by (see [Bou+09])

$$\mu = \frac{\frac{1}{N} \sum_{i,j} W_{ij} p_i (1 - p_j) R_{ij,\mathbf{E}}}{|\mathbf{E}|}, \tag{5.3}$$

where

$$N \quad = nV \text{ is the total number of charge carriers, } V \text{ being the total volume and } n$$
the average of the occupation probabilities p_i over V;

$$\mathbf{E} \quad \text{is an applied electric field } \left[\mathrm{V \cdot m^{-1}}\right];$$

$$R_{ij,\mathbf{E}} \quad \text{is the distance between site } i \text{ and site } j \text{ along the direction of } \mathbf{E} \text{ [m]}.$$

The numerator of eq. (5.3) can be interpreted as the velocity of the particles. Taking the limit of the master equation as the dimension of the space of energetic states becomes continuum leads to the DD model.

5.2. Continuum modeling: the Drift-Diffusion system

A continuum model can be derived by assuming the distribution of charges in the material to be a function of a continuum spatial variable. The electromagnetic fields inside the device can be modeled through Maxwell's equations:

$$\begin{cases} \nabla \cdot \mathbf{D} = \rho, & (5.4a) \\ \nabla \times \mathbf{E} + \dfrac{\partial \mathbf{B}}{\partial t} = \mathbf{0}, & (5.4b) \\ \nabla \cdot \mathbf{B} = 0, & (5.4c) \\ \nabla \times \mathbf{H} - \dfrac{\partial \mathbf{D}}{\partial t} = \mathbf{J}, & (5.4d) \end{cases}$$

where

E   the electric field $\left[\mathrm{V} \cdot \mathrm{m}^{-1}\right]$;
D   the electric displacement field $\left[\mathrm{C} \cdot \mathrm{m}^{-2}\right]$;
ρ   the volume charge density $\left[\mathrm{C} \cdot \mathrm{m}^{-3}\right]$;
B   the magnetic induction field $\left[\mathrm{N} \cdot \mathrm{A}^{-1}\mathrm{m}^{-1}\right]$;
H   the auxiliary magnetic field $\left[\mathrm{A} \cdot \mathrm{m}^{-1}\right]$;
J   the electric current density (per unit area) $\left[\mathrm{A} \cdot \mathrm{m}^{-2}\right]$.

In the *effective homogeneous medium* approach we assume that the material is a linear, isotropic, homogeneous medium, provided that suitable effective values are used for the material coefficients. In such case, the constitutive relation $\mathbf{D} = \varepsilon \mathbf{E}$, $\varepsilon = \varepsilon_0 \varepsilon_r$ holds, ε_0 being the vacuum permittivity $\left[\mathrm{C} \cdot \mathrm{V}^{-1}\mathrm{m}^{-1}\right]$ and ε_r the material relative permittivity.

5.2.1. Poisson's equation

From (5.4c) it is possible to introduce a *vector potential*, *i.e.* a vector field **A** such that

$$\nabla \times \mathbf{A} = \mathbf{B}.$$

The *gauge freedom* allows to write a vector potential in the form $\mathbf{A} + \nabla \phi$ [Jac99] where ϕ is an arbitrary function, as $\nabla \times \nabla \phi = 0 \; \forall \phi$.
We assume basic regularity hypotheses for the functions considered and the domain (so that derivatives can be interchanged); hence, by inserting last equation into (5.4b) we get

$$\nabla \times \left(\mathbf{E} + \frac{\partial \mathbf{A}}{\partial t} \right) = \mathbf{0} \Rightarrow \mathbf{E} + \frac{\partial \mathbf{A}}{\partial t} = -\nabla \varphi$$

for a proper function φ called the *electrostatic potential*.
After a multiplication by ε the equation becomes

$$\mathbf{D} + \varepsilon \frac{\partial \mathbf{A}}{\partial t} = -\varepsilon \nabla \varphi.$$

Applying now the operator divergence and interchanging time and space derivatives:

$$\nabla \cdot \mathbf{D} + \varepsilon \frac{\partial}{\partial t}(\nabla \cdot \mathbf{A}) = -\nabla \cdot (\varepsilon \nabla \varphi),$$

which, through (5.4a), gives:

$$\varepsilon \frac{\partial}{\partial t}(\nabla \cdot \mathbf{A}) + \nabla \cdot (\varepsilon \nabla \varphi) = -\rho.$$

45

We choose the arbitrary function ϕ so that the *Lorenz gauge condition* is satisfied, namely

$$\varepsilon \frac{\partial}{\partial t}(\nabla \cdot \mathbf{A}) = -\frac{1}{c^2}\frac{\partial \varphi}{\partial t},$$

c being the vacuum velocity of electromagnetic waves. The electrostatic potential φ is then the solution to the *wave equation*

$$\frac{1}{c^2}\frac{\partial^2 \varphi}{\partial t^2} - \nabla \cdot (\varepsilon \nabla \varphi) = \rho.$$

c is usually much greater than the characteristic propagation velocities in the device considered (for example the mean velocity of a charge carrier); in other words, we are assuming that the length of the highest frequency electromagnetic wave is much greater than a characteristic length of the device, *i.e.* there is no substantial propagation. Therefore, the first term is negligible compared to the others and a *Poisson equation* for the electrostatic potential φ is obtained [Mar86]:

$$-\nabla \cdot (\varepsilon \nabla \varphi) = \rho.$$

In the following we will assume that the device domain Ω is composed by a semiconductor region Ω_{semic} and an insulator region Ω_{ins} such that $\Omega_{semic} \cup \Omega_{ins} = \Omega$. Hence the following expressions hold:

$$\varepsilon = \begin{cases} \varepsilon_{semic}, & \text{in } \Omega_{semic}, \\ \varepsilon_{ins}, & \text{in } \Omega_{ins}, \end{cases}$$

and

$$\rho = \begin{cases} -q\,(n - p + N_D), & \text{in } \Omega_{semic}, \\ 0, & \text{in } \Omega_{ins}. \end{cases}$$

Here n and p $[m^{-3}]$ are the charge carrier (electron and hole respectively) volume densities and N_D $[m^{-3}]$ is the net dopant concentration ($N_D < 0$ denotes an n-type doping and $N_D > 0$ a p-type one).
Finally, the Poisson equation becomes

$$-\nabla \cdot (\varepsilon \nabla \varphi) = -q(n - p + N_D), \quad \text{in } \Omega. \tag{5.5}$$

5.2.2. Model assumptions

Hereinafter, we will assume the following hypotheses [Mad+15]:

- the semiconductor is intrinsic, *i.e.* the dopant concentration N_D is zero, as it is very often the case in organic semiconductors; hence the total charge density becomes

$$\rho = \begin{cases} -q\,(n-p)\,, & \text{in } \Omega_{\text{semic}}, \\ 0, & \text{in } \Omega_{\text{ins}}; \end{cases}$$

- thermal generation effects are negligible (energy gaps are sufficiently large);

- leakage currents are negligible in the insulator region Ω_{ins};

- the semiconductor is unipolar, *i.e.* the device operation is based predominantly on the use of majority charge carriers; we will consider n-type devices, *i.e.* $p \approx 0$ (p-type devices can be treated analogously), and will neglect generation/recombination phenomena. From these assumptions we get the simplified expression

$$\rho = -qn. \tag{5.6}$$

Since techniques for establishing stable doping in organic semiconductors are still under study, bipolar devices have been given less attention in the literature; moreover, the device architecture of FETs is simple and requires only one type of charge carrier [KB15].

5.2.3. Continuity equation

One more equation can be deduced by a basic conservation principle in order to describe the evolution of n.

The conservation of the total number of particles, when generation/recombination phenomena do not occur, is expressed by the following equation:

$$\frac{\partial n}{\partial t} + \nabla \cdot f_n = 0, \quad \text{in } \Omega_{\text{semic}}, \tag{5.7}$$

where f_n is the electron flux density $\left[\text{m}^{-2}\text{s}^{-1}\right]$. We define the total electron current density $\left[\text{A} \cdot \text{m}^{-2}\right]$ as

$$J_n = -qf_n.$$

5. *Physical models*

By linearizing the electron distribution functions around equilibrium, the following constitutive relation for the current density can be derived [Sel12]:

$$J_n = q\mu_n n \nabla \varphi_n, \tag{5.8}$$

where μ_n denotes the electron mobility respectively $\left[m^2 V^{-1} s^{-1}\right]$ and φ_n is the *electrochemical potential* [V], accounting for both electrical and chemical interactions between charges. At equilibrium the electrochemical potential is spatially constant, while in the non-equilibrium case it is a function of the position.

The total number of charge carriers at a given energy can be estimated by means of statistical mechanics models. Let $\mathcal{E}_{\text{LUMO}}$ and $\mathcal{E}_{\text{HOMO}}$ be the energy levels corresponding to the molecular orbitals LUMO and HOMO respectively, and let $g(\mathcal{E})$ the DOS function; the quantity $g(\mathcal{E}) \, d\mathcal{E}$ represents the density of available quantum states (per unit volume) that may have energy within an infinitesimal range $d\mathcal{E}$ of energies centered at $\mathcal{E}$. The total amount of charge carriers per unit volume is thus expressed as the sum over all the admissible energies of the DOS function weighted on the probability of occupation f_D of an energy state:

$$n = \int_{-\infty}^{+\infty} g\left(\mathcal{E} - \mathcal{E}_{\text{LUMO}}\right) \cdot f_D\left(\mathcal{E} - \mathcal{E}_F\right) \, d\mathcal{E}, \tag{5.9}$$

where the function $f_D(\mathcal{E})$ denotes the occupation probability of the state having energy $\mathcal{E}$ and $\mathcal{E}_F$ denotes the Fermi level, a quantity related to the electrochemical potential. For a population of fermions, *i.e.* a system of many particles obeying the Pauli exclusion principle[1], the occupation probability is given by the Fermi-Dirac statistics, which is the statistical distribution identified through the density function

$$f_D(\mathcal{E}) = \frac{1}{1 + \exp\left(\frac{\mathcal{E}}{k_B T}\right)}.$$

The Fermi-Dirac statistics represents, according to Pauli's exclusion principle ($f_D(\mathcal{E}) < 1 \; \forall \mathcal{E}$), the average number of electrons occupying the state having energy $\mathcal{E}$.

We define the Fermi level $\mathcal{E}_F$ [J] as the thermodynamic work required to add one electron to a fermion system [Kit08]. An understanding of how it relates to the electronic structure is essential to describe the physics of a solid-state system. The Fermi level does not necessarily correspond to an actual energy level (for example, in an insulator the

---

[1]Pauli's exclusion principle states that the same quantum state cannot be occupied simultaneously by two identical fermions.

Fermi level lies in the band gap and is not populated by charges). By definition, the Fermi level is such that

$$f_D\left(\mathcal{E}_F\right) = \frac{1}{2},$$

which means that an electron or a hole has a 50% probability to occupy the energy level $\mathcal{E}_F$. Equation (5.9) rigorously holds for a system at thermal equilibrium, where $\mathcal{E}_F$ is a constant. In a system out of equilibrium we can assume a generalized version of eq. (5.9) to hold, by allowing the Fermi level $\mathcal{E}_F$ to depend on spatial coordinates; it turns out that the resultant force acting on a particle is proportional to the gradient of such *quasi-Fermi* energy.

Without loss of generality, we can choose an energetic reference level such that both $\mathcal{E}_{LUMO}$ and $\mathcal{E}_F$ are related to the electrostatic and the quasi-Fermi potential by the following affine relations

$$\mathcal{E}_{LUMO} = -q\varphi,$$
$$\mathcal{E}_F = -q\varphi_n. \tag{5.10}$$

so that the constitutive relation (5.9) becomes

$$n = \int_{-\infty}^{+\infty} g\left(\mathcal{E} + q\varphi\right) \cdot f_D\left(\mathcal{E} + q\varphi_n\right) d\mathcal{E}. \tag{5.11}$$

At high energies, *i.e.* when $\mathcal{E} \gg k_B T + \mathcal{E}_F$, then the Fermi-Dirac distribution can be approximated as:

$$f_D\left(\mathcal{E}\right) \approx \exp\left(-\frac{\mathcal{E} - \mathcal{E}_F}{k_B T}\right), \tag{5.12}$$

which is called the Maxwell-Boltzmann statistics. Carrier densities usually involved in typical organic semiconductor devices are such that the Fermi level lies inside a region where the DOS function is not negligible; therefore the Maxwell-Boltzmann approximation can not be used except for a narrow range of energy values.

5.3. Generalized Einstein relation

We define a *chemical potential* ϕ as

$$\phi = \varphi - \varphi_n. \tag{5.13}$$

The definition above is compatible with [Mad95], while other authors [AM88] use swapped definitions for chemical and electrochemical potentials. From eq. (5.11), after

a change of variables, the electron density can be represented as a function of the chemical potential, *i.e.* $n = n(\phi)$. Therefore its spatial gradient is computed as

$$\nabla n = \frac{\partial n}{\partial \phi} \left(\nabla \varphi - \nabla \varphi_n \right).$$

By substituting this expression into eq. (5.8) we get

$$J_n = -q \mu_n n \nabla \varphi + q D_n \nabla n, \tag{5.14}$$

which corresponds to the familiar **drift-diffusion** constitutive relation for the electron current density; here we have introduced the electron diffusion coefficient $\left[m^2 s^{-1} \right]$

$$D_n = \mu_n \frac{n}{\frac{\partial n}{\partial \phi}}. \tag{5.15}$$

Equation (5.15) provides a generalization, valid for an arbitrary DOS shape, of the relation discovered by Einstein and Smoluchowski in their analysis on the Brownian motion [ES99].

It can be easily shown that the classical Einstein relation can be deduced as a particular case of eq. (5.15) through an appropriate choice for the function $g(\mathcal{E})$. For example, let us consider the typical DOS function for an inorganic semiconductor

$$g(\mathcal{E} - \mathcal{E}_c) \propto \sqrt{\mathcal{E} - \mathcal{E}_c} \cdot \mathbb{1}_{\{\mathcal{E} > \mathcal{E}_c\}},$$

where the proportionality is intended up to a multiplicative constant, $\mathbb{1}$ denotes the indicator function and $\mathcal{E}_c$ is the energy of the bottom of the conduction band (analogous to the $\mathcal{E}_{LUMO}$ in an organic semiconductor), and the zero-disorder limit for an organic semiconductor:

$$g(\mathcal{E} - \mathcal{E}_{LUMO}) \propto \delta(\mathcal{E} - \mathcal{E}_{LUMO}),$$

where $\delta(\mathcal{E} - \mathcal{E}_{LUMO})$ denotes the Dirac delta centered at $\mathcal{E}_{LUMO}$. Under the Maxwell-Boltzmann approximation (5.12) in both cases we get

$$n(\phi) \propto \exp\left(\frac{\phi}{V_{th}} \right) \quad \Longrightarrow \quad \frac{\partial n}{\partial \phi} = \frac{1}{V_{th}} n \quad \Longrightarrow \quad D_n = \mu_n V_{th},$$

where $V_{th} = \frac{k_B T}{q}$ is the *thermal voltage*.

In the following we will denote by $g_D(n)$ the diffusion enhancement factor representing the deviation from the classical Einstein relation:

$$g_D(n(\phi)) = \frac{1}{V_{th}} \frac{n}{\frac{\partial n}{\partial \phi}}, \tag{5.16}$$

so that

$$D_n = \mu_n V_{th} g_D(n(\phi)). \tag{5.17}$$

5.4. Constitutive relations for the Density of States

In the literature there is no definitive consensus as to the best choice for the shape of the DOS function g in eq. (5.11) for organic materials [Mad+15]. We assume it to belong to a family of given functions parametrized by a single parameter (*DOS width*, later denoted by σ) corresponding to the degree of molecular disorder of the semiconductor material. Several models have been proposed, including

1. a single symmetric Gaussian [FT09; Poe+13; Mar+09];

2. a linear combination of symmetric Gaussians [Kwo+12];

3. an exponential [VW11; Riv+11; RE11];

4. an asymmetric Gaussian [TM11];

5. a combination of a Gaussian and an exponential [Vri+13a; Cho+14];

6. others [VW09; Hul+04; Bar14].

However, the ansatz based on a single Gaussian is motivated by the physical plausibility in the case of organic materials [Wei+06] and will be adopted in the following. The corresponding DOS function is

$$g(\mathcal{E}) = \frac{N_0}{\sqrt{2\pi}\sigma} \exp\left(-\frac{\mathcal{E}^2}{2\sigma^2}\right),$$

where N_0 is the total number of available states (per unit volume) $\left[\text{m}^{-3}\right]$ and σ the disorder parameter [J], corresponding to the standard deviation of the Gaussian.

Thus eq. (5.11) becomes

$$n = \frac{N_0}{\sqrt{2\pi}\sigma} \int_{-\infty}^{+\infty} \exp\left(-\frac{(\mathcal{E} - \mathcal{E}_{\text{LUMO}})^2}{2\sigma^2}\right) \frac{1}{1 + \exp\left(\frac{\mathcal{E}-\mathcal{E}_F}{k_B T}\right)} \, d\mathcal{E}. \tag{5.18}$$

We aim at rewriting eq. (5.18) in order to exploit a Gaussian quadrature formula for efficiently computing the integrals in numerical simulations.
Through the substitution

$$\eta = \frac{\mathcal{E} - \mathcal{E}_{\text{LUMO}}}{\sqrt{2}\sigma} \tag{5.19}$$

eq. (5.18) becomes

$$n(\phi) = \mathcal{N}(\phi) = \frac{N_0}{\sqrt{\pi}} \int_{-\infty}^{+\infty} e^{-\eta^2} \left(1 + \exp\left(\frac{\sqrt{2}\sigma\eta - q\phi}{k_B T} \right) \right)^{-1} d\eta, \qquad (5.20)$$

where ϕ is the chemical potential introduced in section 5.3.

We also compute the functional derivatives of eq. (5.18) with respect to the electric potential φ and the chemical potential ϕ (of order 1 and 2), used in the application of a linearization scheme such as Newton's method. From eq. (5.18) we compute

$$\frac{\partial n}{\partial \varphi}(\varphi) = \frac{N_0}{\sqrt{2\pi}\sigma} \int_{-\infty}^{+\infty} \exp\left(-\frac{(\mathcal{E} + q\varphi)^2}{2\sigma^2} \right) \frac{1}{1 + \exp\left(\frac{\mathcal{E} - \mathcal{E}_F}{k_B T} \right)} \cdot \frac{-2(\mathcal{E} + q\varphi)q}{2\sigma^2} d\mathcal{E},$$

which, through eq. (5.19), becomes

$$\frac{\partial n}{\partial \varphi}(\varphi) = -\frac{N_0 q}{\sigma} \sqrt{\frac{2}{\pi}} \int_{-\infty}^{+\infty} \eta e^{-\eta^2} \left(1 + \exp\left(\frac{\sqrt{2}\sigma\eta - q\phi(\varphi)}{k_B T} \right) \right)^{-1} d\eta. \qquad (5.21)$$

Similarly, from eq. (5.20) we get

$$\frac{\partial n}{\partial \phi}(\phi) = \frac{N_0}{V_{th}\sqrt{\pi}} \int_{-\infty}^{+\infty} e^{-\eta^2} \frac{\exp\left(\frac{\sqrt{2}\sigma\eta - q\phi}{k_B T} \right)}{\left(1 + \exp\left(\frac{\sqrt{2}\sigma\eta - q\phi}{k_B T} \right) \right)^2} d\eta \qquad (5.22)$$

and

$$\frac{\partial^2 n}{\partial \phi^2}(\phi) = \frac{N_0}{V_{th}^2 \sqrt{\pi}} \int_{-\infty}^{+\infty} e^{-\eta^2} \frac{\exp\left(\frac{\sqrt{2}\sigma\eta - q\phi}{k_B T} \right)}{\left(1 + \exp\left(\frac{\sqrt{2}\sigma\eta - q\phi}{k_B T} \right) \right)^2} \left(\frac{2\exp\left(\frac{\sqrt{2}\sigma\eta - q\phi}{k_B T} \right)}{1 + \exp\left(\frac{\sqrt{2}\sigma\eta - q\phi}{k_B T} \right)} - 1 \right) d\eta.$$

$$(5.23)$$

A generalization of the above introduced Gaussian distribution to a class of parametric DOS shapes will be presented in the results discussed in chapter 12.

5.5. EGDM mobility model

In [Coe+05; VC08] is presented the Extended Gaussian Disorder Model (EGDM), which is valid for a single Gaussian DOS and proceeds on the assumption that on-site energies $\mathcal{E}_i$ in eq. (5.2) are Gaussian-distributed and have no spatial correlation. For materials where the energies are spatially correlated Bouhassoune et al. presented in [Bou+09] a modification of this model known as the Extended Correlated Disorder Model (ECDM). Both approaches determine the mobility (eq. (5.3)) starting from a numerical solution of the Master equation (5.1). For the EGDM the mobility has been shown to depend on:

1. the temperature T;

2. the charge carrier density n;

3. the component of the electric field in the direction of the motion of charge carriers $E_{\parallel} = \mathbf{E} \cdot \mathbf{J}_n$.

More specifically, it was found that only at high voltages and low temperatures the dependence on the field plays a role.

The complete EGDM model for the electron mobility coefficient reads [Coe+05; VC08]

$$\mu_n(T, n, E_{\parallel}) = \mu_{0,n}(T) \cdot g_1(n, T) \cdot g_2(E_{\parallel}, T), \tag{5.24}$$

where

$$\mu_{0,n}(T) = \bar{\mu}_{0,n} \exp\left(-c_0 \left(\frac{\sigma}{k_B T}\right)^2\right)$$

$$g_1(n) = \frac{N_0}{n} \exp\left[-\frac{(\varphi - \varphi_n)(n)}{V_{th}} + \frac{1}{2}\left(\frac{\sigma}{k_B T}\right)^2\right],$$

$$g_2(E_{\parallel}) = \exp\left\{0.44 \left[\left(\frac{\sigma}{k_B T}\right)^{3/2} - 2.2\right]\left[\sqrt{1 + 0.8 \min\left\{\frac{q E_{\parallel}}{N_0^{1/3}\sigma}, 2\right\}^2} - 1\right]\right\},$$

where
  c_0 is a dimensionless parameter;
  $\bar{\mu}_{0,n}$ is the low-field and low-charge-density mobility $\left[\mathrm{m^2 V^{-1} s^{-1}}\right]$.

This functional dependence leads to excellent agreement between calculated and measured Current-Voltage (IV) characteristics [Bou+09]. By a slight abuse of notation, we

will later refer to the function $\mu_{0,n}(T)$ as the low-field and low-charge-density mobility. The functions g_1, g_2 are called *enhancement factors*.

The value of $(\varphi - \varphi_n)(n)$ in the expression for g_1 can be computed by numerically inverting the relation (5.11), for example through a lookup table containing values of $n(\varphi - \varphi_n)$ and $g_1(\varphi - \varphi_n)$ predetermined at a given set of values of $(\varphi - \varphi_n)$: once constructed, $g_1(n)$ is given by interpolating the lookup table over the solution n of the DD equations.

The DOS width σ parameter and $\mu_{0,n}$ strongly affect the dynamics of the DD system because of the EGDM. However, it is often unfeasible to determine their value experimentally, which is why a parameter estimation problem has to be solved in order to completely close the DD system [Afr+17].

The EGDM model introduces further non-linearities into the DD system [Kna+10] because of the functional dependence of μ_n on the system variables n and φ, thus affecting the overall efficiency of non-linear iteration strategies. Therefore, standard solution schemes have to be properly adapted and generalized for taking into account the peculiar physical models of organic semiconductors.

In chapter 13 a numerical technique to address the identification of the σ and $\mu_{0,n}$ parameters will be presented.

5.6. Boundary conditions

5.6.1. Modeling charge injection

As charge carriers can not normally be introduced into organic semiconductor devices by doping with ionized impurities, as seen in section 4.3, usually all charges contributing to conduction originate from injection phenomena at metal-semiconductor interfaces [Tun14]. For this reason it is crucial, in order to correctly model current conduction in such devices, to be able to accurately describe charge injection. This problem mainly consists of a precise estimate of the value of the so-called *Schottky barrier*, *i.e.* the energy barrier that carriers have to overcome in order to flow from the metal to the semiconductor or vice-versa.

Out of thermal equilibrium, the electrical current flowing across the interface between a metal and a semiconductor is influenced by a discontinuity on the energy scale of the electronic states responsible for conduction in the two materials. Delocalized electronic states around the Fermi level are responsible for the electrical conduction in the metal, but these states are not coupled to any delocalized electronic state in the semiconductor, depending on the doping type: in n-type semiconductors the electrons near the LUMO are primarily responsible for electrical conduction and they are at an energy $-q\Phi_B$

(where Φ_B is the equivalent potential barrier) above the Fermi level. This energy offset is known as the Schottky barrier height and is such that the flow of electrons from the semiconductor to the metal is easier than the conduction in the opposite direction. The potential barrier can be expressed as

$$\Phi_B = -\frac{W_f - E_a}{q},\tag{5.25}$$

W_f being the metal work function, *i.e.* the minimum thermodynamic work needed to remove an electron from a solid to the vacuum immediately outside the solid surface, and E_a the semiconductor electron affinity, *i.e.* the minimum thermodynamic work needed to remove an electron from its LUMO level to the vacuum level.

Scott and Malliaras [SM99] also considered a mechanism of (thermionic) charge injection from metals into organic semiconductors, which plays an important role in devices such as OLEDs, where metal electrodes inject charge carriers into the opposite sides of the emissive organic layer, organic photoconductors (used in laser printers and photocopiers), where the photogenerated charge has to be extracted from the polymer film, and OTFTs too. Here the effect of the *image potential* (induced by charges in the metal) on injected carriers is modeled as a recombination activated from a Coulomb interaction through an hopping process. This means that, depending on the outward electric field at the metal-semiconductor interface $E = \nabla\varphi \cdot \nu$, where ν is the inward unit normal, the effective energy barrier can be larger or smaller than the nominal one Φ_B, and the deviation is modeled through a coefficient $\tilde{\Phi}(E)$ such that the effective barrier is $\Phi_B + V_{th}\tilde{\Phi}(E)$. Following the description in [BRG03], the coefficient $\tilde{\Phi}$ can be mathematically modeled as

$$\tilde{\Phi} = \begin{cases} \sqrt{f}, & \text{if } f \geq 0 \text{ (carrier injection)}, \\ f/4, & \text{if } f < 0 \text{ (carrier extraction)}, \end{cases}$$

where $f = qEr_c/(k_BT)$ is the reduced electric field and $r_c = q^2/(4\pi\varepsilon k_BT)$ the Coulomb radius.

Following [Afr+17; BRG03], charge injection phenomena are taken into account by imposing the following boundary condition on a contact $\Gamma_i \in C_{semic}$:

$$J_n \cdot \nu + q\,S(E)\left(n_{eq}(E) - n\right) = 0, \quad \text{on } \Gamma_i \in C_{semic},\tag{5.26}$$

where $C_{semic} \subseteq \partial\Omega$ is the set of boundary faces connected to any contact, ν the inward unit normal and $n_{eq}(E) = \mathcal{N}\left(\Phi_B + V_{th}\tilde{\Phi}(E)\right)$ is the equilibrium density value corresponding to the field E, computed through the DOS integral (5.20). The field-dependent

recombination velocity S in the injection regime ($f \geq 0$) is given by

$$S(f) = \frac{4\pi\varepsilon(k_BT)^2\mu_{0,n}}{q^3}\left(\frac{1}{\gamma^2(f)} - f\right), \qquad \gamma(f) = f^{-1} + f^{-\frac{1}{2}} - f^{-1}\left(1 + 2f^{\frac{1}{2}}\right)^{\frac{1}{2}},$$

while $S(f) = S(0) = \frac{1}{2}$ in the carrier extraction regime ($f < 0$).

A boundary condition consistent with (5.26) and imposed on the Poisson equation will be described in section 6.1.2.

5.6.2. External control circuit

We suppose that the device contacts are connected to an external control circuit. The circuit's evolution can be described by the Modified Nodal Analysis (MNA) equation obtained from the Kirchhoff's circuit laws and the constitutive relations for the electronic components connected to the circuit [Alì+03; ABG05]. It can be expressed in the form

$$A\dot{\mathbf{F}} + \mathbf{C}(\mathbf{F}) + r\mathbf{I} = 0, \tag{5.27}$$

where $\mathbf{F}$ is the state vector, containing the circuit variables (such as voltages, magnetic fluxes, currents, total charges, . . .), $\mathbf{I}$ the vector of the inward contact currents and r an incidence matrix, describing the connections among contacts and circuit pins. For the sake of simplicity, a linear model is assumed for $\mathbf{C}$, such that $\mathbf{C}(\mathbf{F}) = B\mathbf{F} + \mathbf{s}$. A and B are proper matrices and $\mathbf{s}$ is a source term. In particular we choose that the state vector $\mathbf{F}$ contains the contact voltages, that are imposed equal to the quasi-Fermi potential φ_n at each electric contact.

5.7. Computation of contact currents

The vector of currents $\mathbf{I}$ in eq. (5.27) is computed using the residue method [GS06], based on the property of local conservation [Hug+00] which holds for discretization schemes derived from the Galërkin method (such as finite elements and finite volumes).

Let $C = C_{\text{semic}} \cup C_{\text{ins}} \subseteq \partial\Omega$ be the set of boundary faces connected to any device contact lying on the semiconductor or the insulator region, respectively. The total current density at the i-th contact $\Gamma_i \in C$ is the sum of two contributions, namely the displacement and the conduction current:

$$I_i = \int_{\Gamma_i} \frac{\partial\,(\mathbf{D}\cdot\mathbf{v})}{\partial t} + \int_{\Gamma_i} \mathbf{J}_n\cdot\mathbf{v}, \tag{5.28}$$

where $\mathbf{D} = -\varepsilon\nabla\varphi$ is the electric displacement field $\left[C\cdot m^{-2}\right]$ and $\mathbf{v}$ the inward unit normal.

5.7.0.1. Displacement current

Assuming for the sake of simplicity that homogeneous conditions are imposed on Dirichlet boundary Γ_D (otherwise a standard lifting procedure can be applied), the variational formulation of the Poisson equation (5.5) reads

$$\forall t \in [0, T] \text{ find } \varphi(t) \in V \text{ such that}$$

$$\int_\Omega \varepsilon \nabla \varphi \cdot \nabla \gamma + \int_{\partial \Omega} \varepsilon \nabla \varphi \cdot \mathbf{v} \, \gamma + \int_\Omega qn\gamma = 0, \quad \forall \gamma \in V,$$

where $V = \left\{ v \in H^1(\Omega) : v|_{\Gamma_D} = 0 \right\}$.

Since the Galërkin method is locally conservative [Hug+00], we can choose γ among the basis functions associated with the degrees of freedom lying on Γ_i [GS06], so that

$$-\int_{\Gamma_i} \varepsilon \nabla \varphi \cdot \mathbf{v} = \sum_k \left(\int_\Omega \varepsilon \nabla \varphi \cdot \nabla \gamma_k + \int_\Omega qn\gamma_k \right),$$

where the summation loop over all the basis functions $\gamma_k \in H^1(\Omega)$ such that $\gamma_k(\mathbf{x}_j) = \delta_{jk}, \forall \mathbf{x}_j \in \Gamma_i$.

Therefore, the displacement current density can be computed as

$$\int_{\Gamma_i} \frac{\partial (\mathbf{D} \cdot \mathbf{v})}{\partial t} = \sum_k \left(\int_\Omega \varepsilon \nabla \frac{\partial \varphi}{\partial t} \cdot \nabla \gamma_k + \int_\Omega q \frac{\partial n}{\partial t} \gamma_k \right).$$

We remark that the k-th term of the summation can be numerically computed as the multiplication of the k-th row of the resulting stiffness and mass matrices (obtained by the discrete formulation before imposing the boundary conditions) by the discrete state vectors associated with $\frac{\partial \varphi}{\partial t}$ and $\frac{\partial n}{\partial t}$.

5.7.0.2. Conduction current

Following an analogous derivation than the one in the previous section, the variational formulation of the continuity equation eq. (5.7) reads

$$\forall t \in [0, T] \text{ find } n(t) \in H^1(\Omega) \text{ such that}$$

$$\int_\Omega \frac{\partial n}{\partial t} \gamma + \frac{1}{q} \int_\Omega \mathbf{J}_n \cdot \nabla \gamma + \frac{1}{q} \int_{\partial \Omega} (\mathbf{J}_n \cdot \mathbf{v} \, \gamma) = 0, \quad \forall \gamma \in H^1(\Omega).$$

Rearranging the terms enables to compute the conduction current density as

$$\int_{\Gamma_i} \mathbf{J}_n \cdot \mathbf{v} = \sum_k \left(\int_\Omega \frac{\partial n}{\partial t} \gamma_k + \frac{1}{q} \int_\Omega \mathbf{J}_n \cdot \nabla \gamma_k \right).$$

Again, the volume integrals appearing in this last expression can be numerically computed starting from the discrete formulation of the problem.

6. A consistent hierarchy of mathematical models

6.1. Transient regime

6.1.1. Thermodynamic consistency equation

As will be discussed in more detail in chapter 9, in order to allow for a better numerical treatment it is convenient to reformulate the DD equations (5.5) and (5.7) by introducing an additional unknown that has the physical dimensions of an electric potential and accounts for the deviation from the classical Einstein relation.

A motivation for the derivation presented below, that descends directly from the pioneering work of [VDM73], is also given in [AFN19].

The derivation of this relation comes from observing that the discretization method used, namely the Scharfetter-Gummel scheme, relies on rewriting the continuity equation in terms of Slotboom variables:

$$n = \rho \exp\left(\frac{\varphi - \varphi_n}{V_{th}}\right), \tag{6.1}$$

for a proper function ρ, which corresponds to a *Maxwell-Boltzmann*-like relation.

For more general statistical distributions, like the one presented in eq. (5.20), n is related to φ and φ_n through a general constitutive law of the form

$$n = \mathcal{N}(\varphi - \varphi_n) = N_0 \cdot \hat{\mathcal{N}}(\varphi - \varphi_n), \tag{6.2}$$

where N_0 is the total volume density of available energetic states. In general, consistency between the discretization scheme and such a constitutive law is desirable. However, the Scharfetter-Gummel scheme does not satisfy this requirement *per se*. Several approaches in this direction, that are valid only for specific density distributions such as approximations of the Fermi-Dirac statistics, have been proposed: they make use of a proper average of the diffusion coefficient over the mesh cells or on the solution of local non-linear boundary-value problems [KG13; Kop+14; Kop+15].

For general distribution functions it is not possible to find simple fixed point equations for the unknown current [Far+18]. For this reason physically motivated approximate fluxes are usually employed. The so-called modified Scharfetter-Gummel methods, namely those based on diffusion enhanced schemes, preserve the Scharfetter-Gummel structure and remain thermodynamically consistent.

We will propose hereafter an approach that, following the spirit of [VDM73], solves the issue of having a consistent discrete model and that is valid for a generic DOS function.

In order to make eqs. (6.1) and (6.2) consistent, we introduce an additional potential ψ (later referred to as *consistency potential* or *enhancement potential*) by imposing

$$n = N_0 \exp\left(\frac{\varphi - \varphi_n + \psi}{V_{th}}\right),$$ (6.3)

following the choice $\rho = N_0 \exp(\psi/V_{th})$. The consistency potential ψ has been introduced and chosen such to convey all the information provided by the DOS function $\mathcal{N}$ into the Scharfetter-Gummel relation (6.1).

Applying the gradient operator to the previous relation yields

$$\nabla n = \frac{n}{V_{th}} \nabla(\varphi - \varphi_n + \psi),$$

which reads

$$n \nabla \varphi_n = -V_{th} \nabla n + n \nabla(\varphi + \psi),$$

so that the current density (5.8) becomes

$$J_n = q \mu_n n \nabla \varphi_n = -q V_{th} \mu_n \left(\nabla n - n \nabla\left(\frac{\varphi + \psi}{V_{th}}\right)\right).$$ (6.4)

In this expression the diffusion and the mobility coefficients are related through a *Maxwell-Boltzmann*-like relation and the drift term takes into account the additional contribution given by the potential ψ. The thermodynamical consistence of this formulation will be proved in theorem 9.1. We also remark that this approach, compared to the ones in [Fuh15; Pat+18], is more effective from a computational point of view since equation (6.3) for the enhancement potential ψ is local and its discretization results in diagonal blocks.

6.1.2. Complete Drift-Diffusion system

$$\begin{cases} -\nabla \cdot (\varepsilon \nabla \varphi) + qn = 0, & \text{in } \Omega, \\[2mm] \dfrac{\partial n}{\partial t} - \dfrac{1}{q} \nabla \cdot \mathbf{J_n} = 0, & \text{in } \Omega_{\text{semic}}, \\[2mm] n - \mathcal{N} \left(V_{\text{th}} \log \left(\dfrac{n}{N_0} \right) - \psi \right) = 0, & \text{in } \Omega_{\text{semic}}, \\[2mm] A\dot{\mathbf{F}} + \mathbf{C}(\mathbf{F}) + r\mathbf{I} = 0, \\[2mm] I_i - \displaystyle\int_{\Gamma_i} \dfrac{\partial \left(\mathbf{D} \cdot \mathbf{v} \right)}{\partial t} - \int_{\Gamma_i} \mathbf{J_n} \cdot \mathbf{v} = 0, & \forall \Gamma_i \in \mathcal{C}, \end{cases} \tag{6.5}$$

where $\mathcal{C} = \mathcal{C}_{\text{semic}} \cup \mathcal{C}_{\text{ins}} \subseteq \partial\Omega$ is the set of boundary faces connected to any device contact lying on the semiconductor or the insulator region, respectively.

Let F_i the circuit state variable representing the electric potential at the contact Γ_i. Then the Drift-Diffusion system is coupled with the following boundary conditions:

$$\begin{cases} \varphi - F_i - \left(V_{\text{th}} \log \left(\dfrac{n}{N_0} \right) - \psi \right) = 0, & \text{on } \Gamma_i \in \mathcal{C}_{\text{semic}}, \\[2mm] \varphi - F_i = 0, & \text{on } \Gamma_i \in \mathcal{C}_{\text{ins}}, \\[2mm] \nabla \varphi \cdot \mathbf{v} = 0, & \text{on } \partial\Omega \setminus \mathcal{C}, \\[2mm] \mathbf{J_n} \cdot \mathbf{v} + q\, S(E) \left(n_{\text{eq}} - n \right) = 0, & \text{on } \Gamma_i \in \mathcal{C}_{\text{semic}}, \\[2mm] \mathbf{J_n} \cdot \mathbf{v} = 0, & \text{on } \partial\Omega_{\text{semic}} \setminus \mathcal{C}_{\text{semic}}, \end{cases} \tag{6.6}$$

where

$$n_{\text{eq}} = \mathcal{N} \left(\Phi_B + V_{\text{th}} \tilde{\Phi}(E) \right).$$

6.2. Thermal equilibrium regime

In the thermal equilibrium regime the following relation holds:

$$\mathbf{J_n} = \mathbf{0},$$

which implies that $\nabla \varphi_n = 0$, *i.e.* the quasi-Fermi potential φ_n is constant and can be arbitrarily chosen such that

$$\varphi_n = 0.$$

Under this assumption eq. (6.2) becomes

$$n = \mathcal{N}(\varphi)$$

while eq. (6.3) can be rewritten as

$$n = N_0 \exp\left(\frac{\varphi + \psi}{V_{th}}\right) \implies \psi = V_{th} \log\left(\frac{n}{N_0}\right) - \varphi,$$

Finally, the boundary conditions become:

$$\begin{cases} \varphi - F = 0, & \text{on } \Gamma_{ins}, \\ \varphi - F - \left(V_{th} \log\left(\frac{n}{N_0}\right) - \psi\right) = 0, & \text{on } \Gamma_{semic}, \\ \mathbf{J}_n \cdot \mathbf{v} = 0, & \text{on } \bar{\Omega}_{ins} \cap \bar{\Omega}_{semic}, \\ n = n_{eq}, & \text{on } \Gamma_{semic}. \end{cases}$$

Two possible equilibrium models for the electric potential can be chosen in order to guarantee consistence with the transient model and to provide consistent boundary conditions, namely

$$\begin{cases} -\nabla \cdot (\varepsilon \nabla \varphi) + n = 0, & \text{in } \Omega, \\ n = \mathcal{N}(\varphi), & \text{in } \Omega_{semic}, \\ \psi - \left(V_{th} \log\left(\frac{n}{N_0}\right) - \varphi\right) = 0, & \text{in } \Omega_{semic}, \\ \varphi - F = 0, & \text{on } \Gamma_{ins}, \\ \varphi - F - \left(V_{th} \log\left(\frac{n}{N_0}\right) - \psi\right) = 0, & \text{on } \Gamma_{semic}, \end{cases}$$

which has a Dirichlet-type boundary condition on Γ_{semic}, or

$$\begin{cases} -\nabla \cdot (\varepsilon \nabla \varphi) + n = 0, & \text{in } \Omega, \\ n = \mathcal{N}(\varphi), & \text{in } \Omega_{semic}, \\ \varphi - F = 0, & \text{on } \Gamma_{ins}, \\ \varphi - F - \left(\Phi_B + V_{th} \tilde{\Phi}(\nabla \varphi)\right) = 0, & \text{on } \Gamma_{semic}, \end{cases} \tag{6.7}$$

which can be solved at a cheaper computational effort, since it does not require to compute the enhancement potential ψ, but is characterized by a Robin boundary condition on Γ_{semic} that hampers the symmetry of the resulting linear system.

In the implementation of the numerical code for equilibrium simulations we adopted the latter model, in what follows referred to as Non-Linear Poisson (NLP) equation, as it consists only of a PDE for the electric potential φ coupled to a set of non-linear algebraic constraints.

6.3. Time-harmonic regime

In engineering applications, it is often required to simulate the behavior of a device controlled by an input signal which is periodic in time. Such mode of operation is usually referred to as the Alternating Current (AC) regime. In this regime a possibly large stationary bias is usually applied, and then perturbed by an additional time-harmonic signal, small enough that the resulting response of the device may be modeled as linear. Let us for example assume that a generic contact $\Gamma_i \in C$, for example the gate contact, is connected to a sinusoidal voltage generator of the form

$$F_i(t) = \bar{V} + V_0 \sin(\omega_0 t), \tag{6.8}$$

centered at a given voltage $\bar{V}$ and with amplitude V_0 and angular frequency ω_0 over a timespan $[t_{min}, t_{max}]$.

While it is possible, and indeed common, to simulate this regime of operation by solving the DD system imposing eq. (6.8) as a general time-dependent boundary condition on Γ_i through the control circuit equation, as described in section 6.3.1, it is convenient to exploit the quasi-linear device behavior and to perform the simulation directly in the frequency domain as discussed in section 6.3.2. In both cases the computation of the device equivalent capacitance follows from the assumption that the simulated current I_i flowing through the generator F_i is equivalent to the one flowing through a parallel RC circuit with resistance R_p, capacitance C_p and voltage generator F_i, as shown in fig. 6.1.

6.3.1. Simulating the transient DD system

If the contact controlled by the sinusoidal signal is an insulator gate contact while other contacts are kept grounded, the device behavior is essentially that of a voltage controlled capacitor with capacitance C_p, depending on the bias voltage and the frequency, connected in parallel to a bias-dependent resistance R_p, as shown in fig. 6.1.

The total current flowing through the equivalent circuit is

$$I_i = \frac{V_0}{R_p} \sin(\omega_0 t) + V_0 \omega_0 C_p \cos(\omega_0 t),$$

which yields

$$R_p = \frac{V_0}{c_1}, \qquad C_p = \frac{c_2}{V_0 \omega_0},$$
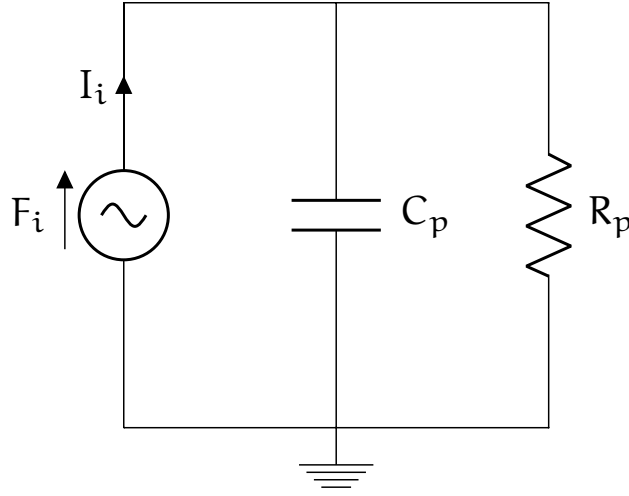
Figure 6.1.: Equivalent parallel RC circuit.

where

$$c_1 = \frac{\int_{t_{min}}^{t_{max}} I_i(t) \sin(\omega_0 t)\, dt}{\int_{t_{min}}^{t_{max}} \sin(\omega_0 t)^2\, dt}, \qquad c_2 = \frac{\int_{t_{min}}^{t_{max}} I_i(t) \cos(\omega_0 t)\, dt}{\int_{t_{min}}^{t_{max}} \cos(\omega_0 t)^2\, dt}.$$

Then the equivalent capacitance C_p is easily computed once the numerical simulation has provided the current $I_i(t)$.

If the dielectric permittivity ε_{ins} of an insulator, as is the case of materials of relevant application, is modeled as a frequency-dependent parameter, the DD system has to be complemented by a differential equation for the dipole moment $\mathbf{p}_j$ of the j-th molecule in order to describe the evolution of ε in the time domain [Gri05a]:

$$\ddot{\mathbf{p}}_j + \gamma_j \dot{\mathbf{p}}_j + \varpi_j^2 \mathbf{p}_j = -\frac{q^2 \mathbf{E}}{m},$$

where m is the mass of the electron, γ_j, ϖ_j are material-dependent constants and $\mathbf{E}$ is the electric field acting on the molecule. In an isotropic medium the relation between $\mathbf{p}_j$ and ε is expressed by

$$N_{mol} \sum_{j=1}^{N_{mol}} \mathbf{p}_j = (\varepsilon - \varepsilon_0)\mathbf{E}$$

where N_{mol} is the total number of molecules.

6.3.2. Analysis in the frequency domain

The approach presented in the previous section is not computationally efficient, since estimating the device equivalent capacitance and resistance C_p and R_p at different frequencies requires to repeat the complete transient simulation for all the needed values of ω_0. Here we present an alternative approach based on a Fourier analysis.

The aim is to linearize the system around the equilibrium point $F_i = \bar{V}$, *i.e.* the point the sinusoidal voltage is centered at. Let $\bar{u} = [\bar{\varphi}, \bar{n}, \bar{\psi}, \bar{F}, \bar{I}]^T$ be the equilibrium solution to the DD system (6.5) with boundary conditions (6.6) such that $F_i = \bar{V}$ on Γ_i. Then this equilibrium solution is such that:

$$\frac{\partial \bar{u}}{\partial t} = 0, \qquad \bar{I} = 0.$$

In order to derive the linearized system, we assume that the state solution obtained by perturbing the boundary condition on Γ_i by an increment $\delta F_i = \delta \bar{V} = V_0 \sin(\omega_0 t)$ is $\bar{u} + \delta u$. Then the solution increment $\delta u = [\delta \varphi, \delta n, \delta \psi, \delta F, \delta I]^T$ satisfies the following system:

$$\begin{cases} -\nabla \cdot (\varepsilon \nabla \delta \varphi) + q \delta n = 0, & \text{in } \Omega, \\[2mm] \dfrac{\partial (\delta n)}{\partial t} - \dfrac{1}{q} \nabla \cdot \delta J_n = 0, & \text{in } \Omega_{\text{semic}}, \\[2mm] \delta_n + \dfrac{\partial \mathcal{N}}{\partial (\varphi - \varphi_n)} \left(V_{\text{th}} \log \left(\dfrac{\bar{n}}{N_0} \right) - \bar{\psi} \right) \cdot \left(\dfrac{V_{\text{th}}}{\bar{n}} \delta n + \delta \psi \right) = 0, & \text{in } \Omega_{\text{semic}}, \\[2mm] A \dot{\delta F} + B \delta F + r \delta I = -\bar{s} \delta \bar{V}, \\[2mm] \delta I_i - \displaystyle\int_{\Gamma_i} \dfrac{\partial (\delta D \cdot v)}{\partial t} - \int_{\Gamma_i} \delta J_n \cdot v = 0, & \forall \Gamma_i \in C, \end{cases} \quad (6.9)$$

where δJ_n and δD denote the functional differentials of J_n and D, respectively, at $\bar{u}$ in the direction δu, with proper homogeneous boundary conditions. The linearization of the circuit equation has been performed by expliciting the dependence on $\bar{V}$:

$$C(F) = BF + \hat{s} + \bar{s} \bar{V},$$

where $\bar{s} = s / \bar{V}$. The quantity $\hat{s} = s - \bar{s} \bar{V}$ does not depend on $\bar{V}$.

After applying an arbitrary discretization scheme and remarking that $\delta \bar{V} = \delta F_i$, system (6.9) can be rewritten in compact algebraic form as

$$M \dot{U} + J U = -f \delta F_i, \quad (6.10)$$

where $\mathbf{U}$ is the state solution vector of the degrees of freedom corresponding to the discretization scheme adopted, M is a mass matrix multiplying the time-derivative terms, J the spatial Jacobian matrix. The right-hand side is the residual of the perturbed circuit equation, where $\mathbf{f}$ is a vector whose j-th component is 1 if j is the global degree of freedom of the circuit variable F_i and 0 otherwise.

Computing symbolically the Fourier transform of eq. (6.10) at a generic frequency ω provides

$$\jmath\omega\mathsf{M}\widehat{\mathbf{U}} + \mathsf{J}\widehat{\mathbf{U}} = -\mathbf{f}\widehat{\delta F}_i,$$

where the hat denotes the Fourier transformed vector at $\jmath\omega$ and $\jmath$ is the imaginary unit. This latter expression can be rewritten as

$$\widehat{\mathbf{U}} = -\left((\jmath\mathsf{M} + \mathsf{J})^{-1}\mathbf{f}\right)\widehat{\delta F}_i,$$

The transfer function between the perturbation of the applied voltage $\widehat{\delta F}_i$ and the perturbation of the corresponding current $\widehat{\delta I}_i$ in the frequency domain is

$$\frac{\widehat{\delta I}_i}{\widehat{\delta F}_i}(\jmath\omega) = -\left((\jmath\mathsf{M} + \mathsf{J})^{-1}\mathbf{f}\right)\cdot\mathbf{i}, \tag{6.11}$$

where $\mathbf{i}$ is a vector whose j-th component is 1 if j is the global degree of freedom of the circuit current I_i and 0 otherwise.

Since this expression was derived from a linear model, we can assume that the transfer function eq. (6.11) is equivalent to the one of the parallel RC circuit in fig. 6.1 by imposing the equality

$$\frac{\widehat{\delta I}_i}{\widehat{\delta F}_i}(\jmath\omega) = \frac{1}{R_p} + \jmath\omega C_p,$$

to obtain, after simple algebraic steps, the equivalent resistance and capacitance

$$R_p = \frac{\sqrt{1 + \tan(\angle T)^2}}{|T|}, \quad C_p = \frac{\tan(\angle T)}{\omega_0 R_p}, \tag{6.12}$$

where $|T|$ and $\angle T$ denote the modulus and the argument, respectively, of the complex number $T = \frac{\widehat{\delta I}_i}{\widehat{\delta F}_i}(\jmath\omega_0)$, *i.e.* the numerical transfer function evaluated at the actual frequency ω_0.

References

[ABG05]   G. Alì, A. Bartel, and M. Günther. "Parabolic Differential-Algebraic Models in Electrical Network Design". In: *Multiscale Modeling & Simulation* 4.3 (2005), pp. 813–838 (cit. on p. 56).

[AFN19]   P. C. Africa, C. de Falco, and D. Natali. "A Note on Thermodynamically Consistent Flux Discretization". In: *In preparation* (2019) (cit. on pp. 23, 59, 93).

[Afr+17]   P. C. Africa, C. de Falco, F. Maddalena, M. Caironi, and D. Natali. "Simultaneous Extraction of Density of States Width, Carrier Mobility and Injection Barriers in Organic Semiconductors". In: *Scientific Reports* 7.1 (2017), p. 3803 (cit. on pp. 23, 54, 55, 161).

[Alì+03]   G. Alì, A. Bartel, M. Günther, and C. Tischendorf. "Elliptic Partial Differential-Algebraic Multiphysics Models in Electrical Network Design". In: *Mathematical Models and Methods in Applied Sciences* 13.09 (2003), pp. 1261–1278 (cit. on p. 56).

[AM88]   N. W. Ashcroft and N. D. Mermin. *Solid State Physics*. Holt, Rinehart and Winston, New York, 1988 (cit. on p. 49).

[And78]   P. W. Anderson. "Local Moments and Localized States". In: *Reviews of Modern Physics* 50.2 (1978), p. 191 (cit. on p. 39).

[AR00]   A. M. Anile and V. Romano. "Hydrodynamical Modeling of Charge Carrier Transport in Semiconductors". In: *Meccanica* 35.3 (2000), pp. 249–296 (cit. on p. 38).

[AR99]   A. M. Anile and V. Romano. "Non Parabolic Band Transport in Semiconductors: Closure of the Moment Equations". In: *Continuum Mechanics and Thermodynamics* 11.5 (1999), pp. 307–325 (cit. on p. 38).

[Bar14]   S. D. Baranovskii. "Theoretical Description of Charge Transport in Disordered Organic Semiconductors". In: *Physica Status Solidi (b)* 251.3 (2014), pp. 487–525 (cit. on pp. 51, 171, 172).

References

[Bäs93]   H. Bässler. "Charge Transport in Disordered Organic Photoconductors, a Monte Carlo Simulation Study". In: *Physica Status Solidi (b)* 175 (1993) (cit. on p. 44).

[Bou+09]   M. Bouhassoune, S. L. M. v. Mensfoort, P. A. Bobbert, and R. Coehoorn. "Carrier-density and Field-dependent Charge-carrier Mobility in Organic Semiconductors with Correlated Gaussian Disorder". In: *Organic Electronics: Physics, Materials, Applications* 10.3 (2009), pp. 437–445 (cit. on pp. 44, 53, 171).

[BRG03]   J. A. Barker, C. M. Ramsdale, and N. C. Greenham. "Modeling the Current-voltage Characteristics of Bilayer Polymer Photovoltaic Devices". In: *Physical Review B* 67.7 (2003), p. 075205 (cit. on p. 55).

[CB12]   R. Coehoorn and P. A. Bobbert. "Effects of Gaussian Disorder on Charge Carrier Transport and Recombination in Organic Semiconductors". In: *Physica Status Solidi (a)* 209.12 (2012), pp. 2354–2377 (cit. on pp. 38, 172).

[Cho+14]   W. Choi, T. Miyakai, T. Sakurai, A. Saeki, M. Yokoyama, and S. Seki. "Non-contact, Non-destructive, Quantitative Probing of Interfacial Trap Sites for Charge Carrier Transport at Semiconductor-insulator Boundary". In: *Applied Physics Letters* 105.3, 033302 (July 22, 2014) (cit. on p. 51).

[Coe+05]   R. Coehoorn, W. F. Pasveer, P. A. Bobbert, and M. A. J. Michels. "Charge-carrier Concentration Dependence of the Hopping Mobility in Organic Materials with Gaussian Disorder". In: *Physical Review B* 72.15 (15 2005), p. 155206 (cit. on pp. 53, 162).

[ES99]   A. Einstein and M. von Smoluchowski. "Untersuchungen über Die Theorie Der Brownschen Bewegung/abhandlungen über Die Brownsche Bewegung Und Verwandte Erscheinungen". In: *Harri Deutsch, Frankfurt* 3 (1999) (cit. on p. 50).

[Far+18]   P. Farrell, M. Patriarca, J. Fuhrmann, and T. Koprucki. "Comparison of Thermodynamically Consistent Charge Carrier Flux Discretizations for Fermi-Dirac and Gauss-Fermi Statistics". In: *Optical and Quantum Electronics* 50.2 (2018), p. 101 (cit. on p. 60).

[FT09]   J. A. Freire and C. Tonezer. "Density of States and Energetic Correlation in Disordered Molecular Systems Due to Induced Dipoles". In: *The Journal of Chemical Physics* 130.13, 134901 (Apr. 1, 2009) (cit. on p. 51).

[Fuh15]   J. Fuhrmann. "Comparison and Numerical Treatment of Generalised Nernst-Planck Models". In: *Computer Physics Communications* 196 (2015), pp. 166–178 (cit. on p. 60).

[Gri05a]   D. J. Griffiths. *Introduction to Electrodynamics*. AAPT, 2005 (cit. on p. 64).

[Gri05b]   D. J. Griffiths. *Introduction to Quantum Mechanics*. Pearson Education India, 2005 (cit. on p. 39).

[GS06]   R. Gusmeroli and A. S. Spinelli. "Accurate Boundary Integral Calculation in Semiconductor Device Simulation". In: *IEEE Transactions on Electron Devices* 53.7 (2006), pp. 1730–1733 (cit. on pp. 56, 57).

[Hec11]   J. Hecht. *Understanding Lasers: An Entry-level Guide*. Vol. 21. John Wiley & Sons, 2011 (cit. on p. 38).

[Hug+00]   T. J. R. Hughes, G. Engel, L. Mazzei, and M. G. Larson. "The Continuous Galerkin Method Is Locally Conservative". In: *Journal of Computational Physics* 163.2 (2000), pp. 467–488 (cit. on pp. 56, 57).

[Hul+04]   I. N. Hulea, H. B. Brom, A. J. Houtepen, D. Vanmaekelbergh, J. J. Kelly, and E. A. Meulenkamp. "Wide Energy-window View on the Density of States and Hole Mobility in Poly(p-phenylene Vinylene)". In: *Physical Review Letters* 93.16, 166601 (Oct. 15, 2004) (cit. on p. 51).

[Jac99]   J. D. Jackson. *Classical Electrodynamics*. 3rd ed. John Wiley & Sons, 1999 (cit. on p. 45).

[Jer96]   J. W. Jerome. *Analysis of Charge Transport: A Mathematical Study of Semiconductor Devices*. 1996 (cit. on p. 38).

[Kax03]   E. Kaxiras. *Atomic and Electronic Structure of Solids*. Cambridge University Press, 2003 (cit. on p. 38).

[KB15]   A. Köhler and H. Bässler. *Electronic Processes in Organic Semiconductors: An Introduction*. John Wiley & Sons, 2015 (cit. on p. 47).

[KG13]   T. Koprucki and K. Gärtner. "Discretization Scheme for Drift-diffusion Equations with Strong Diffusion Enhancement". In: *Optical and Quantum Electronics* 45.7 (2013), pp. 791–796 (cit. on p. 59).

[Kit08]   C. Kittel. *Introduction to Solid State Physics*. Wiley, 2008 (cit. on p. 48).

[Kna+10]   E. Knapp, R. Häusermann, H. U. Schwarzenbach, and B. Ruhstaller. "Numerical Simulation of Charge Transport in Disordered Organic Semiconductor Devices". In: *Journal of Applied Physics* 108.5 (2010), p. 054504 (cit. on p. 54).

References

[Kop+14]   T. Koprucki, M. Kantner, J. Fuhrmann, and K. Gärtner. "On Modifications of the Scharfetter-Gummel Scheme for Drift-diffusion Equations with Fermi-like Statistical Distribution Functions". In: *Numerical Simulation of Optoelectronic Devices, 2014.* 2014, pp. 155–156 (cit. on p. 59).

[Kop+15]   T. Koprucki, N. Rotundo, P. Farrell, D. H. Doan, and J. Fuhrmann. "On Thermodynamic Consistency of a Scharfetter-Gummel Scheme Based on a Modified Thermal Voltage for Drift-diffusion Equations with Diffusion Enhancement". In: *Optical and Quantum Electronics* 47.6 (2015), pp. 1327–1332 (cit. on p. 59).

[Kwo+12]   S. Kwon, K.-R. Wee, J. W. Kim, C. Pac, and S. O. Kang. "Effects of Intermolecular Interaction on the Energy Distribution of Valance Electronic States of a Carbazole-based Material in Amorphous Thin Films". In: *The Journal of Chemical Physics* 136.20, 204706 (2012) (cit. on p. 51).

[MA60]   A. Miller and E. Abrahams. "Impurity Conduction at Low Concentrations". In: *Physical Review* 120.3 (1960), p. 745 (cit. on p. 43).

[Mad+15]   F. Maddalena, C. de Falco, M. Caironi, and D. Natali. "Assessing the Width of Gaussian Density of States in Organic Semiconductors". In: *Organic Electronics* 17 (2015), pp. 304–318 (cit. on pp. 30, 47, 51, 161–164, 168, 170, 173, 175, 177).

[Mad95]   O. Madelung. *Introduction to Solid-state Theory.* Vol. 2. Springer Science & Business Media, 1995 (cit. on p. 49).

[Mar+09]   N. G. Martinelli, M. Savini, L. Muccioli, Y. Olivier, F. Castet, C. Zannoni, D. Beljonne, and J. Cornil. "Modeling Polymer Dielectric/pentacene Interfaces: On the Role of Electrostatic Energy Disorder on Charge Carrier Mobility". In: *Advanced Functional Materials* 19.20 (2009), pp. 3254–3261 (cit. on p. 51).

[Mar86]   P. A. Markowich. *The Stationary Semiconductor Device Equations.* Vol. 1. Springer Science & Business Media, 1986 (cit. on p. 46).

[Mei+06]   K. D. Meisel, W. F. Pasveer, J. Cottaar, C. Tanase, R. Coehoorn, P. A. Bobbert, P. W. M. Blom, D. M. de Leeuw, and M. A. J. Michels. "Charge-carrier Mobilities in Disordered Semiconducting Polymers: Effects of Carrier Density and Electric Field". In: *Physica Status Solidi (c)* 3.2 (2006), pp. 267–270 (cit. on p. 43).

[MRS90]   P. A. Markowich, C. A. Ringhofer, and C. Schmeiser. *Semiconductor Equations.* 1990 (cit. on p. 38).

[Pat+18]   M. Patriarca, P. Farrell, J. Fuhrmann, and T. Koprucki. "Highly Accurate Quadrature-based Scharfetter-Gummel Schemes for Charge Transport in Degenerate Semiconductors". In: *Computer Physics Communications* (2018) (cit. on p. 60).

[Poe+13]   C. Poelking, E. Cho, A. Malafeev, V. Ivanov, K. Kremer, C. Risko, J. Brédas, and D. Andrienko. "Characterization of Charge-carrier Transport in Semicrystalline Polymers: Electronic Couplings, Site Energies, and Charge-carrier Dynamics in Pbttt". In: *The Journal of Physical Chemistry C* 117.4 (2013), pp. 1633–1640 (cit. on p. 51).

[PS99]   M. Pope and C. E. Swenberg. *Electronic Processes in Organic Crystals and Polymers*. Oxford University Press on Demand, 1999 (cit. on p. 41).

[RE11]   M. Raja and B. Eccleston. "The Significance of Debye Length in Disordered Doped Organic Devices". In: *Journal of Applied Physics* 110.11, 114524 (Dec. 13, 2011) (cit. on p. 51).

[Riv+11]   J. Rivnay, R. Noriega, J. E. Northrup, R. J. Kline, M. F. Toney, and A. Salleo. "Structural Origin of Gap States in Semicrystalline Polymers and the Implications for Charge Transport". In: *Physical Review B* 83.12, 121306 (Mar. 16, 2011) (cit. on p. 51).

[SBS81]   G. Schönherr, H. Bässler, and M. Silver. "Dispersive Hopping Transport Via Sites Having a Gaussian Distribution of Energies". In: *Philosophical Magazine B* 44.1 (1981), pp. 47–61 (cit. on p. 44).

[Sel12]   S. Selberherr. *Analysis and Simulation of Semiconductor Devices*. Springer Science & Business Media, 2012 (cit. on p. 48).

[SM99]   J. C. Scott and G. G. Malliaras. "Charge Injection and Recombination at the Metal-organic Interface". In: *Chemical Physics Letters* 299.2 (1999), pp. 115–119 (cit. on p. 55).

[TM11]   A. K. Tripathi and Y. N. Mohapatra. "Correlation of Photocurrent and Electroabsorption Spectra and Their Temperature Dependence for Conjugated Light Emitting Polymers: The Origin of the Corresponding Density of States". In: *Physical Review B* 84.20, 205213 (Nov. 18, 2011) (cit. on p. 51).

[Tun14]   R. T. Tung. "The Physics and Chemistry of the Schottky Barrier Height". In: *Applied Physics Reviews* 1.1 (2014), p. 011304 (cit. on p. 54).

References

[VC08]   S. L. M. Van Mensfoort and R. Coehoorn. "Effect of Gaussian Disorder on the Voltage Dependence of the Current Density in Sandwich-type Devices Based on Organic Semiconductors". In: *Physical Review B* 78.8 (2008), p. 085207 (cit. on pp. 53, 172).

[VDM73]   R. J. Van Overstraeten, H. J. DeMan, and R. P. Mertens. "Transport Equations in Heavy Doped Silicon". In: *IEEE Transactions on Electron Devices* 20.3 (1973), pp. 290–298 (cit. on pp. 59, 60).

[Vri+13a] R. J. de Vries, A. Badinski, R. A. J. Janssen, and R. Coehoorn. "Extraction of the Materials Parameters That Determine the Mobility in Disordered Organic Semiconductors from the Current-voltage Characteristics: Accuracy and Limitations". In: *Journal of Applied Physics* 113.11, 114505 (Mar. 19, 2013) (cit. on p. 51).

[VW09]   N. Vukmirović and L.-W. Wang. "Charge Carrier Motion in Disordered Conjugated Polymers: A Multiscale Ab Initio Study". In: *Nano Letters* 9.12 (Nov. 13, 2009), pp. 3996–4000 (cit. on p. 51).

[VW11]   N. Vukmirović and L.-W. Wang. "Density of States and Wave Function Localization in Disordered Conjugated Polymers: A Large Scale Computational Study". In: *The Journal of Physical Chemistry B* 115.8 (Feb. 3, 2011), pp. 1792–1797 (cit. on p. 51).

[Wei+06]   D. S. Weiss, M. Abkowitz, S. Kasap, and P. Capper. *Handbook of Electronic and Photonic Materials*. Springer, 2006. Chap. 9 (cit. on pp. 39, 40, 51).

Part III.

Numerical methods

7. Introduction

In this part we aim to solve the mathematical models presented in chapter 6. In particular we consider

- the transient DD system (6.5), which is a non-linear system of an elliptic equation coupled with a parabolic one;

- the equilibrium Non-Linear Poisson equation (6.7), which is an elliptic PDE;

- the time-harmonic system (6.9), consisting of a linear system of an elliptic equation and a parabolic one.

All the previous equations are coupled with a set of algebraic constraints. The key ingredients that form a numerical scheme for the solution of such systems are

- the time semi-discretization;

- the linearization of non-linear problems;

- the discretization scheme.

Section 7.1 will be devoted to present an implicit time-advancing scheme used for the semi-discretization of the time derivatives appearing in the above mentioned models. The scheme is derived for general Ordinary Differential Equations (ODEs) and makes use of an adaptive time step and a linear extrapolation for the non-linear initial guess at each time step. The application of such algorithm to systems of ODEs is proved to keep the global truncation error below a prescribed tolerance; however, there's empirical proof of its effectiveness also in those cases, like the ones we are dealing with, where the differential equations are coupled with algebraic constraints.

Standard linearization methods can be categorized as *staggered*, *i.e.* those decoupling the equations, or *monolithic*, where the system is solved fully coupled, often by means of a Newton method. In this work we focus on the latter class: unlike staggered methods, monolithic ones can be developed and implemented in a problem-independent fashion and are proved to provide fast convergence to the solution. However, the convergence is usually only local and such schemes don't guarantee in general that box-type constraints

are satisfied. A survey of variants to the standard Newton method is presented in chapter 8. Such variants are developed with the aim either to extend the convergence region or to enforce box-type constraints on specific state variables. The actual algorithm employed in our code is a semi-empirical combination of many ingredients presented in chapter 8 and can be described as a projected modified quasi-Newton method with line-search globalization.

Finally, a thermodynamic consistent modification of the Scharfetter-Gummel discretization scheme will be presented in chapter 9 in a one-dimensional framework and then extended to two- (three-)dimensional geometries of quad- (oct-)trees in chapter 10. A recovery metric-based mesh adaptation algorithm will be derived to improve the overall accuracy of the solution strategy adopted.

7.1. Time semi-discretization and time step selection

In this section we present the adaptive scheme used for the time discretization of the problems described in part II. Consider a general ordinary differential equation over the a time interval $[t_0, T]$ written in the following form:

$$\begin{cases} u' = f(t, u), \\ u(t_0) = u_0. \end{cases} \tag{7.1}$$

The well-known and widely adopted backward Euler method consists of approximating the solution u of (7.1) with a sequence $\{u_n\}_n$ such that:

$$u_{n+1} = u_n + \Delta_n t \cdot f(t_{n+1}, u_{n+1}),$$

with $u_n = u(t_n)$ and $\Delta_n t = t_{n+1} - t_n$.

This scheme is implicit and absolutely stable [But16]. However, its order of convergence is 1, which means that, assuming a constant time step Δt, the L^∞-norm of the error between the real and the numerical solution is

$$\|u - u_{ex}\|_\infty \lesssim C\Delta t, \tag{7.2}$$

for a proper constant C.

Therefore a small time step has to be adopted in order to get a high accuracy, that can result in an unfeasible computational cost when trying nonlinear problems. This motivates the derivation of a time adaptation strategy, that makes use of a local extrapolation method to estimate the error at each time step in order to compute the maximum $\Delta_n t$ allowed to guarantee the prescribed accuracy. The proposed method is again of order 1, but with a smaller convergence constant C.

7.1.1. Truncation error

Given an arbitrary approximation $\hat{u}_{n+1}$ of u at t_{n+1}, the local truncation error τ_{n+1} is defined as the difference between the exact and the numerical solution at the current step, namely $\tau_{n+1} = \hat{u}_{n+1} - u_{n+1}$.

We now prove that the difference between two suitable approximations u^0_{n+1} and u_{n+1} of $u(t_{n+1})$ at each time step is a good estimate of the local truncation error.

Let now

$$u^0_{n+1} = \hat{u}_n + \Delta_n t \ \hat{u}'_n \tag{7.3}$$

and

$$u_{n+1} = \hat{u}_n + \Delta_n t \cdot f(t_{n+1}, \hat{u}_{n+1}).$$

A Taylor expansion around t_{n+1} provides

$$\hat{u}_{n+1} = \hat{u}(t_{n+1}) = \hat{u}(t_n + \Delta_n t) \approx \hat{u}_n + \Delta_n t \hat{u}'_n + C \left(\Delta_n t\right)^2.$$

Then the difference between the two approximations yields

$$\begin{aligned} u^0_{n+1} - u_{n+1} &= \hat{u}_n + \Delta_n t \ \hat{u}'_n - u_{n+1} \\ &= \hat{u}_{n+1} - C \left(\Delta_n t\right)^2 - u_{n+1} \\ &= \tau_{n+1} - C \left(\Delta_n t\right)^2, \end{aligned}$$

which is an estimate of the local truncation error of $\hat{u}$ as desired.

7.1.2. Time adaptation

Ideally, the approximation $\hat{u}_{n+1}$ used to derive the error estimate would be chosen to be consistent with eq. (7.1). Since in most cases the exact solution is not available, one way to set $\hat{u}_{n+1}$ is to assume that it comes from one step of the forward Euler method:

$$\hat{u}_{n+1} = \frac{u_n - u_{n-1}}{\Delta_{n-1} t},$$

so that eq. (7.3) becomes the following extrapolation of the last two numerical approximations:

$$u^0_{n+1} = u_n + \Delta_n t \ \frac{u_n - u_{n-1}}{\Delta_{n-1} t}.$$

With this choice, the difference between $u^0_{n+1} - u_{n+1}$ is not of same order as τ_{n+1} anymore. However, it can still be used to drive the time adaptation procedure listed in algorithm 1.

Let tol be a user-specified tolerance and let λ_{min}, λ_{max} two user-defined
  parameters;
Set $t = t_0$, $\Delta t \in \mathbb{R}^+$, $n = 0$;
while $t < T$ **do**
    if $t + \Delta t > T$ **then**
        $\Delta t = T - t$;
    end
    $t = t + \Delta t$;
    if $n == 0$ **then**
        $u_{n+1}^0 = u_0$;
    else
        $u_{n+1}^0 = u_n + \Delta_n t \frac{u_n - u_{n-1}}{\Delta_{n-1} t}$;
    end
    Solve $u_{n+1} = u_n + \Delta t\, f(t_{n+1}, u_{n+1})$.;
    Compute err $= ||u_{n+1}^0 - u_{n+1}||$;
    if *err < tol* **then**
        $n = n + 1$;
        $\Delta_{n-1} t = \Delta_n t$;
        $\Delta_n t = \Delta_{n-1} t \cdot \min\left\{\lambda_{max}, \max\left\{\lambda_{min}, \lambda \cdot \sqrt{\frac{tol}{err}}\right\}\right\}$;
    else
        $t = t - \Delta_n t$;
        $\Delta_n t = \frac{\Delta_n t}{2}$;
    end
end

Algorithm 1: Time adaptation procedure.

We remark that the time step Δt is automatically computed at each step based on the information provided by the ratio $\frac{tol}{err}$, that is an indicator of how large large (small) the error is compared to the user-specified tolerance tol. The smaller the error, the bigger is the predicted maximum time step length allowed. Control parameters as $\lambda, \lambda_{min}, \lambda_{min}$ are used to slow down or fasten variations in the time step length. Following the description in [HNW87], we set $\lambda = \sqrt{0.38}$.

For ODEs the above procedure may be shown to keep the global truncation error within the prescribed tolerance, as shown in the next example. Consider the problem

$$u'(t) = 10\cos(t) - 3u(t), \tag{7.4}$$

having exact solution $u_{ex}(t) = \sin(t) + 3\cos(t)$.

Algorithm 1 was run with different values of tol. The L^{∞}-error obtained and the values of tol with respect to N are displayed in fig. 7.1, which shows order 1 for the error and order 2 for tol as expected.

The advantage of using the adaptive time step compared to the classical backward Euler method, as mentioned above, consists of having a smaller constant C in eq. (7.2). The comparison of the two methods is summarized in fig. 7.2: in order to get a comparable error the time adaptation procedure requires about 18% fewer iterations than backward Euler's scheme.
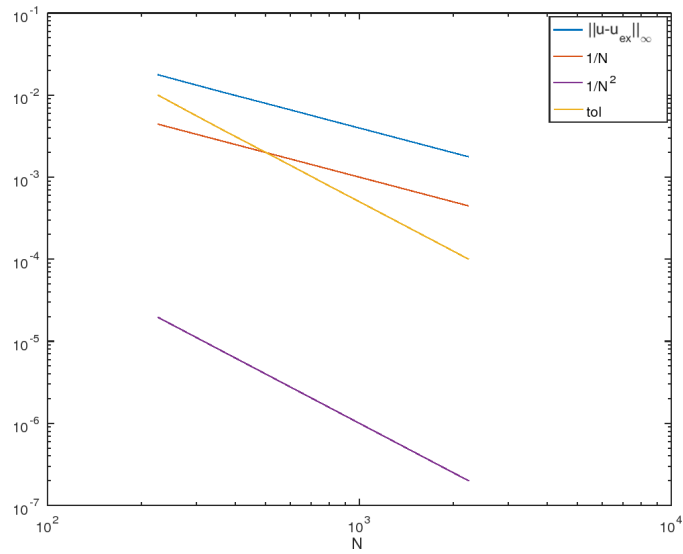
Figure 7.1.: Convergence orders of the time adaptation procedure.
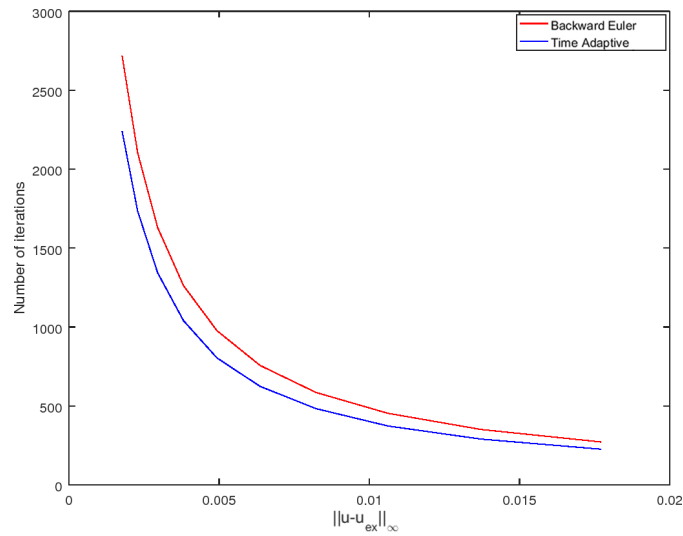
Figure 7.2.: Number of iterations for the backward Euler and the time adaptation scheme.

8. Linearization

The purpose of the present chapter is to address the main aspects of theory of Newton's method and its variants used to linearize nonlinear problems.

The standard Newton method for nonlinear problems will be presented, focusing on the relevance of choosing a proper the initial guess to satisfy the local convergence property. Then the description will be extended to some of the most common *quasi-Newton methods*, a class of schemes where the Jacobian is approximated, and to *inexact Newton* ones where the linear step is solved inexactly, for examples Newton-Krylov methods based on the Generalized Minimal Residual (GMRES). Finally we will present some globalization techniques, with a focus on the line search approach. Further discussions on the methods described below can be found in [Deu11; Căt05].

8.1. Newton's method

Consider a general nonlinear problem

$$F(x) = 0, \quad x \in \mathbb{R}^n,$$

where $F : \mathbb{R}^n \to \mathbb{R}^n$ is continuously differentiable.

Newton's method is an iterative method consisting of computing the sequence $\{x_k\}_k$ such that

$$x_{k+1} = x_k - F'(x_k)^{-1}F(x_k), \tag{8.1}$$

starting from an initial guess x_0.

In the following we will refer to the set of assumptions and definitions, supposed to hold in all of the theorems presented below, namely:

- $F(x) = 0$ has a unique solution x^*;

- $F'(x) : \Omega \to \mathbb{R}^n$ is Lipschitz continuous;

- $F'(x^*)$ is non singular.

Let $x^* \in \mathbb{R}^n$. Then a sequence $\{x_k\}_k \subset \mathbb{R}^n$ is said to be

- **q-linearly convergent** if there exists a constant $C \in (0, 1)$ and an integer m such that for all $k \geq m$

$$||x_{k+1} - x^*|| \leq C||x_k - x^*||;$$

- **q-superlinearly convergent** if there exists a sequence $\{C_k\}_k$ convergent to 0 such that

$$||x_{k+1} - x^*|| \leq C_k||x_k - x^*||;$$

- **convergent of** q-**order** p $(p > 1)$ if there exists a constant C and an integer $m > 0$ such that for all $k \geq m$

$$||x_{k+1} - x^*|| \leq C||x_k - x^*||^p.$$

Theorem 8.1 (Local convergence). *There exists a $\delta > 0$ such that, given an initial guess $x_0 : ||x_0 - x^*|| < \delta$, the Newton iterates given by (8.1) converge* q-*quadratically to x^*, that is $||e_{k+1}|| \leq C||e_k||^2$ for some $C > 0$, where $e_k = x_k - x^*$.*

Since the initial guess has to be chosen close enough to the exact solution, then the convergence is only local. A common stopping criterion is based on the relative residual $||F(x_k)||/||F(x_0)||$, that is a good indicator of the error when $F'(x^*)$ is well conditioned:

Theorem 8.2. *There exists a $\delta > 0$ such that, given $x_k : ||x_k - x^*|| < \delta$:*

$$\frac{||e_k||}{4 \, ||e_0|| \, k(F'(x^*))} \leq \frac{||F(x_k)||}{||F(x_0)||} \leq \frac{4 \, k(F'(x^*)) \, ||e_k||}{||e_0||},$$

where $k \, (F'(x^*)) = ||F'(x^*)|| \cdot \left\| F'(x^*)^{-1} \right\|$ is the conditioning number of $F'(x^*)$.

Another possible stopping criterion relies on the step length

$$s_{k+1} = x_{k+1} - x_k = -F'(x_k)^{-1}F(x_k),$$

so to accept an iterate x_{k+1} as a good approximation of the solution when $||s_{k+1}||$ is sufficiently small. However, it is often too computationally expensive to evaluate the Jacobian $F'(x)$ at each step or even unneeded, especially when the iterate is still inaccurate and far from the exact solution. This motivates the investigation of variants of the Newton method, subject of the next section.

8.2. Variants of Newton's method

This section concerns with different possible approximations of $(F')^{-1}$. First of all, assume that $F + \epsilon$ and $F' + \Delta$ are used instead of F and F' respectively. Then the following result holds.

Theorem 8.3. *There exist* $K > 0$, $\delta > 0$ *and* $\delta_1 > 0$ *such that, given* $\mathbf{x}_k : \|\mathbf{x}_k - \mathbf{x}^*\| < \delta$ *and* $\|\Delta(\mathbf{x}_k)\| < \delta_1$, *then*

$$\mathbf{x}_{k+1} = \mathbf{x}_k - \left(F'(\mathbf{x}_k) + \Delta(\mathbf{x}_k)\right)^{-1} \left(F(\mathbf{x}_k) + \epsilon(\mathbf{x}_k)\right)$$

is well defined (i.e. $F'(\mathbf{x}_k) + \Delta(\mathbf{x}_k)$ *is non-singular) and satisfies*

$$\|\mathbf{e}_{k+1}\| = K \left(\|\mathbf{e}_k\|^2 + \|\Delta(\mathbf{x}_n)\| \cdot \|\mathbf{e}_k\| + \|\epsilon(\mathbf{x}_k)\|\right).$$

In general, quadratic convergence is lost.

8.2.1. Quasi-Newton methods

In quasi-Newton methods an approximation of $F'(\mathbf{x})^{-1}$ is used instead of the exact value [DM77]. This enables to save computational costs at the price of a slower convergence. Moreover, this can be the only viable solution when the exact Jacobian is unavailable or too expensive to be computed at each iteration. A class of quasi-Newton methods is described in the following subsections.

8.2.1.1. Chord method or Modified Newton method

The modified Newton iteration is given by

$$\mathbf{x}_{k+1} = \mathbf{x}_k - F'(\mathbf{x}_0)^{-1} F(\mathbf{x}_k).$$

The convergence of the chord iteration is q-linear. Indeed, this comes from theorem 8.3, remarking that $\epsilon(\mathbf{x}_k) = 0$ and $\|\Delta(\mathbf{x}_k)\| = O(\|\mathbf{e}_0\|)$. The Jacobian could also be evaluated at any of the previous iterations and not necessarily at $\mathbf{x}_0$.

8.2.1.2. Shamanskii method

It consists of alternating of a Newton step with a sequence of chord steps and leads to a class of *high-order methods*, *i.e.* methods that converge q-superlinearly with q-order

larger that 2. The transition from x_k to x_{k+1} is provided by

$$y_1 = x_k - F'(x_k)^{-1}F(x_k),$$
$$y_{j+1} = y_j - F'(x_k)^{-1}F(y_j), \quad \text{for } 1 \le j \le m-1,$$
$$x_{k+1} = y_m.$$

The cases $m = 1$ and $m = \infty$ degenerate in the classical and the modified Newton method, respectively.

Theorem 8.4. *There exist $K_S > 0$ and $\delta > 0$ such that, given an initial guess $x_0 : \|x_0 - x^*\| < \delta$, the Shamanskii iterates converge q-superlinearly to x^* with q-order $m+1$ and*

$$\|e_{k+1}\| \le K_S \|e_k\|^{m+1},$$

for a proper constant K_S.

The advantage of such a method is that high convergence orders can be reached with few Jacobian evaluations.

8.2.1.3. Difference approximations

Another possibility consists of replacing $F'(x_k)$ with an approximation through *n*-dimensional differences of the form

$$\left(F_h'^{(k)} \right)_j = \frac{F\left(x_k + h_j^{(k)} e_j \right) - F(x_k)}{h_j^{(k)}}, \quad \forall k \ge 0,$$

where e_j is the j-th vector of the canonical basis of $\mathbb{R}^n$ and $h_j^{(k)} > 0$ are increments to be suitably chosen at each k-th iteration.

Under the standard assumptions and given an initial guess close enough to x^* then the sequence

$$x_{k+1} = x_k - \left(F_h'^{(k)} \right)^{-1} F(x_k) \tag{8.2}$$

can be proved to converge linearly to x^*. Moreover, if there exists a positive constant C such that $\max_j \left| h_j^{(k)} \right| \le C \|x_k - x^*\|$ or, equivalently, if there exists a positive constant c such that $\max_j \left| h_j^{(k)} \right| \le c \|F(x_k)\|$, then the sequence (8.2) convergences quadratically. We remark that choosing small $h_j^{(k)}$ can lead to large truncation errors.

8.2.1.4. Broyden's method

This is a generalization of the scalar secant method to vector problems. The method demands that the current approximation B_k of $F'(x_k)$ satisfies the secant equation

$$B_k(x_k - x_{k-1}) = F(x_k) - F(x_{k-1}).$$

A wide variety of methods satisfying this relation have been designed to preserve properties such as the sparsity or the symmetry of the Jacobian. The standard Broyden method reads

$$x_{k+1} = x_k - \lambda_k B_k^{-1} F(x_k),$$
$$y_k = F(x_{k+1}) - F(x_k),$$
$$s_k = x_{k+1} - x_k = \lambda_k d_k,$$
$$B_{k+1} = B_k + \frac{(y_k - B_k s_k) s_k{}^T}{s_k{}^T s_k},$$

where λ_k is a non-constant step length.

In this case there is no guarantee that the approximate direction $-\lambda_k B_k^{-1} F(x_k)$ is a descent direction for $||F||$. Assuming x_0 and B_0 are good approximations of x^* and $F'(x^*)$, the convergence is q-superlinear [DM74]. So it is only local and, therefore, less satisfactory than the one of other variants presented in this chapter.

For memory occupation reasons, it is often more advantageous to approximate the Jacobian matrix instead of its inverse due to fill-in phenomena. This is typical especially for nonlinear differential problems, where the Jacobian has a known sparsity pattern. A variant of Broyden's method applicable to this scenario is stated in [Sch70].

8.2.2. Inexact Newton method

Rather than approximating the Jacobian, one could solve the equation for the Newton step approximately. An inexact Newton method uses as a step a vector s that satisfies the inexact Newton condition

$$||F'(x_k)s + F(x_k)|| \leq \eta_k ||F(x_k)||. \tag{8.3}$$

The parameter η_k is called forcing term. At the very first Newton iterations, when the numerical solution is still possibly inaccurate, choosing η too small may lead to *oversolving* the Newton equation. Therefore far from the solution, a less accurate approximation of the Newton step may be both cheaper and more effective. So, the idea is to choose a forcing term that becomes smaller when the iterations approach to the solution. The following convergence result holds [EW94].

Theorem 8.5. *There exist δ and $\bar{\eta}$ such that, given an initial guess $\mathbf{x}_0 : \|\mathbf{x}_0 - \mathbf{x}^*\| < \delta$, $\eta_k \in [0, \bar{\eta}]$, then the inexact Newton iterations*

$$\mathbf{x}_{k+1} = \mathbf{x}_k + \mathbf{s}_k$$

where

$$\|F'(\mathbf{x}_k)\mathbf{s}_k + F(\mathbf{x}_k)\| \leq \eta_k \|F(\mathbf{x}_k)\|,$$

converge q-*linearly to $\mathbf{x}^*$. Moreover,*

- *if $\eta_k \to 0$, the convergence is* q-*superlinear, and*

- *if $\eta_k \leq K_\eta \|F(\mathbf{x}_k)\|^p$ for some $K_\eta > 0$, the convergence is* q-*superlinear with* q-*order $p + 1$.*

The following possible choices for η are presented in [EW96].

Choice 1 Given $\eta_0 \in [0, 1)$, choose

$$\eta_k = \frac{\|F(\mathbf{x}_k) - F(\mathbf{x}_{k-1}) - F'(\mathbf{x}_{k-1})\mathbf{s}_{k-1}\|}{\|F(\mathbf{x}_{k-1})\|}, \tag{8.4}$$

or

$$\eta_k = \frac{\|\|F(\mathbf{x}_k)\| - \|F(\mathbf{x}_{k-1}) + F'(\mathbf{x}_{k-1})\mathbf{s}_{k-1}\|\|}{\|F(\mathbf{x}_{k-1})\|\|}, \tag{8.5}$$

Note that η_k given by (8.4) and (8.5) directly reflects the match between F and its local linear approximation at the previous step. The choice (8.5) may be more convenient to evaluate than (8.4) in some circumstances. Since it is at least as small as (8.4), local convergence will be at least as fast as with (8.4). One possible way to obtain faster local convergence, while retaining the potential advantages of (8.4) and (8.5), is to raise those expression to powers with exponent greater than one.

Choice 2 Given $\gamma \in [0, 1]$, $\alpha \in (1, 2]$, and $\eta_0 \in [0, 1)$, choose

$$\eta_k = \gamma \left(\frac{\|F(\mathbf{x}_k)\|}{\|F(\mathbf{x}_{k-1})\|} \right)^\alpha, \tag{8.6}$$

This choice does not directly reflect the agreement between F and its local approximated linear model. In practice, however, it can produce a little oversolving.

Experiments have shown that the forcing term may occasionally become too small even far from the solution, especially the one computed as in eqs. (8.4) and (8.5). For this reason it is convenient to include *safeguards* that are intended to prevent the forcing term to become too small too soon [Kel03], for example

Choice 1 safeguard Replace η_k by $\eta_k = \max\left\{\eta_k, \eta_{k-1}^{\frac{1+\sqrt{5}}{2}}\right\}$ whenever $\eta_{k-1}^{\frac{1+\sqrt{5}}{2}} > 0.1$.

Choice 2 safeguard Replace η_k by $\eta_k = \max\left\{\eta_k, \gamma\eta_{k-1}^{\alpha}\right\}$ whenever $\gamma\eta_{k-1}^{\alpha} > 0.1$.

Iterative methods for solving the equation for the Newton step would typically use eq. (8.3) as a stopping criterion. In this case, the overall nonlinear solver is named after the particular iterative method used for the linear equation, such as Newton-Jacobi, Newton-SOR or Newton-Krylov. In the following we will refer to this last class of methods.

8.2.2.1. Newton-Krylov methods

As said before, for each iteration of the inexact Newton method the resulting linear equation has to be solved by means of an iterative method. Sometimes we refer to this linear iteration as to an *inner iteration*. Similarly, the nonlinear step is often called the *outer iteration*. Newton-Krylov methods, as the name suggests, rely on Krylov subspace-based linear solvers [Kel03; BS90]. The solution $\mathbf{d}$ of a linear system $A\mathbf{d} = \mathbf{b}$ is approximated with a sum of the form

$$\mathbf{d}_k = \mathbf{d}_0 + \sum_{j=0}^{k-1} \gamma_j A^j \mathbf{r}_0,$$

where $\mathbf{r}_0 = \mathbf{b} - A\mathbf{d}_0$ and $\mathbf{d}_0$ is the initial iterate. Since the goal is to approximate a Newton step, a reasonable choice is to set $\mathbf{d}_0 = \mathbf{0}$ since there is no knowledge on prior directions, which is however expected to be small. We express this in compact form as $\mathbf{d}_k \in \mathcal{K}_k$, where the k-th Krylov subspace is $\mathcal{K}_k = \text{span}\left\{\mathbf{r}_0, A\mathbf{r}_0, \ldots, A^{k-1}\mathbf{r}_0\right\}$.

Many Newton-Krylov methods are available that differ in storage requirements, costs of evaluating F and robustness. If A is symmetric and positive definite, the Conjugate Gradient (CG) method has better storage and convergence properties than other Newton-Krylov methods. Otherwise, two low-storage solvers, namely the Bi-Conjugate Gradient STABilized (BiCGSTAB) and the Transpose-Free Quasi-Minimal Residual (TFQMR) methods, can be used, but with the awareness of possible failure in case a division by zero occurs.

Another option is the GMRES, that is not strictly a low-storage solver but guarantees that, in case of non-convergence, stagnation occurs instead of a break down. The k-th GMRES iterate is the solution of the linear least squares problem of minimizing

$$||\mathbf{b} - A\mathbf{d}_k||^2$$

over $\mathcal{K}_k$. An important property is that GMRES accumulates the history of the linear iteration as an orthonormal basis for the Krylov subspaces. Therefore, for large problems, it can exhaust the available memory. In such cases, there is GMRES(m), which restarts the iteration when the size of Krylov space exceeds m vectors.

Sometimes the GMRES method, like other Krylov methods, is implemented in a *matrix-free* form in which only matrix-vector products are needed, rather than storing the matrix itself [KK04]. The algorithm description is provided, for example, in [SS86]. As a general rule, GMRES, like others Krylov methods, performs at its best if the eigenvalues of A are grouped in few tight clusters.

8.3. Globalization

Globalization techniques are used to improve the likelihood of convergence from arbitrary initial guesses [BR81; CV17]. Most of such techniques can be classified into **line search** and **trust-region** methods.

8.3.1. Line search

Often Newton's method fails to reach convergence when the iterates are still far from the solution due to a too large or too small step. The step length can be tuned through an additional parameter λ_k such that the new iterate is updated on the search direction $\mathbf{d}_k$ as $\mathbf{x}_{k+1} = \mathbf{x}_k + \lambda_k \mathbf{d}_k$. This technique is often referred to as *damping*.

One way to compute a damping parameter is to search over a set of admissible values until the following condition is satisfied:

$$||F(\mathbf{x}_k + \lambda_k \mathbf{d}_k)|| \leq ||F(\mathbf{x})||.$$

We call this method *line search* because the decrease of $F(\mathbf{x})$ is searched along the line segment

$$(\mathbf{x}_k, \mathbf{x}_k - \mathbf{d}_k).$$

Since the solution moves from the right to the left endpoint, this procedure is usually called *backtracking* and is often used for guaranteeing non-negativity constraints for density variables, so to prevent large steps that would make such variables negative.

Another possibility consists of imposing the stricter Armijo rule

$$||F(\mathbf{x}_k + \lambda_k \mathbf{d}_k)|| \leq (1 - \alpha\lambda_k)||F(\mathbf{x})||.$$

The reduction factor is often chosen as $\alpha = \frac{1}{2}$. There exist different ways of determining λ_k, such as

Constant reduction This consists of choosing a starting $\lambda_0 \in (0, 1)$ and then trying with different values of the form $\lambda = \lambda_0^m$ by letting m vary until the condition is satisfied.

Polynomial line searches Choosing an optimal reduction factor would increase the performance of a constant reduction approach. The goal is to construct a polynomial

$$f(\lambda) = ||F(\mathbf{x}_k + \lambda \mathbf{d}_k)||^2$$

starting from the prior information available about a number of inadmissible values of λ. Then the optimal λ is determined as the minimizer of f.

8.3.2. Trust region

As seen above, the globalization of the convergence in Newton methods is about ensuring that the new iterate reduces the norm of F, even through a constant less than 1, that is $||F(\mathbf{x}_{k+1})|| \leq \alpha||F(\mathbf{x}_k)||$, with $0 < \alpha \leq 1$. This is equivalent to stating that $\mathbf{s}_k = \mathbf{x}_k + \lambda_k \mathbf{d}_k$ is a *descent direction*.

Consider this minimization problem

$$\min_{\mathbf{x} \in \mathbb{R}^N} f(\mathbf{x}) = \frac{1}{2}F(\mathbf{x})^\mathsf{T}F(\mathbf{x}).$$

A descent direction for f at the current approximation $\mathbf{x}$ is any vector $\mathbf{p}$ such that

$$\nabla f(\mathbf{x})^\mathsf{T}\mathbf{p} < 0. \tag{8.7}$$

It is easy to show that, being $\nabla f(\mathbf{x})^\mathsf{T}\mathbf{p} = J(\mathbf{x})^\mathsf{T}F(\mathbf{x})$, with $J(\mathbf{x}) = F'(\mathbf{x})$, (8.7) is equivalent to

$$F(\mathbf{x})^\mathsf{T}J(\mathbf{x})\mathbf{p} < 0. \tag{8.8}$$

For such a direction, there exists a certain $\lambda_0 > 0$ such that $f(\mathbf{x} + \lambda\mathbf{p}) < f(\mathbf{x})$, $\forall\lambda \in (0, \lambda_0]$.

If $J(\mathbf{x}_k)\mathbf{s}_k = -F(\mathbf{x}_k)$ is solved by means of a direct method, so that $\mathbf{s}_k$ is always a descent direction since $\mathbf{p} = -J(\mathbf{x})^{-1}F(\mathbf{x})$ satisfies eq. (8.8), which is not always the case when approximating $\mathbf{s}_k$ through an iterative method.

Let for simplicity $F = F(x)$ and $J = J(x)$, with $\bar{s}$ an approximate solution of $Js = -F$. Then we can write

$$F^T J \bar{s} = -F^T F - F^T \bar{r}$$

with $\bar{r} = -F - J\bar{s}$; $\bar{s}$ is a descent direction for f at x whenever $\left| F^T \bar{r} \right| < F^T F$; in particular the condition

$$||\bar{r}|| < ||F||, \tag{8.9}$$

implies that $\bar{s}$ is a descent direction.

The effect of using a Krylov method to solve the Newton equations $J(x)d = -F(x)$ approximately is to take a step from x of the form $x + s$, where s is in the affine subspace $d_0 + \mathcal{K}_m$. If $V_m = [v_1, \dots, v_m]$ is an orthonormal basis for $\mathcal{K}_m$ and the initial guess $d_0 = 0$, then $d = V_m y$, for some $y \in \mathbb{R}^m$ and the step can be expressed as $x + V_m y$. As introduced above, the globalization strategy relies on finding a local minimum of the real-valued function $\frac{1}{2} F(x)^T F(x)$. Thus, the problem consists of solving

$$\min_{y \in \mathbb{R}^m} f(x + V_m y). \tag{8.10}$$

Letting $g(y) = f(x + V_m y)$, we get

$$\nabla g(y) = (J(x + V_m y)V_m)^T F(x + V_m y)$$

and

$$\nabla g(0) = (JV_m)^T F.$$

Using $F + JV_m y$ as a linear model of $F(x + V_m y)$, implies that the quadratic model for g is represented by

$$\hat{g}(y) = \frac{1}{2} ||F + JV_m y||^2.$$

Letting $B_m = (JV_m)^T JV_m$ yields

$$\hat{g}(y) = \frac{1}{2} F^T F + F^T JV_m y + \frac{1}{2} y^T B_m y \tag{8.11}$$

where B_m is symmetric and positive semidefinite and $\nabla \hat{g}(0) = \nabla g(0)$. If J is non-singular, then V_m has orthonormal columns and B_m is strictly positive definite. The considered *trust region* method [BMM03] relies on solving the problem

$$\min_{||y|| \leq \tau} \hat{g}(y), \quad y \in \mathbb{R}^m, \tag{8.12}$$

where τ is an estimate of the maximum length of a successful step to take from x and measures the size of the region where the local quadratic model $\hat{g}(y)$ closely agrees with the function $g(y)$. The following result, proved in [BS90], provides the solution to eq. (8.12).

Theorem 8.6. *Let $\hat{g}(y)$ be defined by (8.11), and assume that J is non-singular. Then problem (8.12) is solved by*

$$y_m(\mu) = (B_m + \mu I)^{-1} z_m,$$

where $z_m = -\nabla \hat{g}(0)$, for the unique μ such that $||y_m(\mu)|| = \tau$ unless $||y_m(0)|| \leq \tau$, in which case $y_m(0) = B_m^{-1} z_m$ is the solution. Furthermore, $\forall \mu \geq 0$, $s(\mu) = V_m y_m(\mu)$ defines a descent direction for $f(x) = \frac{1}{2} F(x)^T F(x)$ from x, as long as $z_m \neq 0$.

In case $||y_m(0)|| > \tau$, there is no value of μ such that $||y_m(\mu)|| = \tau$, so eq. (8.12) has to be solved approximately. In [Pow70] the authors present a piecewise linear approximation to the parametric curve $y_m(\mu)$ and choose $\hat{y}_m$ as the point lying on this curve such that $||\hat{y}_m|| = \tau$. Letting $x_{k+1} = x_k + \hat{d}$, where $\hat{d} = V_m \hat{y}_m$, if the iterate x_{k+1} satisfies the condition

$$f(x + \bar{d}) \leq f(x) + \alpha \nabla f(x)^T \bar{d},$$

with $0 < \alpha < 1$, then it is accepted; otherwise, a new value of the trust region size τ is chosen, and the procedure is run again.

9. Consistent one-dimensional discretization

We present here a one-dimensional discretization scheme for the DD equations which is consistent with the thermodynamic equilibrium case, as anticipated in section 6.1.1. The results presented hereafter are also discussed in [AFN19].

Accurate and stable numerical solution of the semiconductor equations requires spatial discretization methods that employ upwinding techniques to deal with possibly dominant advective phenomena [Boc11; BP11]. In this work we follow an approach based on a finite volume method, particularly a Scharfetter-Gummel stabilized box method [MW94; BCC98].

Given a spatial discretization grid $\{z_i\}_{i=1}^n$ with n the number of mesh nodes, the box method requires to construct a *dual mesh*, defined by the boxes $[z_{i-\frac{1}{2}}, z_{i+\frac{1}{2}}]$, where $z_{i+\frac{1}{2}}$ is the midpoint of the interval $\Omega_i = [z_i, z_{i+1}]$, as shown in fig. 9.1; let $h_i = z_{i+1} - z_i$ denote the size of a box.

Since the Poisson and the continuity equations presented in chapter 6 both fall into this category, we will focus on a general diffusion-advection-reaction problem:

$$\begin{cases} J' + cu = 0, \\ \qquad J = -au' + bu, \end{cases} \tag{9.1}$$

where a, b, c are the diffusion, advection and reaction coefficients respectively.

Integrating eq. (9.1) over the box $[z_{i-\frac{1}{2}}, z_{i+\frac{1}{2}}]$ yields:

$$J_{i+\frac{1}{2}} - J_{i-\frac{1}{2}} + \int_{z_{i-\frac{1}{2}}}^{z_{i+\frac{1}{2}}} c(z)u(z)\,dz = 0, \tag{9.2}$$
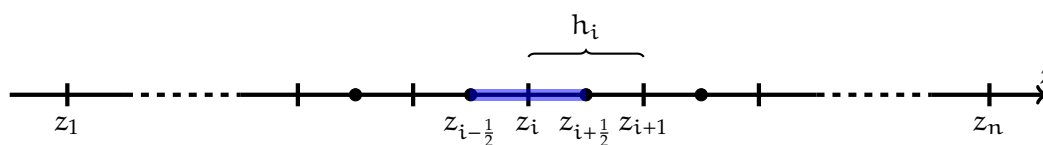
Figure 9.1.: Mesh and dual mesh used for the discretization.

9. Consistent one-dimensional discretization

We now approximate the flux $J(z)$ and the coefficients $a(z), b(z)$ to be constant over each interval $[z_i, z_{i+1}]$ (see [Sha99]), so that:

$$J_{i+\frac{1}{2}} \approx -a_{i+\frac{1}{2}} u' + b_{i+\frac{1}{2}} u,$$

where u is the solution to the following linear ordinary differential equation with constant coefficients:

$$\begin{cases} -a_{i+\frac{1}{2}} u'' + b_{i+\frac{1}{2}} u' = 0, & z \in [z_i, z_{i+1}], \\ u(z_i) = u_i, \\ u(z_{i+1}) = u_{i+1}, \end{cases} \tag{9.3}$$

which gives:

$$u(z) = A + B \exp\left(\lambda_{i+\frac{1}{2}} z\right),$$

with:

$$A = \frac{u_i \exp\left(\lambda_{i+\frac{1}{2}} z_{i+1}\right) - u_{i+1} \exp\left(\lambda_{i+\frac{1}{2}} z_i\right)}{\exp\left(\lambda_{i+\frac{1}{2}} z_{i+1}\right) - \exp\left(\lambda_{i+\frac{1}{2}} z_i\right)} = \frac{u_i \exp\left(\lambda_{i+\frac{1}{2}} h_i\right) - u_{i+1}}{\exp\left(\lambda_{i+\frac{1}{2}} h_i\right) - 1},$$

$$B = \frac{u_{i+1} - u_i}{\exp\left(\lambda_{i+\frac{1}{2}} z_{i+1}\right) - \exp\left(\lambda_{i+\frac{1}{2}} z_i\right)},$$

$$\lambda_{i+\frac{1}{2}} = \frac{b_{i+\frac{1}{2}}}{a_{i+\frac{1}{2}}}.$$

The quantity $\lambda_{i+\frac{1}{2}} h$ represents the local Péclet number multiplied by 2. Finally we compute the approximate flux $J_{i+\frac{1}{2}}$:

$$J_{i+\frac{1}{2}} = -a_{i+\frac{1}{2}} u' + b_{i+\frac{1}{2}} u = A b_{i+\frac{1}{2}} =$$

$$= b_{i+\frac{1}{2}} \frac{u_i \exp\left(\lambda_{i+\frac{1}{2}} h_i\right) - u_{i+1}}{\exp\left(\lambda_{i+\frac{1}{2}} h_i\right) - 1} =$$

$$= \frac{a_{i+\frac{1}{2}}}{h} \lambda_{i+\frac{1}{2}} h \frac{u_i \exp\left(\lambda_{i+\frac{1}{2}} h_i\right) - u_{i+1}}{\exp\left(\lambda_{i+\frac{1}{2}} h_i\right) - 1},$$

which can be rewritten as

$$J_{i+\frac{1}{2}} = -\frac{a_{i+\frac{1}{2}}}{h_i} \left[u_{i+1} \mathcal{B}(\lambda_{i+\frac{1}{2}} h_i) - u_i \mathcal{B}(-\lambda_{i+\frac{1}{2}} h_i) \right], \tag{9.4}$$

where we denoted by $\mathcal{B}(q) = \frac{q}{\exp(q)-1}$ the Bernoulli function and exploited its property $\mathcal{B}(-q) = e^q \mathcal{B}(q)$. The expression of $J_{i-\frac{1}{2}}$ can be analogously derived by interchanging $[z_i, z_{i+1}]$ with $[z_{i-1}, z_i]$:

$$J_{i-\frac{1}{2}} = -\frac{a_{i-\frac{1}{2}}}{h_i} \left[u_i \mathcal{B}(\lambda_{i-\frac{1}{2}} h_i) - u_{i-1} \mathcal{B}(-\lambda_{i-\frac{1}{2}} h_i) \right].$$

The expression (9.4) corresponds to the difference formula presented by Scharfetter and Gummel in [SG69]. An interesting property of this scheme is that it automatically adapts itself to all possible transport regimes: for example, if we assume $b(z) = 0$, *i.e.* no advection ($\lambda = 0$), the formula reduces to

$$J_{i+\frac{1}{2}} = -a_{i+\frac{1}{2}} \frac{u_{i+1} - u_i}{h_i},$$

which is a difference approximation of a purely diffusive flow. Conversely, if we assume $b(z) \to +\infty$, *i.e.* advective phenomena are dominant ($\lambda \to +\infty$), the formula degenerates in:

$$J_{i+\frac{1}{2}} = -\frac{a_{i+\frac{1}{2}}}{h_i} \left[-u_i \cdot (\lambda_{i+\frac{1}{2}} h_i) \right] = b_{i+\frac{1}{2}} u_i,$$

while, for $b(z) \to -\infty$:

$$J_{i+\frac{1}{2}} = -\frac{a_{i+\frac{1}{2}}}{h_i} \left[u_{i+1} \cdot (-\lambda_{i+\frac{1}{2}} h_i) \right] = b_{i+\frac{1}{2}} u_{i+1};$$

these two expressions correspond to an upwind discretization of a purely advective flow.

Finally, the reaction term is approximated using the midpoint quadrature rule:

$$\int_{z_{i-\frac{1}{2}}}^{z_{i+\frac{1}{2}}} c(z) u(z) \, dz \approx \frac{h_i + h_{i+1}}{2} c_i u_i. \tag{9.5}$$

Expanding eq. (9.2) over all the boxes $[z_{i-\frac{1}{2}}, z_{i+\frac{1}{2}}]$ through the approximations (9.4) and (9.5) finally leads to a linear system for the nodal unknowns $\{u_i\}_{i=1}^n$.

95

Theorem 9.1 (Thermodynamical consistence). *The discrete formulation provided by the Scharfetter-Gummel scheme (9.4) applied to the one-dimensional flux defined as in eq. (6.4) is such that*

$$\varphi_n = 0 \implies J_n = 0$$

at the discrete level.

Proof. The Scharfetter-Gummel discretization (9.4) applied to the continuity equation provides the following numerical flux on a generic mesh interval Ω_i:

$$-\frac{J_n|_{\Omega_i}}{q} = \frac{\mu_n|_{\Omega_i} V_{th}}{|\Omega_i|} \left[\mathcal{B}\left(\Delta_i\left(\frac{\varphi+\psi}{V_{th}}\right)\right) n_{i+1} - \mathcal{B}\left(-\Delta_i\left(\frac{\varphi+\psi}{V_{th}}\right)\right) n_i \right], \tag{9.6}$$

where

$$\Delta_i(f) = f_{i+1} - f_i = f(x_{i+1}) - f(x_i).$$

Assume now that the density n is given by the consistency relation (6.3) evaluated at the thermodynamical equilibrium – *i.e.* $\varphi_n = 0$:

$$n_i = N_0 \exp\left(\frac{\varphi_i + \psi_i}{V_{th}}\right).$$

Then, replacing this expression into eq. (9.6), expanding and letting for the sake of simplicity $\tilde{\varphi} = \varphi + \psi$ yields

$$J_n|_{\Omega_i} \propto \frac{\tilde{\varphi}_{i+1} - \tilde{\varphi}_i}{\exp\left(\frac{\tilde{\varphi}_{i+1}-\tilde{\varphi}_i}{V_{th}}\right) - 1} \exp\left(\frac{\tilde{\varphi}_{i+1}}{V_{th}}\right) +$$

$$+ \frac{\tilde{\varphi}_{i+1} - \tilde{\varphi}_i}{\exp\left(-\frac{\tilde{\varphi}_{i+1}-\tilde{\varphi}_i}{V_{th}}\right) - 1} \exp\left(\frac{\tilde{\varphi}_i}{V_{th}}\right) =$$

$$= (\tilde{\varphi}_{i+1} - \tilde{\varphi}_i) \left[\frac{\exp\left(\frac{\tilde{\varphi}_{i+1}}{V_{th}}\right)}{\exp\left(\frac{\tilde{\varphi}_{i+1}-\tilde{\varphi}_i}{V_{th}}\right) - 1} + \frac{\exp\left(\frac{\tilde{\varphi}_i}{V_{th}}\right)}{\exp\left(-\frac{\tilde{\varphi}_{i+1}-\tilde{\varphi}_i}{V_{th}}\right) - 1} \right] =$$

$$= (\tilde{\varphi}_{i+1} - \tilde{\varphi}_i) \left[\frac{\exp\left(\frac{\tilde{\varphi}_{i+1}}{V_{th}}\right)}{\exp\left(\frac{\tilde{\varphi}_{i+1}-\tilde{\varphi}_i}{V_{th}}\right) - 1} - \frac{\exp\left(\frac{\tilde{\varphi}_i}{V_{th}}\right)\exp\left(\frac{\tilde{\varphi}_{i+1}-\tilde{\varphi}_i}{V_{th}}\right)}{\exp\left(\frac{\tilde{\varphi}_{i+1}-\tilde{\varphi}_i}{V_{th}}\right) - 1} \right] =$$

$$= 0.$$

<div align="right">□</div>

10. Two- and three-dimensional discretization

In this chapter we present a discretization scheme for two- and three-dimensional geometries. Our approach relies on the use of Cartesian quadtree/octree meshes, for reasons that will be motivated and discussed in section 10.1. We allow for the mesh to have non-conforming edges: the corresponding finite element formulation will be discussed in section 10.2. The recovery-based estimator will be derived in section 10.3, and a corresponding metric-based algorithm for mesh adaptation is also proposed in section 10.4. Finally, the implementation strategies followed in the development of an efficient, scalable numerical code will be examined in section 10.5. The results presented hereafter are also discussed in [AFP19].

10.1. Introduction

The term *octree* denotes a recursive tree structure where each node is either a leaf or has eight children. Its two-dimensional equivalent is named *quadtree*, where nodes have four children instead of eight [BWG11]. Octrees and quadtrees can be associated with 3D and 2D cubic domains, where tree nodes are called octants and quadrants, respectively, and the root node corresponds to a cubic domain that is recursively subdivided according to the tree structure. We use the term *forest* to describe a collection of such logical cubes that are connected conformingly through faces, edges, or corners, each cube corresponding to an independent tree. In the following we will only refer to forests of quadtrees, as the discussion can be easily extended to three-dimensional geometrical domains.

Quadrants within a quadtree can be assigned a natural ordering by a traversal across all leaves. By the equivalence of tree nodes and quadrants this one-dimensional sequence corresponds to a space-filling s-shaped curve in the geometric domain. A parallel partition is created by dividing the curve into P segments with P being the number of parallel processes. These concepts, whose graphical representation is shown in fig. 10.1, can be extended to forests of quadtrees by connecting the space-filling curve between quadtrees, thus generating a total ordering of all quadrants in the domain [BWG11].

(a) Geometrical mesh. (b) Corresponding tree data structure.
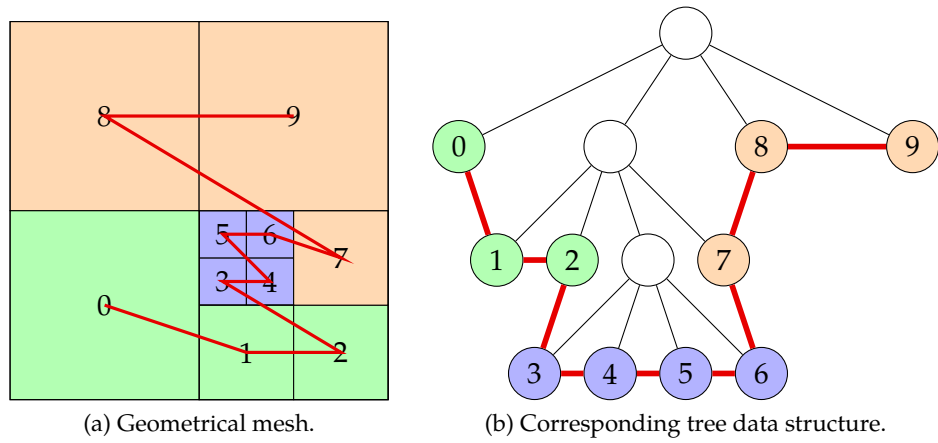
Figure 10.1.: Geometrical mesh and its corresponding tree data structure. The red line is the space-filling curve used to determine a unique global ordering of all the quadrants in the domain. Different quadrant colors correspond to different parallel processes.

The following definitions will clarify the numerical procedure discussed in the present chapter.

Connectivity creation Create an equi-partitioned, uniformly and conformingly refined forest.

Refinement Adaptively subdivide quadrants based on a refinement marker, once or recursively. This means replacing, at each refinement step, a quadrant with four children of equal size.

Coarsening Replace families of four child quadrants by their common parent quadrant based on a coarsening marker, once or recursively.

Partitioning Redistribute the quadrants in parallel, according to a given target number of quadrants per process or according to prescribed quadrant weights.

Balancing Ensure at most 2:1 size relations between neighboring quadrants by local refinement where necessary. The process is illustrated in fig. 10.2.

Below we will only refer to balanced quadtrees, as required for the numerical application described below and needed in order to ensure a balanced computational load among different parallel units.

Figure 10.2.: Process of 2:1 quadtree balancing.

Following [BWG11], a quadrant is also said to be a

ghost to a local process if it is owned by another process but touches from the outside the boundaries of current process;

mirror if it is a ghost to another process.

Once the quadrants have been assigned a rank-local and global index and have been partitioned, another space-filling s-shaped curve connecting the mesh node is created, in order to number and parallel distribute vertices, too. Each independent node is assigned to one owner process by dividing such space-filling curve; then the nodes are numbered globally in sequence of their owner processes. The numbering of a node is canonicalized, *i.e.* when shared between multiple quadtrees it is assigned to the lowest-numbered quadtree touching it. A node is marked as

owned by a process if it is assigned to it;

local if it is owned by a ghost quadrant and touches the boundary of current process;

non-local otherwise.

The owned nodes are also locally numbered with indices that are contiguous on the local processor.

10.2. Discrete formulation on quadtree/octree meshes

Let $\Omega \subset \mathbb{R}^2$ an open, bounded domain. We will henceforth assume Ω to be a Cartesian rectangle, but the method described below can be trivially extended to any simply

connected union of rectangles.

In the following we will refer to two classes of differential problems, namely reaction-diffusion equations of the form:

$$\begin{cases} -\nabla \cdot (\varepsilon \nabla u) + bu = f, & \text{in } \Omega, \\ \qquad\qquad\quad u = g, & \text{on } \Gamma_D \subseteq \partial\Omega, \\ \qquad\quad \nabla u \cdot \mathbf{v} = 0, & \text{on } \partial\Omega \setminus \Gamma_D, \end{cases} \tag{10.1}$$

and advection-diffusion problems:

$$\begin{cases} -\nabla \cdot (\varepsilon(\nabla u - \boldsymbol{\beta} u)) = f, & \text{in } \Omega, \\ \qquad\qquad\qquad u = g, & \text{on } \Gamma_D \subseteq \partial\Omega, \\ \qquad\qquad \nabla u \cdot \mathbf{v} = 0, & \text{on } \partial\Omega \setminus \Gamma_D, \end{cases} \tag{10.2}$$

with $\boldsymbol{\beta}$ such that $\boldsymbol{\beta} = \nabla \psi$ and $\nabla \cdot \boldsymbol{\beta} = 0$ for a proper potential ψ. We allow for the coefficients ε, b, $\boldsymbol{\beta}$ and f to be discontinuous in Ω.

In the following sections we will present the numerical scheme adopted to discretize such equations: first we will introduce the case of Cartesian-product meshes, *i.e.* quadrilateral grids whose vertices are the Cartesian product of one-dimensional partitions of one-dimensional intervals, and then we generalize the discretization to non-conforming quadtree meshes generated by refinement or coarsening procedures.

10.2.1. Discretization on Cartesian-product meshes

Let $\tau_h = \left\{ \Omega^{(k)} \right\}_{k=1}^{N_{el}}$ be a family of Cartesian partitions of Ω, where N_{el} is the total number of mesh elements, and let $\Omega_h = \cup_{k=1}^{N_{el}} \Omega^{(k)} \subseteq \Omega$.

We adopt the finite element space consisting of continuous piecewise bi-linear polynomials $Q_h^1(\tau_h)$, where

$$Q_h^n(\tau_h) = Q_h^{n,n}(\tau_h),$$
$$Q_h^{n,m}(\tau_h) = \{ v \in C^0\left(\overline{\Omega_h} \right) : v|_{\Omega^{(k)}} \in \mathbb{P}_{n,m}\left(\Omega^{(k)} \right) \ \forall \Omega^{(k)} \in \tau_h \},$$

and

$$\mathbb{P}_{m,n}(A) = \{ p : A \to \mathbb{R} : p(x,y) = \sum_{\substack{i \leq m \\ j \leq n}} a_{ij} x^i y^j, \ \forall (x,y) \in A \}.$$

In the following, for the sake of simplicity, we will omit the dependence of these spaces on the partition τ_h. Let now $u_h \in Q_h^1$ be the Galërkin approximation of the solution

u of problem (10.1) or (10.2) and let $X = \{x_i\}_{i=1}^N$ be the set of the vertices defining the partition τ_h. Then the functions $\{\varphi_i\}_{i=1}^N \subset Q_h^1$ such that

$$\varphi_i(x_j) = \delta_{ij}, \quad \forall x_j \in X, \tag{10.3}$$

where δ_{ij} is the Kronecker delta, form a basis for Q_h^1:

$$Q_h^1 = \mathrm{span}\left(\{\varphi_i\}_{i=1}^N\right).$$

Therefore the discrete solution $u_h \in Q_h^1$ can be expressed as a linear combination of these basis functions through a set of coefficients $\{U_i\}_{i=1}^N$ which represent the actual unknowns:

$$u_h(x) = \sum_{i=1}^N U_i \varphi_i(x), \ \forall x \in \Omega_h.$$

The numerical scheme adopted to discretize the class of problems under analysis relies on the Finite-Volume Scharfetter-Gummel (FVSG) method proposed in [BCC98]. This method was originally introduced by D. N. de G. Allen and R. V. Southwell in [GS55] for one-dimensional geometries and then generalized to a two- and three-dimensional setting by M. A. Zlámal in [Zlá86] for diffusion-convection equations and to self-adjoint problems by P. A. Markowich and M. A. Zlámal in [MZ88].

The idea of the method is the following: firstly we rewrite the equation in terms of the Slotboom variables; then the resulting self-adjoint problem is discretized by means of a primal-mixed method making use of the harmonic average of the diffusion coefficient over the mesh edges; finally, the problem is rewritten in terms of the primal variables by inverting the Slotboom relation so to prevent arithmetic overflow during computations. Under these assumptions maximum principles can be proved to hold also in the discrete setting (see [BMP89]).

The local matrix resulting from applying this procedure to the diffusion-advection equation (10.2) associated with an element $\Omega^{(k)}$, assuming the inverse lexicographical local node numbering, is provided by

$$\begin{bmatrix} \mathcal{B}_{12}^- + \mathcal{B}_{31}^+ & -\mathcal{B}_{12}^+ & -\mathcal{B}_{31}^- & 0 \\ -\mathcal{B}_{12}^- & \mathcal{B}_{12}^+ + \mathcal{B}_{24}^- & 0 & -\mathcal{B}_{24}^+ \\ -\mathcal{B}_{31}^+ & 0 & \mathcal{B}_{43}^+ + \mathcal{B}_{31}^- & -\mathcal{B}_{43}^- \\ 0 & -\mathcal{B}_{24}^- & -\mathcal{B}_{43}^+ & \mathcal{B}_{43}^- + \mathcal{B}_{24}^+ \end{bmatrix},$$

where

$$\mathcal{B}_{ij}^+ = \frac{\ell_{ij} h_{ij}^{(k)}(\varepsilon) B(\psi_i - \psi_j)}{2|\Omega^{(k)}|}, \qquad \mathcal{B}_{ij}^- = \frac{\ell_{ij} h_{ij}^{(k)}(\varepsilon) B(\psi_j - \psi_i)}{2|\Omega^{(k)}|},$$

ℓ_{ij} being the length of the edge joining vertices i and j, ψ_i the value of the advection field ψ at node i, $B(x) = \frac{x}{e^x - 1}$ the Bernoulli function, $h_{ij}^{(k)}(f) = \frac{1}{|\ell_{ij}|} \int_{ij} f^{-1}$ the harmonic mean operator over the edge ij.

10.2.2. Discretization on non-conforming meshes

The quadtree data structure enables to easily deal with non-conforming mesh refinement and coarsening: the refinement operation consists in replacing an element with four children of equal size, while coarsening occurs by removing four children and replacing them with their parent.

Such procedures can lead to the presence of hanging nodes. In this setting the mesh cannot be represented as a Cartesian-product set, and in such cases the Q_h^1 space is not well defined. Therefore the finite element formulation has to be set in a different function space, say $\tilde{Q}_h^1$, obtained starting from Q_h^1 and by imposing a set of constraints in order to account for the presence of hanging nodes – which are not included as additional degrees of freedom – and to preserve the partition of unity property. In particular such constraints correspond to impose the continuity of the numerical solution across non-conforming edges, *i.e.* the solution at a hanging node is the **arithmetic mean** of the values at its parents. Let us analyze now more into details how to manage refinement and coarsening of non-conforming meshes.

In the following we will denote by $\tilde{\tau}_h$ the non-conforming mesh obtained by refining (or coarsening) τ_h and by $\tilde{X}$ the set of vertices defining $\tilde{\tau}_h$.

Non-conforming mesh refinement When non-conformingly refining a mesh element, as shown in fig. 10.3, an additional node (node 5 in the figure) has to be added to the degrees of freedom.

Le now $\bar{\tau}_h$ the partition obtained by uniformly refining τ_h (*i.e.* the minimum-size Cartesian-product mesh containing $\tilde{\tau}_h$). Let finally $\bar{\varphi}_5 \in Q_h^1(\bar{\tau}_h)$ be the basis function associated with node 5 over the uniformly refined mesh.

Define now the following functions:

$$\tilde{\varphi}_i = \varphi_i - \frac{1}{4}\bar{\varphi}_5, \quad i \in 1\ldots 4,$$

and associate them with vertices $1, \ldots, 4$ of the element to be refined.

Let now $\Phi = \{\tilde{\varphi}_i\}_i = \{\{\varphi_i\}_{i \neq 1, \ldots, 4}, \{\tilde{\varphi}_i\}_{i=1}^4, \bar{\varphi}_5\}$. Then the new finite element space over the non-conforming grid is defined as

$$\tilde{Q}_h^1(\tilde{\tau}_h) = \text{span}(\Phi).$$

Figure 10.3.: Example of non-conforming mesh refinement. The blue node corresponds to the newly added degree of freedom. The right mesh $\bar{\tau}_h$ is only used to define the basis function $\bar{\varphi}_5$.

Please remark that this is a linear subspace of $Q^1_h(\tau_h)$ and that the basis functions $\tilde{\varphi}_i \in \Phi$ satisfy the partition of unity property

$$\sum_i \tilde{\varphi}_i(x) = 1, \quad \forall x \in \Omega_h, \tag{10.4}$$

as well as the Lagrangian property

$$\tilde{\varphi}_i(x_j) = \delta_{ij}, \quad \forall x_j \in \tilde{X}. \tag{10.5}$$

Non-conforming mesh coarsening   With reference to fig. 10.4, the degrees of freedom associated with the nodes $5, \dots, 9$ have to be removed since nodes $5, \dots, 8$ become hanging and 9 is no longer a mesh node.

Define now the following functions:

$$\tilde{\varphi}_i = \varphi_i + \frac{1}{4}\varphi_9 + \frac{1}{2}\sum_{j \in \mathcal{N}_i} \varphi_j, \quad i \in 1 \dots 4,$$

where $\mathcal{N}_i$ is the set of hanging nodes sharing an edge with node i, and associate them with vertices $1, \dots, 4$ of the element to be coarsened.

Let now $\Phi = \{\tilde{\varphi}_i\}_i = \{\{\varphi_i\}_{i \neq 1, \dots, 9}, \{\tilde{\varphi}_i\}_{i=1}^4\}$. Then the new finite element space over the non-conforming grid is defined as

$$\tilde{Q}^1_h(\tilde{\tau}_h) = \mathrm{span}\,(\Phi).$$

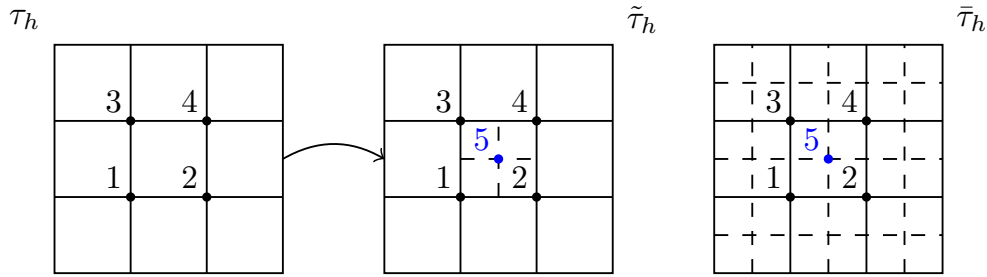Again, this is a linear subspace of $Q^1_h(\tau_h)$ and the functions $\tilde{\varphi}_i \in \Phi$ satisfy the partition of unity and the Lagrangian property (10.4) and (10.5) respectively.
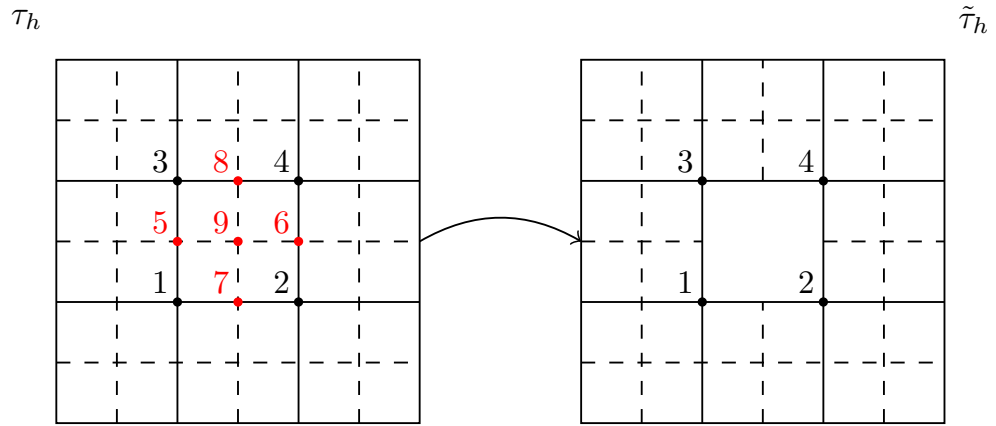
Figure 10.4.: Example of non-conforming mesh coarsening. The red nodes correspond to the removed degrees of freedom.

The formulation illustrated above in the case of non-conforming meshes is equivalent to assembling the local matrices using the non-modified Q_h^1 basis functions on each mesh element; the resulting system is then extended through a set of equations that constrain the solution at each hanging node to be the arithmetic mean of the solution at its two parent vertices. Finally the constraints are eliminated by static condensation.

10.3. Recovery-based estimator

In this section we present the recovery techniques that will enable us to derive the error estimator driving the automatic mesh adaptation procedure.

We extend the results in [Mai+06] for triangular grids to quadtree meshes. In particular, given a finite element solution $u_h \in \tilde{Q}_h^1$ and its gradient $\sigma_h = \nabla u_h \in Q_h^{0,1} \times Q_h^{1,0}$, we first derive a formula to recover an enriched gradient $\sigma_h^* = \nabla^* u_h \in \left(\tilde{Q}_h^1\right)^2$, which is then used to recover an enriched solution $u_h^* \in Q_h^2$ which is piecewise bi-quadratic.

10.3.1. Gradient recovery

In order to compute the recovered gradient, we adopt an averaging technique. Consider a patch centered at an internal node $(x_i, y_j) \in \Omega_h$ as shown in fig. 10.5a.

Let $\{s_{x,i}\}_{i=1}^{N_{s,x}}$ and $\{s_{y,j}\}_{j=1}^{N_{s,y}}$ be the sets of the mesh edges oriented along the x and y axis, respectively. and let $h_{x,i} = x_i - x_{i-1}, h_{y,j} = y_j - y_{j-1}$ denote the lengths of the

(a) Internal node. (b) Node on the bottom boundary.
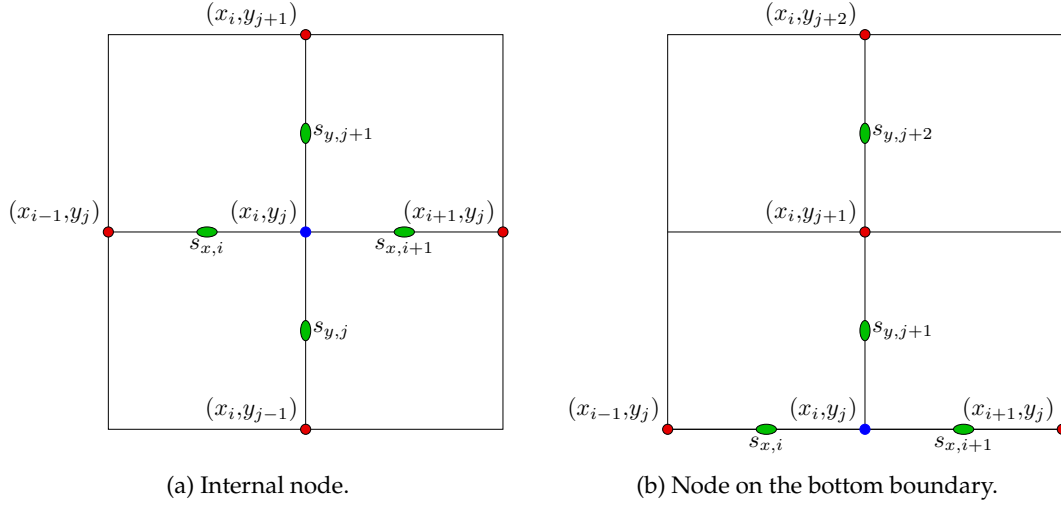
Figure 10.5.: Patch considered to compute the recovered gradient at a mesh node (x_i, y_j).

generic edges $[x_{i-1}, x_i]$ and $[y_{j-1}, y_j]$.

Since the solution u_h is bi-linear, the gradient components can be associated with the degrees of freedom of the Nédélec finite element space (see [Néd80]), and can be computed exactly by using the following finite difference formulas:

$$\sigma_h(s_{x,i}) = \frac{u_h(x_i, y_j) - u_h(x_{i-1}, y_j)}{h_{x,i}} e_1,$$
$$\sigma_h(s_{y,j}) = \frac{u_h(x_i, y_j) - u_h(x_i, y_{j-1})}{h_{y,j}} e_2, \tag{10.6}$$

where e_k is the k-th vector of the canonical basis of $\mathbb{R}^2$.

Then, following [Mai+06], we compute the recovered gradient at (x_i, y_j) by averaging these values with weights given by the reciprocal edge lengths, being:

$$\sigma_h^*(x_i, y_j) = \frac{1}{\frac{1}{h_{x,i}} + \frac{1}{h_{x,i+1}}} \left(\frac{\sigma_h(s_{x,i})}{h_{x,i}} + \frac{\sigma_h(s_{x,i+1})}{h_{x,i+1}} \right) +$$
$$\frac{1}{\frac{1}{h_{y,j}} + \frac{1}{h_{y,j+1}}} \left(\frac{\sigma_h(s_{y,j})}{h_{y,j}} + \frac{\sigma_h(s_{y,j+1})}{h_{y,j+1}} \right). \tag{10.7}$$

If (x_i, y_j) is a node on the boundary or along an internal interface, the patch considered to compute the recovered gradient becomes *unilateral*. An example is shown in fig. 10.5b,

where the formula adopted considers a unilateral patch along the y direction, (x_i, y_j) being a node along the bottom boundary, so that it turns out that

$$\sigma_h^*(x_i, y_j) = \frac{1}{\frac{1}{h_{x,i}} + \frac{1}{h_{x,i+1}}} \left(\frac{\sigma_h(s_{x,i})}{h_{x,i}} + \frac{\sigma_h(s_{x,i+1})}{h_{x,i+1}} \right) +$$

$$\frac{1}{\frac{1}{h_{y,j+1}} + \frac{1}{h_{y,j+2}}} \left[\sigma_h(s_{y,j+1}) \left(\frac{1}{h_{y,j+1}} + \frac{1}{2h_{y,j+2}} \right) - \frac{\sigma_h(s_{y,j+2})}{h_{y,j+2}} \right]. \tag{10.8}$$

Once the recovered values at each degree of freedom are computed, we are able to globally define a recovered gradient $\sigma_h^* \in \tilde{Q}_h^1$. Notice that the presence of hanging nodes does not alter the procedure, since the formula only employs the tangential component of the gradient at each mesh edge, which is continuous also in the case of non-conforming edges.

From the procedure illustrated above the following result can be proved.

Proposition 10.1. *Let $\Omega \subset \mathbb{R}^2$ be an open, bounded domain and let $\tau_h = \left\{ \Omega^{(k)} \right\}_k$ be a quadtree partition of Ω. Let $u \in \mathbb{P}_{2,2}(\Omega)$ be a bi-quadratic polynomial. Then the recovery procedure (10.7)-(10.8) applied to the bi-linear interpolant $\Pi_h^1 u \in \tilde{Q}_h^1(\tau_h)$ of u exactly recovers the gradient $\sigma = \nabla u$ at the partition vertices.*

Proof. Consider the patch shown in figure 10.5a. We aim to prove that $\sigma_h^*(x_i, y_j) = \sigma(x_i, y_j)$ for any internal node (x_i, y_j), since they are a piecewise linear and a linear function, respectively.

We proceed component-wise. Since u is a bi-quadratic polynomial, the following relations hold for the x component σ_x of the exact gradient:

$$\sigma_x(s_{x,i}) = \frac{\Pi_h^1 u(x_i, y_j) - \Pi_h^1 u(x_{i-1}, y_j)}{h_{x,i}},$$

$$\sigma_x(s_{x,i+1}) = \frac{\Pi_h^1 u(x_{i+1}, y_j) - \Pi_h^1 u(x_i, y_j)}{h_{x,i+1}}, \tag{10.9}$$

$$\sigma_x(x_i, y_j) = \frac{1}{\frac{1}{h_{x,i}} + \frac{1}{h_{x,i+1}}} \left(\frac{\sigma_x(s_{x,i})}{h_{x,i}} + \frac{\sigma_x(s_{x,i+1})}{h_{x,i+1}} \right),$$

where the last equality follows from the linearity of σ.

On the other hand, applying the procedure (10.7) to compute the x component $\sigma_{h,x}^*$ of the recovered gradient of $\Pi_h^1 u$ yields

$$\sigma_{h,x}^*(x_i, y_j) = \frac{1}{\frac{1}{h_{x,i}} + \frac{1}{h_{x,i+1}}} \left(\frac{\sigma_{h,x}(s_{x,i})}{h_{x,i}} + \frac{\sigma_{h,x}(s_{x,i+1})}{h_{x,i+1}} \right), \tag{10.10}$$

which, by using (10.6) and (10.9), provides $\sigma_x(x_i, y_j) = \sigma^*_{h,x}(x_i, y_j)$.

The same procedure can be repeated for the y component of the gradient and for boundary nodes, so we conclude the desired equality for each mesh vertex (x_i, y_j).   □

In particular, it holds that $\sigma^*_h(s_{x,i}) = \sigma(s_{x,i}) \; \forall i$ (and similarly for the vertical edges $s_{y,j}$), so we deduce that on each mesh edge the tangential component of the recovered gradient σ^*_h is an exact representation of the tangential component of σ.

From the previous proposition we can also expect that, the recovered gradient is super-convergent with respect to the mesh size $h = \min_k \left(\text{diam} \left(\Omega^{(k)} \right) \right)$, in particular

$$\left\| \sigma^*_h - \sigma \right\|_{L^2(\Omega_h)} = O\left(h^2\right).$$

Analogous properties of super-convergence have been proved in [Wey18] for the gradient approximation provided by the Shortley–Weller method.

10.3.2. Solution recovery

In this section we present a procedure that enables, starting from the recovered gradient σ^*_h, to recover an enriched solution $u^*_h \in Q^2_h(\tau_h)$.

This space is identified by 9 degrees of freedom for each mesh element, as numbered in fig. 10.6a.

Denoting by $u_{h,i} = u_h(x_i)$ the value of u_h at the mesh node x_i and setting the recovered solution at the vertices of $\Omega^{(k)}$ as $u^*_{h,i}|_{\Omega^{(k)}} = u_{h,i}$, $i = 1, \ldots, 4$, the procedure consists of properly integrating σ^*_h in order to compute the values of u^*_h at the degrees of freedom $5, \ldots, 9$, additional with respect to the $\tilde{Q}^1_h$ space.

Denoting by

$$
\begin{aligned}
u^{(1)}_5 &= u_{h,1} + \frac{1}{|y_5 - y_1|} \int_{y_1}^{y_5} \sigma^*_{h,y} \; dy, \\
u^{(2)}_5 &= u_{h,3} - \frac{1}{|y_3 - y_5|} \int_{y_5}^{y_3} \sigma^*_{h,y} \; dy,
\end{aligned}
\tag{10.11}
$$

we assign the value

$$
u^*_{h,5}\Big|_{\Omega^{(k)}} = \frac{u^{(1)}_5 + u^{(2)}_5}{2}
\tag{10.12}
$$

to node 5. Notice that the gradient recovery procedure does not guarantee that σ^*_h represents a conservative vector field, so the two line integrals in (10.11) could differ from each other as they depend on the integration path.

(a) Local numbering of the degrees of freedom associated with the Q_h^2 space on the quadtree mesh element $\Omega^{(k)} \in \tau_h$.

(b) In order to recover a globally continuous solution u_h^*, in the presence of hanging nodes the recovered solution at node 6 on $\Omega^{(2)}$ is assigned equal to $u_{h,6}^*$ as computed on $\Omega^{(1)}$.
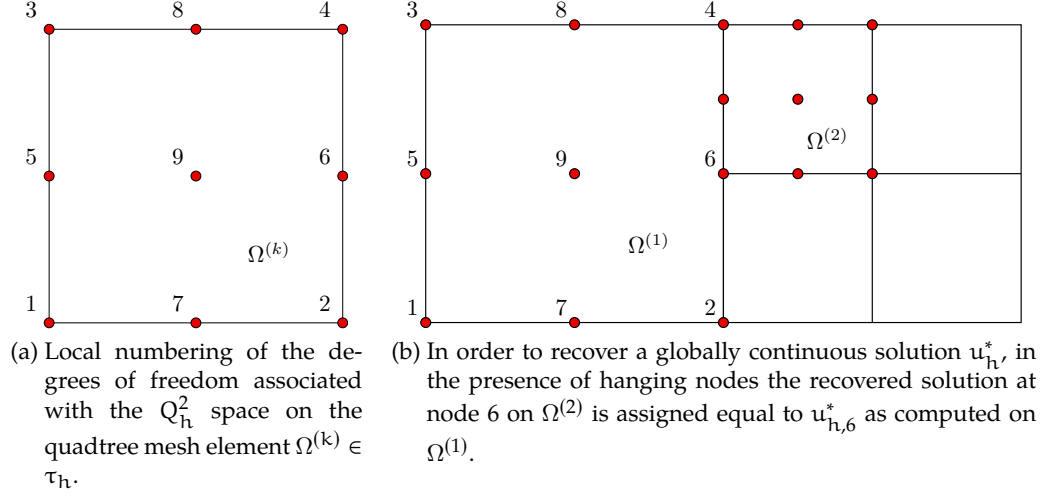
Figure 10.6.: Degrees of freedom for the solution recovery.

Similar formulas can be adopted for the midpoints $6, 7, 8$, while the value at the centroid of the element is computed as:

$$u_{h,9}^* \Big|_{\Omega^{(k)}} = \frac{1}{4} \sum_{i=1}^{4} u_9^{(i)}, \tag{10.13}$$

where

$$
\begin{aligned}
u_9^{(1)} &= u_{h,5} + \frac{1}{|x_9 - x_5|} \int_{x_5}^{x_9} \sigma_{h,x}^* \, dx, \\
u_9^{(2)} &= u_{h,6} - \frac{1}{|x_6 - x_9|} \int_{x_9}^{x_6} \sigma_{h,x}^* \, dx, \\
u_9^{(3)} &= u_{h,7} + \frac{1}{|y_9 - y_7|} \int_{y_7}^{y_9} \sigma_{h,y}^* \, dy, \\
u_9^{(4)} &= u_{h,8} - \frac{1}{|y_8 - y_9|} \int_{y_9}^{y_8} \sigma_{h,y}^* \, dy.
\end{aligned}
\tag{10.14}
$$

The integrals in (10.11) and (10.14) can be exactly computed by the midpoint formula, since the integrand function is linear.

In the presence of non-conforming edges, as shown in fig. 10.6b, the procedure for recovering the solution at hanging nodes is modified as follows: instead of setting

$u_{h,6}^*|_{\Omega^{(2)}} = u_{h,6} = \frac{1}{2}(u_{h,2} + u_{h,4})$ we assign

$$u_{h,6}^*\Big|_{\Omega^{(2)}} = u_{h,6}^*\Big|_{\Omega^{(1)}}, \tag{10.15}$$

i.e. the value recovered using the analogous of formula (10.12) applied to midpoint 6 of element $\Omega^{(1)}$. It is trivial to prove that this procedure provides a recovered solution u_h^* that is continuous also across non-conforming edges.

An analogous result as in proposition 10.1 can be proved also for the recovered solution:

Proposition 10.2. *Let $\Omega \subset \mathbb{R}^2$ be an open, bounded domain and let $\tau_h = \left\{\Omega^{(k)}\right\}_k$ be a quadtree partition of Ω. Let $u \in \mathbb{P}_{2,2}(\Omega)$. Then the solution recovery procedure (10.12), (10.13), (10.15), applied to the bi-linear interpolant $\Pi_h^1 u \in \tilde{Q}_h^1(\tau_h)$ of u exactly recovers the solution u at the partition vertices.*

Again from this result we can expect that the recovered solution converges with order 2 to the exact one, *i.e.*

$$\left\|u_h^* - u\right\|_{L^2(\Omega_h)} = O\left(h^2\right).$$

Other convergence results of numerical schemes for problems with interfaces on Cartesian grids have been investigated in [Wey17] and [DIM17].

10.4. Mesh adaptation procedure

Once the recovered solution u_h^* has been computed, we can define a local error estimator η_k at each mesh element $\Omega^{(k)}$ as

$$\eta_k = \left\|u_h^* - u_h\right\|_{L^2(\Omega^{(k)})},$$

and a global estimator η as:

$$\eta = \left(\sum_k \eta_k^2\right)^{\frac{1}{2}}.$$

We now present two different strategies to generate a mesh able to follow the features of the solution, starting from an initial uniform grid. In both cases the idea is to guarantee the error equi-distribution across all the mesh elements together with a prescribed accuracy on the $L^2(\Omega)$-norm, so that

$$\eta \lessgtr \text{tol},$$

where tol is a user-defined tolerance. Hence it is desirable that the estimator locally satisfies:

$$\eta_k \lessgtr \frac{\text{tol}}{\sqrt{N_{el}}}, \tag{10.16}$$

N_{el} being the mesh cardinality.

The stopping criterion for these strategies relies on fixing the maximum number of iterations, that aims at minimizing the mesh size required to satisfy the prescribed tolerance. This results in keeping the computational effort at a suitable level, as it may become unacceptable – for example when applying iterative methods for non-linear problems – for large meshes. Another possibility consists of monitoring the stagnation of mesh elements, *i.e.* to determine if the relative difference of the cardinality of two successive grids is smaller than a fixed threshold.

10.4.1. Marking-based adaptation

The first approach consists of a standard solve→estimate→mark→adapt iterative procedure. The whole procedure is itemized in algorithm 2, where the parameters δ_1, δ_2 are set equal to 1.5 and 0.5, respectively.

10.4.2. Metric-based adaptation

The second approach we follow is more sophisticated. It is a metric-driven procedure. This means that we are able to predict the number of refinement or coarsening steps required for each mesh element $\Omega^{(k)}$ to satisfy the error equi-distribution and to ensure the desired tolerance. First of all, we scale the local error estimator η_k in order to make it independent on the mesh measure, at least asymptotically (*i.e.* , when the mesh is sufficiently fine), thus lumping this information in a unique multiplicative constant. For this purpose, we divide by a characteristic size of the element, for example $h_x^{(k)}$, the length along the x-direction:

$$\hat{\eta}_k = \frac{\eta_k}{h_x^{(k)}}.$$

Now, we exploit the equi-distribution constraint (10.16) to predict the new size $h_{x,new}^{(k)}$ of each element, being:

$$\hat{\eta}_k h_{x,new}^{(k)} \approx \frac{\text{tol}}{\sqrt{N_{el}}}.$$

Data: the input mesh; the user-defined tolerance tol; the maximum number of
      iterations allowed i_{max};
initialize the iteration counter $i = 0$;
while $i \leq i_{max}$ **do**
    $i = i + 1$;
    compute the numerical solution u_h;
    loop over the mesh elements:
    for $k = 1$ **to** N_{el} **do**
        compute the local estimator η_k;
        if $\eta_k \geq \delta_1 \frac{tol}{\sqrt{N_{el}}}$ **then**
            mark $\Omega^{(k)}$ for refinement;
        else if $\eta_k \leq \delta_2 \frac{tol}{\sqrt{N_{el}}}$ **then**
            mark $\Omega^{(k)}$ for coarsening;
        end
    end
    refine and/or coarsen the mesh;
end

Algorithm 2: Marking-based adaptation.

These two relations yield

$$\frac{h_{x,new}^{(k)}}{h_x^{(k)}} \approx \frac{tol}{\eta_k \sqrt{N_{el}}}.$$

Finally recall that in the case of quadtrees $h_{x,new}^{(k)}/h_x^{(k)} = 2^{-\ell_k}$, so that the number of refinement (or coarsening, if negative) steps ℓ_k required to reach the desired size $h_{x,new}^{(k)}$ can be computed as:

$$\ell_k = \left\lceil \log_2 \left(\frac{\eta_k \sqrt{N_{el}}}{tol} \right) \right\rceil.$$

In order to better control the quality of the generated mesh, we introduced two heuristic integer parameters, namely n_{ref} and $n_{coarsen}$ that play an analogous role as δ_1, δ_2 in the marking approach, so that we finally impose

$$\ell_k = \begin{cases} \max(0, \ell_k - n_{ref}), & \text{if } \ell_k \geq 0, \\ \min(0, \ell_k + n_{coarsen}), & \text{if } \ell_k < 0. \end{cases}$$

The metric-based adaptation procedure is itemized in algorithm 3. The advantage of

Data: the input mesh; the user-defined tolerance tol; the maximum number of
       iterations allowed i_{max};
initialize the iteration counter $i = 0$;
while $i \leq i_{max}$ **do**
    $i = i + 1$;
    compute the numerical solution u_h;
    loop over the mesh elements:
    for $k = 1$ **to** N_{el} **do**
        compute the local estimator η_k;
        compute the number of refinement/coarsening steps ℓ_k;
        refine/coarsen $\Omega^{(k)}$ ℓ_k times;
    end
end

Algorithm 3: Metric-based adaptation.

such an approach is in the predictive feature, so that the final mesh can be obtained by
a lower number of iterations with respect to the marking strategy. We remark that the
choice of the initial mesh plays a role. Indeed, if it is very coarse, the procedure can lead
to overestimate ℓ_k at first steps, so that intermediate iterations can possibly generate an
over-refined mesh.

10.5. Implementation strategies

From an implementation perspective, recent progresses in data structures and algo-
rithms for creating, hierarchically refining, balancing and partitioning meshes of quad-
and oct-trees has brought this class of grids to the forefront of the research interests in
the HPC community as a key tool for attaining extreme scalability. Achieving this goal
drives the development of an efficient, parallel, scalable code.

Different libraries providing support to quadtree data structures are available, such
as p4est[1], PABLO[2] and Gerris[3].

Given the availability of several libraries to create and manage octree meshes that are
currently under active development, we decided to develop a generic high-level C++
mesh interface that enables to decouple the PDE discretization scheme from the back-

---

[1] http://www.p4est.org/
[2] http://optimad.github.io/PABLO/
[3] http://gfs.sourceforge.net/

end meshing library. The first supported back-end in our implementation was chosen to be `p4est` which has been preferred to other alternatives for its ability to work with forests of octrees and for its impressive scalability, yet our design is intended to support interfaces to other libraries in the future.

We have also considered integrating our algorithm into the general purpose finite element library `deal.II`[4], which uses `p4est` as the default mesh management engine. Preliminary tests have shown, though, that the great generality of `deal.II` comes at the cost of introducing a non-negligible amount of overhead that can be highly reduced exploiting the features of the specific discretization algorithms described in sections 10.2 and 10.4.

10.5.1. `bim++`: a C++ interface to `p4est`

The provided implementation was integrated into the in-house `bim++` library. In a first instance, the interface to `p4est` has been implemented by defining a class `quadrant_t` that provides methods to access the information of a quadrant, such as

- its local and global indices;

- the index of the tree it belongs to;

- the coordinates of its vertices;

- the rank-local and global indices of its vertices;

- whether a vertex is hanging and, if this is the case, the rank-local and global indices of its parent vertices;

- the index of the edge that boundary nodes lay on.

The declaration of such methods is reported in listing 1.

```
1  /// C++ interface class to access properties of the
2  /// current quadrant.
3  class
4  quadrant_t
5  {
6  public:
7    /// Simple constructor needs at least a pointer
```

----
[4]https://www.dealii.org/

```
8    /// to the container tmesh.
9    quadrant_t (tmesh * _tmesh,
10              p4est_topidx_t _tree,
11              p4est_quadrant_t * _quadrant);

12   /// Get the i-th coordinate of the j-th vertex.
13   double p (idx_t i, idx_t j);

14   /// Get the i-th coordinate of the centroid.
15   double centroid (idx_t i);

16   /// Get rank-local index of the i-th vertex, or global index for ghosts.
17   idx_t t (idx_t i);

18   /// Get global index of the i-th vertex
19   idx_t gt (idx_t i);

20   /// True if the i-th vertex is hanging.
21   bool is_hanging (idx_t i);

22   /// Return the rank-local (or global for ghosts)
23   /// ip-th parent for the in-th vertex.
24   int parent (idx_t ip, idx_t in);

25   /// Return the ip-th parent for the in-th vertex,
26   /// use global numbering.
27   int gparent (idx_t ip, idx_t in);

28   static const idx_t NOT_ON_BOUNDARY = P4EST_ROOT_LEN + 1;

29   /// Index of the edge of the current tree
30   /// on which the i-th vertex lies, return
31   /// NOT_ON_BOUNDARY if an interior vertex.
32   idx_t e (idx_t i);

33   /// Get an iterator to the first neighbor
34   /// of the current quadrant.
35   neighbor_iterator begin_neighbor_sweep ();
```

```
36    /// Get a null quadrant iterator to signal end of the sweep.
37    neighbor_iterator end_neighbor_sweep ();

38    /// Return index of current quadrant across all
39    /// trees on current process.
40    p4est_locidx_t get_forest_quad_idx ();

41    /// Return index of current quadrant in current
42    /// tree on current process.
43    p4est_locidx_t get_tree_quad_idx ();

44    /// Return index of current quadrant across all
45    /// trees on all processes.
46    p4est_gloidx_t get_global_quad_idx ();

47    /// Return index of current tree.
48    p4est_locidx_t get_tree_idx ();

49    /// Update stored data.
50    void update (p4est_topidx_t tree,
51                 p4est_quadrant_t * q);
52  };
```

Listing 1: Quadrant interface.

On top of the `quadrant_t` we developed a double iterator interface that aims at looping over both

- the local mesh, *i.e.* all the quadrants owned by current process in order to perform operations such as computing local differential operators, etc.;

- the first face neighbors of current quadrant, as required by the gradient recovery procedure.

They are implemented in the classes `quadrant_iterator` and `neighbor_iterator`, whose interface is provided in listing 2. Methods to iterate over the first neighbors are available in the `quadrant_t` class.

```
1   /// Iterator to sweep through the quadrants of a tmesh.
2   /// This is essentially a decorator of quadrant_t *.
3   class
4   quadrant_iterator
5   {
6   public:
7     /// Get next quadrant.
8     void operator++ ();

9     /// Dereference.
10    quadrant_t& operator* ();

11    /// Operator -> to get access to the wrapped pointer.
12    quadrant_t * operator-> ();

13    /// Compare two quadrant_iterator objects.
14    bool operator== (const quadrant_iterator & other);

15    /// Default constructor.
16    quadrant_iterator (quadrant_t * _data);

17    /// Move to first forest quadrant.
18    void reset ();

19  protected:
20    quadrant_t * data;
21  };

22  /// Iterator to sweep through quadrants that are
23  /// neighbors of a quadrant.
24  class
25  neighbor_iterator : public quadrant_iterator
26  {
27  public:
28    /// Get next neighbor.
29    void operator++ ();

30    /// Default constructor.
```

```
31    neighbor_iterator (quadrant_t * _data);
32  };
```

Listing 2: Quadrant and neighbor iterators.

Finally, a class to handle a whole mesh is defined, as implemented in listing 3. The class `tmesh` basically contains methods to

- create a forest of quadtrees;

- load (save) a forest from (to) file;

- export nodal and quadrant-constant fields to a format that is convertible to a VTK[5] unstructured grid file;

- set markers for mesh refinement and coarsening;

- set the metric-based marker defined in section 10.4 for mesh adaptation;

- actually perform mesh adaptation;

- compute the information about the owned quadrants;

- transmit the information about ghost and mirror quadrants among different processes;

- iterate over the local mesh quadrants through the iterator interface;

- get the information about the local and global mesh properties.

```
1  class tmesh
2  {
3  public:
4    using idx_t = p4est_gloidx_t;

5    /// Default constructor, set all pointers to nullptr.
6    tmesh (MPI_Comm _comm);

7    /// Load a p4est and connectivity from a file.
```

---

[5]https://www.vtk.org/

```
8     tmesh (const char * filename,
9            MPI_Comm _comm);

10    /// Save the p4est and connectivity to a file.
11    void save (const char * filename);

12    /// Load the p4est and connectivity from a file.
13    void load (const char * filename);

14    /// Export exploded mesh to a vtk file for visualization.
15    void vtk_export (const char * filename);

16    /// Export nodal field f to a octbin.gz file for visualization.
17    void octbin_export (const char * basename,
18                        const distributed_vector & f);

19    /// Export quadrant field f to a octbin.gz file for visualization.
20    void octbin_export_quadrant (const char * filename,
21                                 const std::vector<double> & f);

22    /// Get an iterator to the first quadrant of the mesh.
23    quadrant_iterator begin_quadrant_sweep ();

24    /// Get a null quadrant iterator to signal end of the sweep.
25    quadrant_iterator end_quadrant_sweep ();

26    /// Mark quadrants for refinement based on fun.
27    void set_refine_marker (std::function<int (quadrant_iterator)> fun);

28    /// Mark quadrants for coarsening based on fun.
29    void set_coarsen_marker (std::function<int (quadrant_iterator)> fun);

30    /// Mark quadrants for refinement based on metrics.
31    void set_metrics_marker (std::function<double (quadrant_iterator)>,
32                             double tol,
33                             int max_depth,
34                             int n_refine,
35                             int n_coarsen);
```

```
36    /// Refine marked quadrants, balance the quadtree and
37    /// re-partition over the processors.
38    void refine (int recursive,
39                 int partforcoarsen,
40                 int balance);

41    /// Refine marked quadrants based on metrics.
42    void metrics_refine (idx_t max_elems);

43    /// Coarsen marked quadrants, balance the quadtree and
44    /// re-partition over the processors.
45    void coarsen (int recursive,
46                  int partforcoarsen,
47                  int balance);

48    /// Compute nodes numbering and quadrant neighbours.
49    void update ();

50    /// Send mirrors and receive ghosts from other ranks.
51    void update_mirrors_ghosts ();

52    /// Return number of nodes owned by local process.
53    idx_t num_owned_nodes ();

54    /// Return number of nodes of quadrants owned
55    /// or shared by local process.
56    idx_t num_local_nodes ();

57    /// Return total number of quadrants owned by all process.
58    idx_t num_global_nodes ();

59    /// Return number of quadrants owned by local process
60    /// across all trees.
61    idx_t num_local_quadrants ();

62    /// Return number of quadrants owned by all processes
63    /// across all trees.
```

```
64    idx_t num_global_quadrants ();
65  };
```

Listing 3: Class `tmesh`.

10.5.2. Distributed vector

The additional class `distributed_vector`, in listing 4 has been implemented to reduce the memory consumption deriving from the storage of nodal coefficient and state vectors. For the specific numerical application it is required that each rank only stores values corresponding to owned or local nodes, while non-local values can be discarded.

```
1   class
2   distributed_vector
3   {
4   public:

5     /// Access operator.
6     double & operator[] (int idx);

7     /// Determine ghost and mirror maps.
8     void remap ();
9     /// Communicate values among sharing processes.
10    void assemble ();

11    /// Get is.
12    int get_range_start () const;
13    /// Get ie.
14    int get_range_end () const;

15    /// Get global vector size.
16    int size ();

17    /// Resets all the non-owned maps.
18    void clear_non_owned ();

19  private:
20    int owned_count; ///< Number of owned entries.
```

```cpp
21    int is, ie; ///< Start and end indices.

22    /// Vector entries owned by the current rank.
23    std::vector<double> owned_data;

24    /// Vector entries touched by the current rank
25    /// that belong to another process.
26    std::map<int, double> non_owned_data;

27    /// Structure to hold data of ghost entries
28    /// in a format amenable for send/receive.
29    struct
30    ghosts_t
31    {
32      std::vector<int> prc_ptr, row_ind, rank_nnz;
33      std::vector<double> a;
34    } ghosts;

35    /// Copy data from non_local_data to ghosts.
36    void ghost_csr ();

37    /// Update ghosts.
38    void ghost_csr_update ();

39    /// Structure to hold data of mirror entries
40    /// in a format amenable for send/receive.
41    struct mirrors_t
42    {
43      std::vector<int> prc_ptr, row_ind, rank_nnz;
44      std::vector<double> a;
45    } mirrors;

46    /// Vector entries that are owned by rank i
47    /// are numbered between ranges[i]
48    /// and ranges[i+1].
49    std::vector<int> ranges;
50  };
```
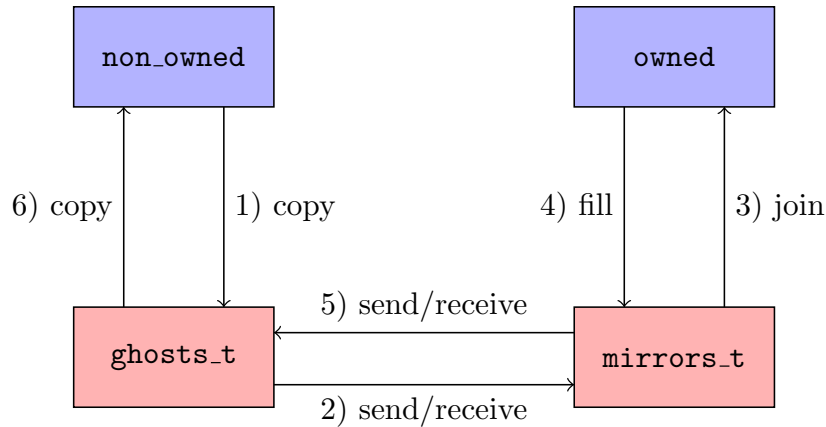
Figure 10.7.: Communication diagram for the parallel assembly of a distributed vector.

Listing 4: Class `distributed_vector`.

The `distributed_vector` class stores the values of owned nodes, that are numbered with contiguous indices, in the `std::vector owned_data`, while non-owned local values are stored in a `std::map` accessed with the global index of the non-owned node.

The data transfer procedure, diagrammed in fig. 10.7, can be summarized as follows:

1. `ghosts_t` is filled with the `non_owned_data` structure;

2. ghost indices and sent to other processes, that store them into `mirrors_t`;

3. mirror data are joined into the ones already in `owned_data` by a user-defined operation, for example by summing the values corresponding to the same index;

4. `mirrors_t` is filled with the `owned_data` structure;

5. mirror data are sent to other processes, that store them into `ghosts_t`;

6. ghost data are copied into `non_owned_data`.

The two first steps are performed by the method `remap ()`, while the others are taken care of by `assemble ()`. The structures `ghosts_t` and `mirrors_t` store their data in a Compressed Sparse Row (CSR)-like format that is amenable for `MPI` communications:

rank_nnz contains the numbers of nonzero entries that the current rank shares with each of the other processes;

row_ind contains the corresponding shared indices;

a contains the corresponding shared values;

prc_ptr contains the cumulative sum of `rank_nnz`, used to identify the starting index per rank in `row_ind` and `a`.

The usage of a `distributed_vector` is consequently straightforward, as the access operator of a vector `u` enables to write expressions like `u[i]` that automatically detect whether the index `i` corresponds to an owned or a non-local entry and accesses it either from the owned vector or from the map accordingly.

A distributed sparse matrix class with an analogous interface has also been implemented so that the matrix assembled from the discretization of a differential operator can be parallel partitioned by splitting it into rows of owned nodes, depending on their numbering and their owning process, augmented by the rows corresponding to local non-owned indices.

10.5.3. Interpolation

Among the challenging tasks that show up when dealing with adaptive meshes is to transmit a solution vector from one mesh to a new one obtained by refinement or coarsening. This kind of procedure is of central relevance in iterative strategies for non-linear or time-dependent problems, where the solution at the current step has to be somehow reprocessed to perform the subsequent iterations. The nature of quadtree meshes makes this operation straightforward, except for some implementation details that will be provided hereafter.

The idea comes from the hierarchical structure of a quadtree mesh and consists of defining an interpolation map at every quadrant. The map has exactly four entries, one per vertex, constructed as follows: given $v = 1, \ldots, 4$, if node v is non-hanging, then the v-th map entry is the pair $(i_v, 1)$, where i_v is the global index of the degree of freedom associated with vertex v and 1 is the identity contribution; otherwise, if v is hanging, then the v-th map entry is a couple of pairs (k_{v_1}, w_1) and (k_{v_2}, w_2), where k_{v_1}, k_{v_2} are the indices of the two parents of v and w_1, w_2 are the corresponding weight used to preserve the partition of unity property (following the description in section 10.2.2 we set $w_1 = w_2 = \frac{1}{2}$).

Once constructed, the map can easily be converted to a 4-by-4 interpolation matrix, noticing that due to the 2:1 balancing the set $\{i_v, k_{v_1}, k_{v_2}\}_{v=1,\ldots,4}$ has always exactly four elements, that can be associated to the matrix columns.

$\Omega^{(1)}$	1	2	3	4
1	1	0	0	0
2	0	1	0	0
3	0	0	1	0
4	0	0	0	1

$\Omega^{(2)}$	2	4	5	6
2	1	0	0	0
5	0	0	1	0
*	$\frac{1}{2}$	$\frac{1}{2}$	0	0
6	0	0	0	1

$\Omega^{(4)}$	2	4	6	9
*	$\frac{1}{2}$	$\frac{1}{2}$	0	0
6	0	0	1	0
4	0	1	0	0
*	0	$\frac{1}{2}$	0	$\frac{1}{2}$

Table 10.1.: Example interpolation matrices for the mesh shown in fig. 10.8.

p4est enables to associate a `void *` pointer, called `user_data`, to each quadrant and to provide a callback function to replace such a data structure during refinement or coarsening steps. The `user_data` that we assigned to the mesh quadrants is of class `data_t`, whose declaration is provided in listing 5. It contains, besides an integer to determine the number of refinement or coarsening steps to be performed, two data members that correspond to the 4-by-4 interpolation coefficient matrix, computed as described above, and the array of the associated interpolation indices $\{i_\nu\}_{\nu=1,\dots,4}$.

```
1   /// Struct for p4est user_data.
2   struct data_t
3   {
4     /// Number of refinement (coarsening, if negative) steps to be performed.
5     int refine_count;
6
6     /// Interpolation indices, i.e. the indices
7     /// associated to interp_coeff columns.
8     std::array<tmesh::idx_t, 4> interp_idx;
9
9     /// Interpolation coefficients at the four vertices.
10    std::array<std::array<double, 4>, 4> interp_coeff;
11  };
```

Listing 5: Data structure for p4est `user_data`.

Table 10.1 shows the interpolation matrices associated with some of the elements of the example mesh in fig. 10.8.

If, during the adaptation procedure, a generic element $\Omega^{(k)}$ is marked for refinement, the interpolation matrices of its i-th children quadrant $\Omega_i^{(k)}$, $i = 1,\dots,4$ can be computed by multiplying the interpolation matrix $M_{\Omega^{(k)}}$ of its parent quadrant by the
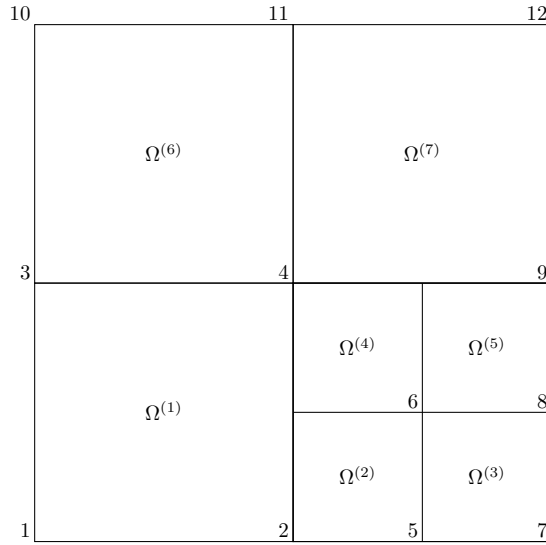
Figure 10.8.: Example mesh used to clarify the building of interpolation matrices.

corresponding local interpolation matrix $M_{\Omega_i^{(k)}}$, defined as follows:

$$
M_{\Omega_1^{(k)}} = \begin{pmatrix} 1 & 0 & 0 & 0 \\ \frac{1}{2} & \frac{1}{2} & 0 & 0 \\ \frac{1}{2} & 0 & \frac{1}{2} & 0 \\ \frac{1}{4} & \frac{1}{4} & \frac{1}{4} & \frac{1}{4} \end{pmatrix}, \quad
M_{\Omega_2^{(k)}} = \begin{pmatrix} \frac{1}{2} & \frac{1}{2} & 0 & 0 \\ 0 & 1 & 0 & 0 \\ \frac{1}{4} & \frac{1}{4} & \frac{1}{4} & \frac{1}{4} \\ 0 & \frac{1}{2} & 0 & \frac{1}{2} \end{pmatrix},
$$

$$
M_{\Omega_3^{(k)}} = \begin{pmatrix} \frac{1}{2} & 0 & \frac{1}{2} & 0 \\ \frac{1}{4} & \frac{1}{4} & \frac{1}{4} & \frac{1}{4} \\ 0 & 0 & 1 & 0 \\ 0 & 0 & \frac{1}{2} & \frac{1}{2} \end{pmatrix}, \quad
M_{\Omega_4^{(k)}} = \begin{pmatrix} \frac{1}{4} & \frac{1}{4} & \frac{1}{4} & \frac{1}{4} \\ 0 & \frac{1}{2} & 0 & \frac{1}{2} \\ 0 & 0 & \frac{1}{2} & \frac{1}{2} \\ 0 & 0 & 0 & 1 \end{pmatrix},
$$

where we assumed the four children to be numbered following the above-mentioned s-ordering).

Conversely, if four children are marked for coarsening then the interpolation matrix of their parent quadrant is assembled by simply joining the identity entry – *i.e.* the one equal to 1 with its corresponding index – of the i-th row of $M_{\Omega_i^{(k)}}$ for $i = 1, \dots, 4$. Notice that such identity entries always exist due to the tree balancing. In the example of fig. 10.8, if quadrants $\{\Omega^{(k)}\}_{k=2,\dots,5}$ were marked for coarsening, their parent quadrant

would replace their interpolation matrices with:

$$\begin{pmatrix} 1 & 0 & 0 & 0 \\ 0 & 0 & 1 & 0 \\ 0 & 1 & 0 & 0 \\ 0 & 0 & 0 & 1 \end{pmatrix},$$

whose columns are associated with nodes $2, 4, 7, 9$, respectively. Therefore the provided replace callback function brings `refine_count` closer to zero by one unit and replaces the `user_data` through one of the two former algorithms, depending on whether the element is being refined or four children coarsened.

The metric-driven approach often consists of multiple refinement or coarsening steps performed simultaneously. This procedure can be easily extended to this case by properly multiplying different interpolation matrices, each one associated with a single step.

References

[AFN19]   P. C. Africa, C. de Falco, and D. Natali. "A Note on Thermodynamically Consistent Flux Discretization". In: *In preparation* (2019) (cit. on pp. 23, 59, 93).

[AFP19]   P. C. Africa, C. de Falco, and S. Perotto. "Scalable Recovery-based Adaptation on Quadtree Meshes". In: *In preparation* (2019) (cit. on pp. 24, 97, 133).

[BCC98]   R. E. Bank, W. M. Coughran Jr, and L. C. Cowsar. "The Finite Volume Scharfetter-Gummel Method for Steady Convection Diffusion Equations". In: *Computing and Visualization in Science* 1.3 (1998), pp. 123–136 (cit. on pp. 93, 101).

[BMM03]   S. Bellavia, M. Macconi, and B. Morini. "An Affine Scaling Trust-region Approach to Bound-constrained Nonlinear Systems". In: *Applied Numerical Mathematics* 44.3 (2003), pp. 257–280 (cit. on p. 90).

[BMP89]   F. Brezzi, L. D. Marini, and P. Pietra. "Two-dimensional Exponential Fitting and Applications to Drift-diffusion Models". In: *Siam Journal on Numerical Analysis* 26.6 (1989), pp. 1342–1355 (cit. on p. 101).

[Boc11]   P. Bochev. *Control Volume Finite Element Method with Multidimensional Edge Element Scharfetter-Gummel Upwinding. Part 1. Formulation*. Tech. rep. Sandia National Laboratories, 2011 (cit. on p. 93).

[BP11]   P. Bochev and K. Peterson. *Control Volume Finite Element Method with Multidimensional Edge Element Scharfetter-Gummel Upwinding. Part 2. Computational Study*. Tech. rep. Sandia National Laboratories, 2011 (cit. on p. 93).

[BR81]   R. E. Bank and D. J. Rose. "Global Approximate Newton Methods". In: *Numerische Mathematik* 37.2 (1981), pp. 279–295 (cit. on p. 88).

[BS90]   P. N. Brown and Y. Saad. "Hybrid Krylov Methods for Nonlinear Systems of Equations". In: *SIAM Journal on Scientific and Statistical Computing* 11.3 (1990), pp. 450–481 (cit. on pp. 87, 91).

[But16]   J. C. Butcher. *Numerical Methods for Ordinary Differential Equations*. John Wiley & Sons, 2016 (cit. on p. 76).

References

[BWG11]   C. Burstedde, L. C. Wilcox, and O. Ghattas. "`p4est`: Scalable Algorithms for Parallel Adaptive Mesh Refinement on Forests of Octrees". In: *SIAM Journal on Scientific Computing* 33.3 (2011), pp. 1103–1133 (cit. on pp. 97, 99).

[Căt05]   E. Cătinaş. "The Inexact, Inexact Perturbed, and Quasi-Newton Methods Are Equivalent Models". In: *Mathematics of Computation* 74.249 (2005), pp. 291–301 (cit. on p. 81).

[CV17]   J. Chen and C. Vuik. "Globalization Technique for Projected Newton-Krylov Methods". In: *International Journal for Numerical Methods in Engineering* 110.7 (2017), pp. 661–674 (cit. on p. 88).

[Deu11]   P. Deuflhard. *Newton Methods for Nonlinear Problems: Affine Invariance and Adaptive Algorithms*. Vol. 35. Springer Science & Business Media, 2011 (cit. on p. 81).

[DIM17]   A. De Brauer, A. Iollo, and T. Milcent. "A Cartesian Scheme for Compressible Multimaterial Hyperelastic Models with Plasticity". In: *Communications in Computational Physics* 22.5 (2017), pp. 1362–1384 (cit. on p. 109).

[DM74]   J. E. Dennis and J. J. Moré. "A Characterization of Superlinear Convergence and Its Application to Quasi-Newton Methods". In: *Mathematics of Computation* 28.126 (1974), pp. 549–560 (cit. on p. 85).

[DM77]   J. E. Dennis Jr and J. J. Moré. "Quasi-Newton Methods, Motivation and Theory". In: *SIAM Review* 19.1 (1977), pp. 46–89 (cit. on p. 83).

[EW94]   S. C. Eisenstat and H. F. Walker. "Globally Convergent Inexact Newton Methods". In: *SIAM Journal on Optimization* 4.2 (1994), pp. 393–422 (cit. on p. 85).

[EW96]   S. C. Eisenstat and H. F. Walker. "Choosing the Forcing Terms in an Inexact Newton Method". In: *SIAM Journal on Scientific Computing* 17.1 (1996), pp. 16–32 (cit. on p. 86).

[GS55]   D. N. de G. Allen and R. V. Southwell. "Relaxation Methods Applied to Determine the Motion, in Two Dimensions, of a Viscous Fluid Past a Fixed Cylinder". In: *The Quarterly Journal of Mechanics and Applied Mathematics* 8.2 (1955), pp. 129–145 (cit. on p. 101).

[HNW87]   E. Hairer, S. P. Norsett, and G. Wanner. *Solving Ordinary Differential Equations I, Computational Mathematics, Vol. 8*. 1987 (cit. on p. 79).

[Kel03]   C. T. Kelley. *Solving Nonlinear Equations with Newton's Method*. Vol. 1. Siam, 2003 (cit. on p. 87).

128

[KK04]   D. A. Knoll and D. E. Keyes. "Jacobian-free Newton-Krylov Methods: A Survey of Approaches and Applications". In: *Journal of Computational Physics* 193.2 (2004), pp. 357–397 (cit. on p. 88).

[Mai+06]   G. Maisano, S. Micheletti, S. Perotto, and C. L. Bottasso. "On Some New Recovery-based a Posteriori Error Estimators". In: *Computer Methods in Applied Mechanics and Engineering* 195.37 (2006), pp. 4794–4815. ISSN: 0045-7825 (cit. on pp. 104, 105).

[MW94]   J. J. H. Miller and S. Wang. "An Analysis of the Scharfetter-Gummel Box Method for the Stationary Semiconductor Device Equations". In: *Rairo-modélisation Mathématique Et Analyse Numérique* 28.2 (1994), pp. 123–140 (cit. on p. 93).

[MZ88]   P. A. Markowich and M. A. Zlámal. "Inverse-average-type Finite Element Discretizations of Selfadjoint Second-order Elliptic Problems". In: *Mathematics of Computation* 51.184 (1988), pp. 431–449 (cit. on p. 101).

[Néd80]   J.-C. Nédélec. "Mixed Finite Elements in $\mathbb{R}^3$". In: *Numerische Mathematik* 35.3 (1980), pp. 315–341 (cit. on p. 105).

[Pow70]   M. J. D. Powell. "A Hybrid Method for Nonlinear Equations". In: *Numerical Methods for Nonlinear Algebraic Equations* (1970) (cit. on p. 91).

[Sch70]   L. K. Schubert. "Modification of a Quasi-Newton Method for Nonlinear Equations with a Sparse Jacobian". In: *Mathematics of Computation* 24.109 (1970), pp. 27–30 (cit. on p. 85).

[SG69]   D. L. Scharfetter and H. K. Gummel. "Large-signal Analysis of a Silicon Read Diode Oscillator". In: *IEEE Transactions on Electron Devices* 16.1 (1969), pp. 64–77 (cit. on p. 95).

[Sha99]   H. Shao. "Numerical Analysis of Meshing and Discretization for Anisotropic Convection-diffusion Equations with Applications". PhD thesis. Duke University, 1999 (cit. on p. 94).

[SS86]   Y. Saad and M. H. Schultz. "Gmres: A Generalized Minimal Residual Algorithm for Solving Nonsymmetric Linear Systems". In: *SIAM Journal on Scientific and Statistical Computing* 7.3 (1986), pp. 856–869 (cit. on p. 88).

[Wey17]   L. Weynans. "Convergence of a Cartesian Method for Elliptic Problems with Immersed Interfaces". PhD thesis. INRIA Bordeaux; Univ. Bordeaux, 2017 (cit. on p. 109).

References

[Wey18]   L. Weynans. "Super-convergence in Maximum Norm of the Gradient for the Shortley-Weller Method". In: *Journal of Scientific Computing* 75.2 (2018), pp. 625–637 (cit. on p. 107).

[Zlá86]   M. A. Zlámal. "Finite Element Solution of the Fundamental Equations of Semiconductor Devices. I". In: *Mathematics of Computation* 46.173 (1986), pp. 27–43 (cit. on p. 101).

Part IV.

Numerical results

11. Adaptation test cases

Here we present some numerical results obtained by the application of the mesh adaptation algorithm described in chapter 10 to a class of linear ADR problems. Elliptic problems with boundary or interior layers will be discussed in section 11.1. Weak scaling results are presented in section 11.2. A parabolic test case with a solution characterized by propagating front is finally presented in section 11.3.

11.1. Quadtree adaptation for linear ADR problems

In the following sections we will describe diffusion-reaction examples with boundary layers, with coefficient discontinuities and a diffusion-advection problem with an internal layer and discontinuous boundary conditions, respectively. The test cases presented are taken from [AFP19].

11.1.1. Diffusion-reaction examples with multiple layers

11.1.1.1. Example with two boundary layers

The first test case we analyze is a diffusion-reaction equation with constant coefficients over the unit square $\Omega = \Omega_h = (0,1)^2$, whose solution has two boundary layers along the top and right sides. Here $\varepsilon = 10^{-4}$, $r = 1$ and f, g are such that the problem has exact solution

$$u_{ex}(x,y) = \left(1 - \frac{\sinh(x/\sqrt{\varepsilon})}{\sinh(1/\sqrt{\varepsilon})}\right)\left(1 - \frac{\sinh(y/\sqrt{\varepsilon})}{\sinh(1/\sqrt{\varepsilon})}\right).$$

The numerical solution and the meshes obtained with the adaptation procedure using the marking-based and the metric-based techniques are shown in figs. 11.1 to 11.3 respectively. The metric-based adaptation provides a mesh that is refined in a thinner boundary region with respect to the marking approach.

Figure 11.4 shows the convergence of the L^2-norm and H^1-seminorm of the error associated with both the discrete solution u_h and the recovered solution u_h^* as a function of the mesh size h. The results are as expected, providing convergence with order 1 for the numerical gradient and 2 for the numerical solution and the recovered gradient
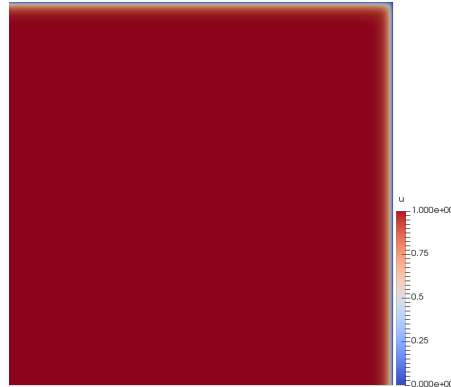
Figure 11.1.: Problem 11.1.1.1. Numerical solution.

and solution. A comparison between the adaptive and uniform adaptation strategies is also drawn, proving that the benefits of the adaptive procedure become evident in particular when the number of dofs increases. The effectivity index

$$\xi = \frac{\eta}{\|u_{ex} - u_h\|_{L^2(\Omega_h)}},$$

associated with the error estimator η has also been computed at each adaptation step. The resulting plot is shown in fig. 11.5, together with the histogram of the element sizes estimated by the metrics: both figures clearly show that, despite the 2:1 balancing, the resulting mesh is *uniform* if evaluated through the error estimator, as most elements have the same (small) size and the effectivity index stagnates asymptotically to a value of about 0.8, meaning that the estimator is underestimating the error of the same factor.

11.1.1.2. Example with two boundary layers and a corner layer

Here we study a test proposed in [FO09]. It has the form of problem (10.1), with $\varepsilon = 2^{-15}$, $b(x,y) = 1 + x^2 y^2 / 1000$, $f(x,y) = 1 + 2xy/1000$ and the following boundary conditions:

$$u(x,y) = \begin{cases} 1, & \text{on } \{x = 0\} \cup \{y = 0\}, \\ 1 - y^2, & \text{on } \{x = 1\}, \\ 1 - x^2, & \text{on } \{y = 1\}. \end{cases}$$

The meshes obtained during the adaptation procedure using the marking-based and the metric-based techniques are shown in figs. 11.6 and 11.7 respectively.
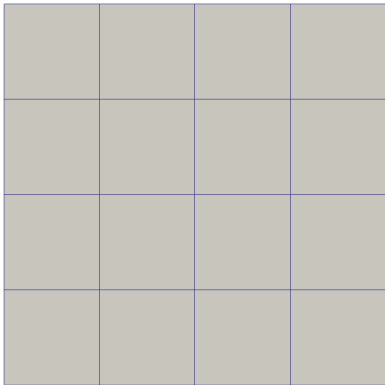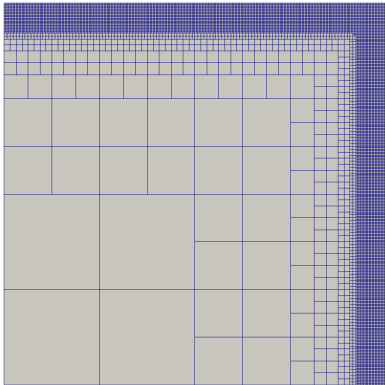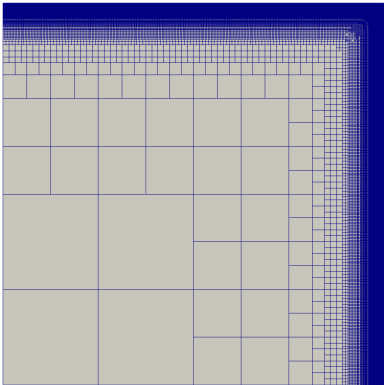
(a) Initial mesh.
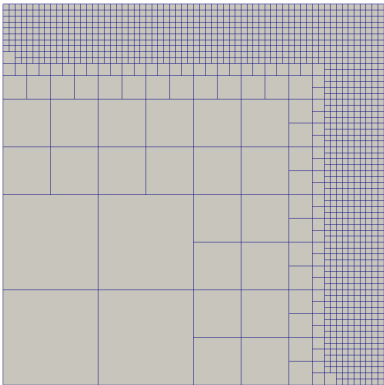
(b) Mesh at adaptation step 4.

(c) Mesh at adaptation step 6.

(d) Mesh at adaptation step 9.

Figure 11.2.: Problem 11.1.1.1. Marking-based adaptation.
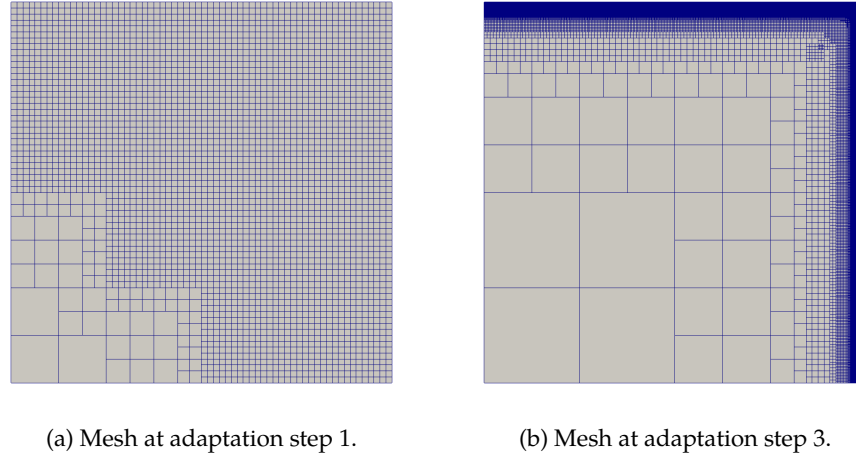
(a) Mesh at adaptation step 1.

(b) Mesh at adaptation step 3.

Figure 11.3.: Problem 11.1.1.1. Metric-based adaptation.

(a) Convergence of numerical errors with respect to the mesh size h.

(b) Comparison of adaptive mesh strategy vs. uniform refinement: the plot shows the error $\|u - u_h\|_{L^2(\Omega_h)}$ as a function of the number of degrees of freedom.
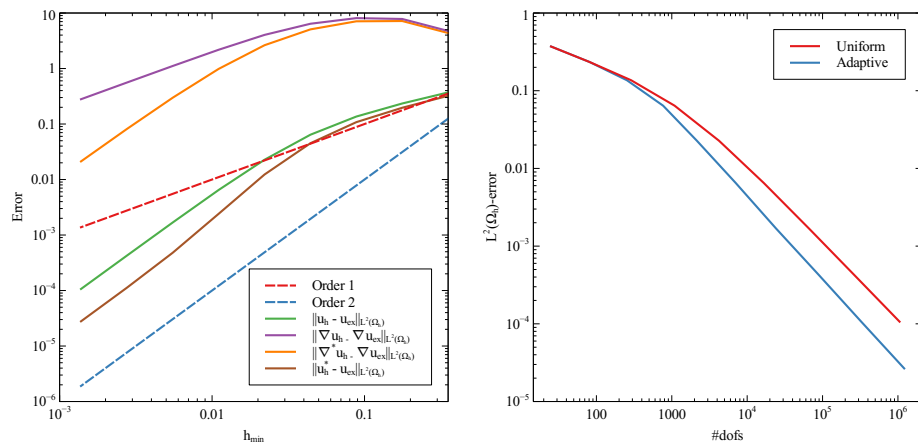
Figure 11.4.: Problem 11.1.1.1. Numerical errors and comparison of adaptive vs. uniform refinement.

(a) Effectivity index ξ as a function of the adaptive iteration.

(b) Histogram of the element size $h_x^{(k)}$ computed by the metrics.
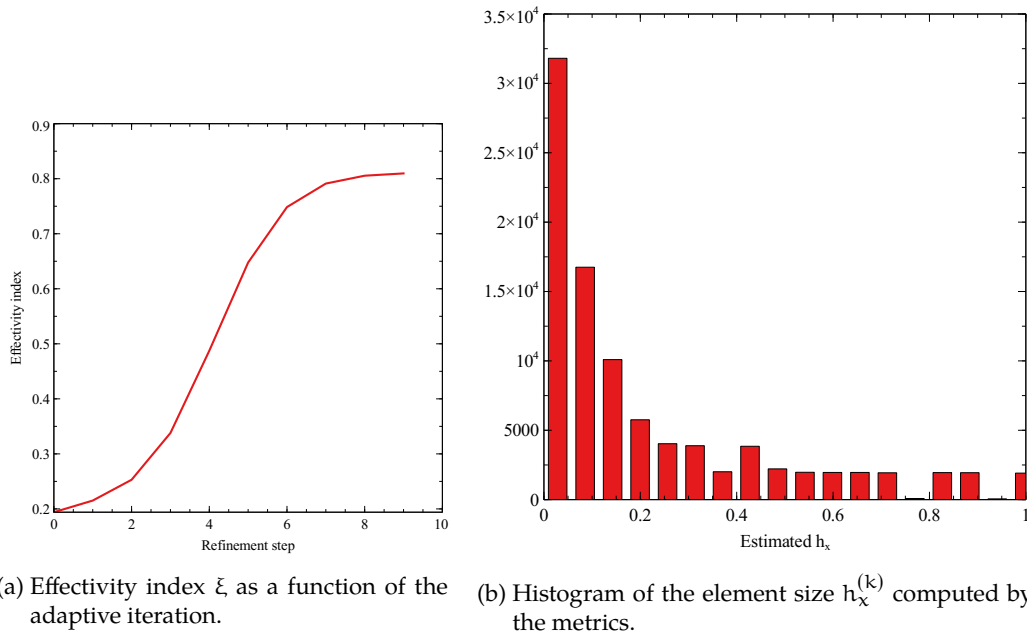
Figure 11.5.: Problem 11.1.1.1. Effectivity index and metrics histogram.

We aim to remark in particular that the metric-based approach is more effective, as it requires 2 adaptation steps to determine a mesh that is comparable, in size and thickness of the captured layers, to the one obtained by 6 iterations of the marking procedure. Moreover, the first steps of the marking approach lead to over-refine the mesh, before starting to coarsen those elements far from the layers that do not provide a significant contribution to the overall error.

11.1.2. Diffusion-reaction examples with discontinuous coefficients

11.1.2.1. Coefficient discontinuous across a Cartesian direction
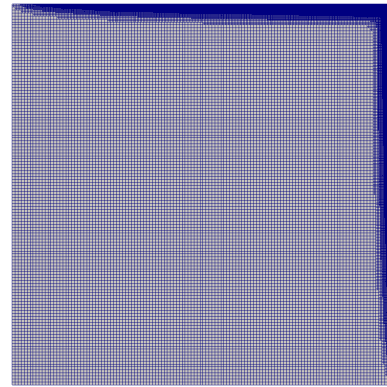
The first test case deals with a linear diffusion-reaction problem firstly proposed in [FO10], characterized by piecewise discontinuous diffusion and reaction coefficients and a strictly one-dimensional dynamics.

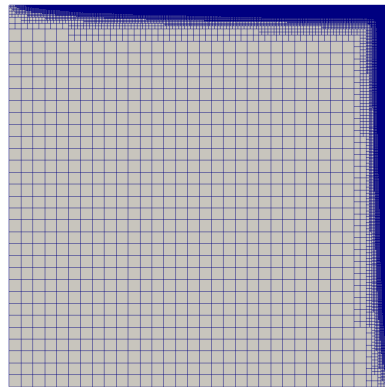Consider problem (10.1) defined over the unit square $\Omega = \Omega_h = (0,1)^2$. Denoting by
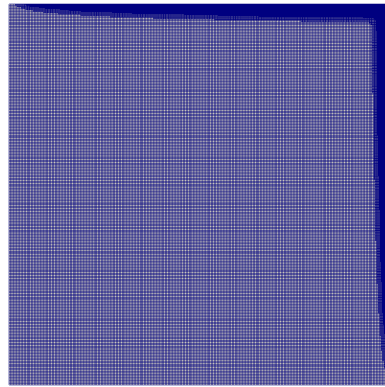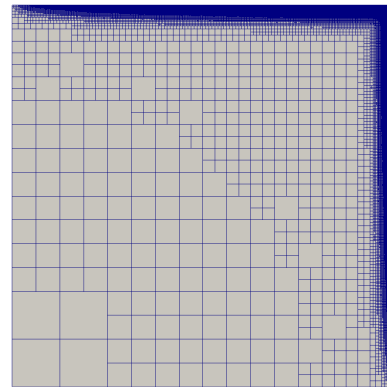
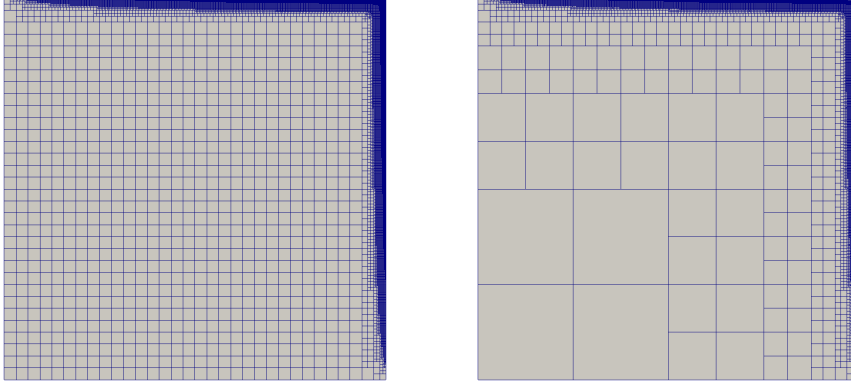(a) Mesh at adaptation step 1.

(b) Mesh at adaptation step 2.

(c) Mesh at adaptation step 4.

(d) Mesh at adaptation step 6.

Figure 11.6.: Problem 11.1.1.2. Marking-based adaptation.

(a) Mesh at adaptation step 1.   (b) Mesh at adaptation step 2.

Figure 11.7.: Problem 11.1.1.2. Metric-based adaptation.

$\Omega_1 = \{(x, y) \in \Omega : y \le 0.5\}$ and $\Omega_2 = \Omega \setminus \Omega_1$, the coefficients are given by

$$\varepsilon = \begin{cases} \varepsilon_1 = 5 \cdot 10^{-5}, & \text{in } \Omega_1, \\ \varepsilon_2 = 10^{-1}, & \text{in } \Omega_2, \end{cases} \qquad b = \begin{cases} 1, & \text{in } \Omega_1, \\ 0, & \text{in } \Omega_2, \end{cases} \qquad f = \begin{cases} 1, & \text{in } \Omega_1, \\ \varepsilon_2, & \text{in } \Omega_2. \end{cases}$$

The boundary conditions are

$$u = \begin{cases} 1, & \text{on } \{y = 0\}, \\ 0, & \text{on } \{y = 1\}. \end{cases}$$

The exact solution is given by

$$u_{\text{ex}}(x, y) = \begin{cases} 1 + 2c_1 \sinh(y/\sqrt{\varepsilon_1}), & \text{in } \Omega_1, \\ -0.5(y - 1)(y + 2c_2), & \text{in } \Omega_2, \end{cases}$$

with

$$c_1 = -\frac{7\varepsilon_2}{8\sqrt{\varepsilon_1}\cosh(0.5/\sqrt{\varepsilon_1}) + 16\varepsilon_2 \sinh(0.5/\sqrt{\varepsilon_1})},$$

$$c_2 = \frac{7\sqrt{\varepsilon_1}\cosh(0.5/\sqrt{\varepsilon_1})}{4\sqrt{\varepsilon_1}\cosh(0.5/\sqrt{\varepsilon_1}) + 8\varepsilon_2 \sinh(0.5/\sqrt{\varepsilon_1})}.$$
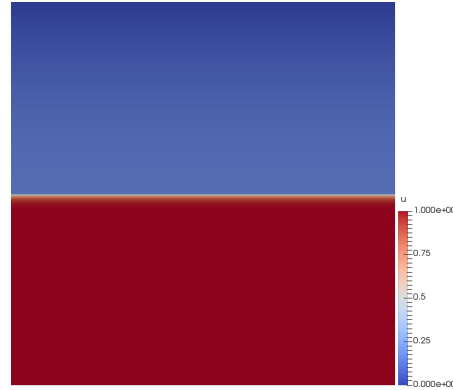
Figure 11.8.: Problem 11.1.2.1. Numerical solution.

The numerical solution and the meshes obtained using the adaptation procedure using the marking-based and the metric-based techniques are shown in figs. 11.8 to 11.10 respectively. Again, the metric-based approach is faster and more effective in determining the discontinuity interface as compared to marking algorithm.

Figure 11.11 shows the convergence of the L^2-norm and H^1-seminorm of the error associated with both the discrete solution u_h and the recovered solution u_h^* as a function of the mesh size h. A comparison between the adaptive and uniform adaptation strategies is also drawn. The same remarks as for fig. 11.4 essentially hold. The effectivity index ξ and the histogram of the element sized estimated by the metrics are shown in fig. 11.12.

11.1.2.2. Coefficient discontinuous across a circular interface

Another test case is taken from [RBI18] and is very demanding for Cartesian grids, since the diffusion coefficient here is discontinuous across a circular interface. Let $G = \{(x - 0.5)^2 + (y - 0.5)^2 \geq R^2\}$, where $R = 0.25$, and let $S = [0, 1]^2 \setminus G$. The equation to be solved is of type (10.1) with

$$\varepsilon = \begin{cases} \varepsilon_G = 1, & \text{in } G, \\ \varepsilon_S = 100, & \text{in } S, \end{cases}$$

(a) Initial mesh.

(b) Mesh at adaptation step 3.

(c) Mesh at adaptation step 5.

(d) Mesh at adaptation step 9.
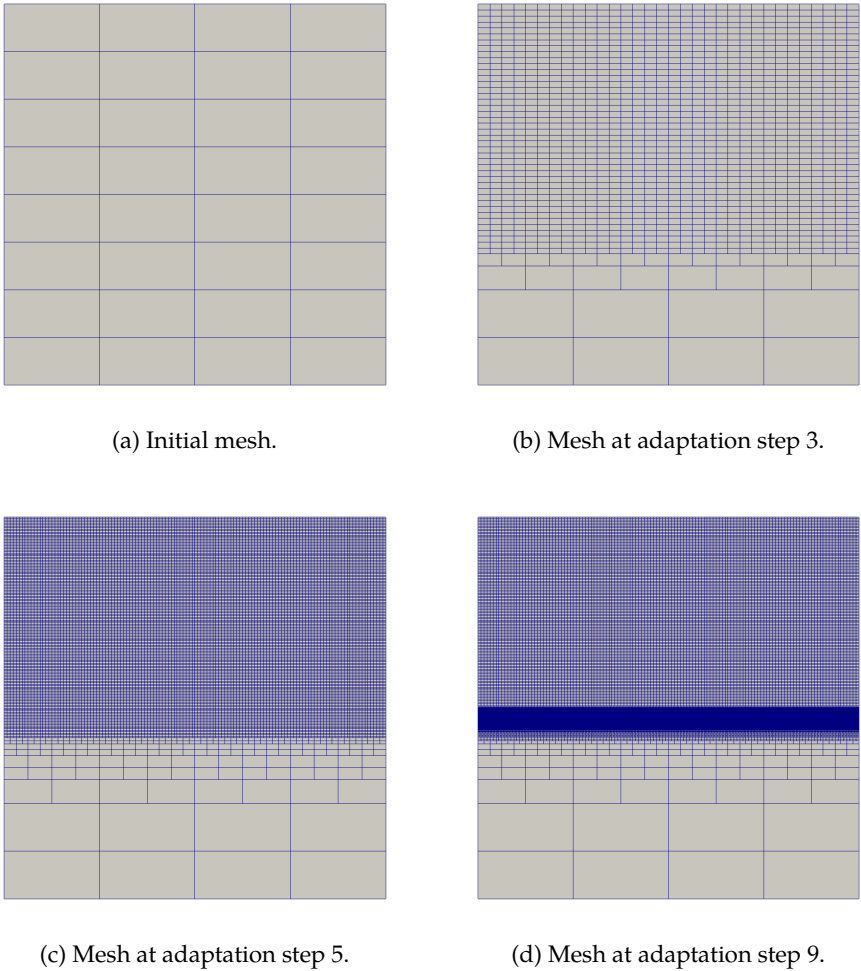
Figure 11.9.: Problem 11.1.2.1. Marking-based adaptation.

(a) Mesh at adaptation step 1.

(b) Mesh at adaptation step 3.
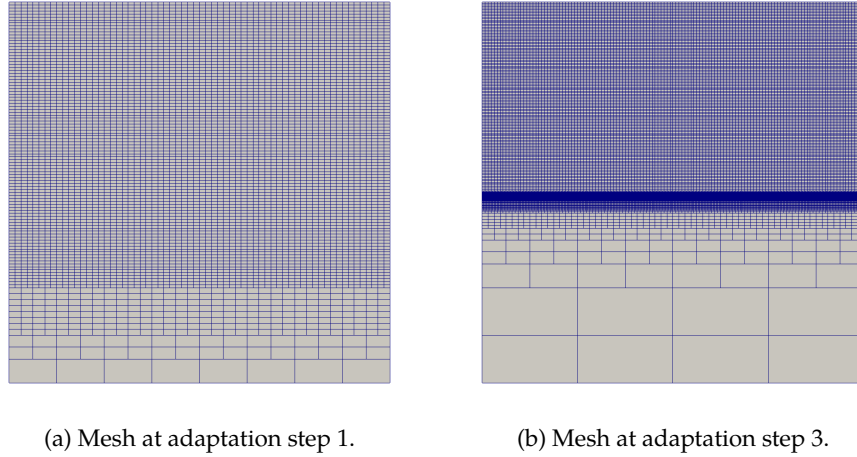
Figure 11.10.: Problem 11.1.2.1. Metric-based adaptation.

(a) Convergence of numerical errors with respect to the mesh size h.

(b) Comparison of adaptive mesh strategy vs. uniform refinement: the plot shows the error $\|u - u_h\|_{L^2(\Omega_h)}$ as a function of the number of degrees of freedom.
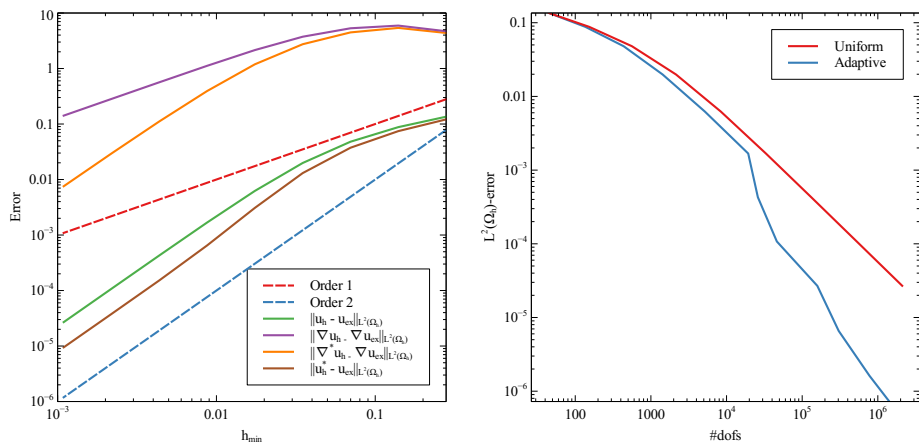
Figure 11.11.: Problem 11.1.2.1. Numerical errors and comparison of adaptive vs. uniform refinement.

(a) Effectivity index ξ as a function of the adaptive iteration.

(b) Histogram of the element size $h_x^{(k)}$ computed by the metrics.
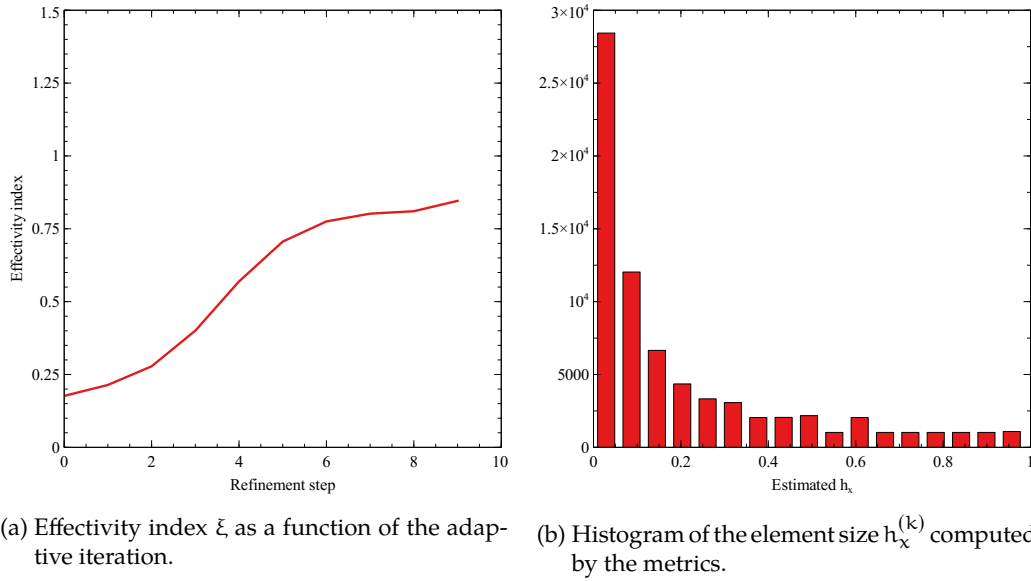
Figure 11.12.: Problem 11.1.2.1. Effectivity index and metrics histogram.

$b = 0$ and $f = 1$, whose exact solution is

$$
u_{ex}(x, y) = \begin{cases} \dfrac{1}{8} - \dfrac{1}{4\varepsilon_G} \left((x - 0.5)^2 + (y - 0.5)^2\right), & \text{in } G, \\[2ex] \dfrac{1}{8} - \dfrac{1}{4\varepsilon_S} \left((x - 0.5)^2 + (y - 0.5)^2\right) - \dfrac{R^2}{4} \left(1 - \dfrac{1}{\varepsilon_S}\right), & \text{in } S, \end{cases}
$$

By imposing a tolerance of 10^{-4} for the error estimator, we ended up with a final mesh with maximum level of refinement equal to 10, as shown in fig. 11.13. The results obtained in terms of L^2-error are summarized in table 11.1. As compared to Ref. [RBI18], for a given maximum level of refinement and mesh cardinality allowed, the error provided using our method is significantly smaller. Indeed, the mesh generated by our adaptation procedure is uniformly refined with level 10 in the whole region G, which suggests that not only the interface contributes to the overall error, but also those regions – possibly far from the interface – where the solution is apparently smooth, due to the error propagation. An estimator-driven approach is able to capture this information independently on the geometrical setting. This is an advantage with respect to geometry-based methods for mesh adaptation, as the one presented in [RBI18], that

143

(a) Final mesh.

(b) Zoom at the interface, colored based on the refinement level.
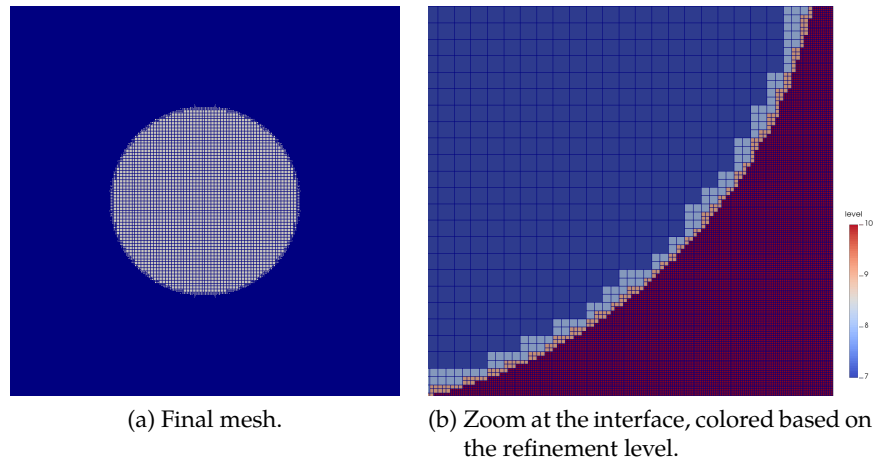
Figure 11.13.: Problem 11.1.2.2. Resulting adapted mesh.

can provide a more locally-refined mesh at geometrical interfaces but is not able to capture the error distribution across all the mesh elements.

11.1.3. Diffusion-advection example with constant advection coefficient skew w.r.t. Cartesian axes

Here we study a test proposed in [BH82]. It has the form of problem (10.2) on $\Omega = (0, 1)^2$ with $\varepsilon = 10^{-6}$, $\boldsymbol{\beta} = [\cos(\vartheta), \sin(\vartheta)]^{\mathsf{T}}/\varepsilon$, $f = 0$. The boundary conditions are imposed as

Step	n. of nodes	h_{min}	L^2-error
0	81	0.176777	$2.82441 \cdot 10^{-3}$
1	289	0.0883883	$6.82165 \cdot 10^{-4}$
2	1033	0.0441942	$1.83441 \cdot 10^{-4}$
3	3829	0.0220971	$5.33397 \cdot 10^{-5}$
4	14245	0.0110485	$3.05214 \cdot 10^{-5}$
5	55149	0.00552427	$1.16476 \cdot 10^{-5}$
6	215321	0.00276214	$4.59463 \cdot 10^{-6}$
7	853511	0.00138107	$2.98502 \cdot 10^{-6}$

Table 11.1.: Mesh cardinality, h_{min} and L^2-error during the refinement procedure.
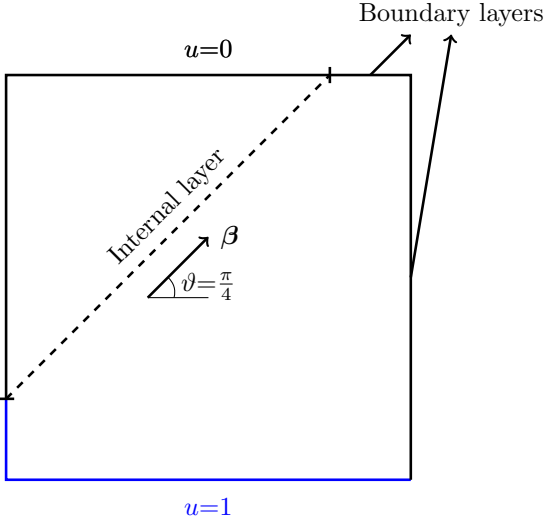
(a) Geometrical setting.
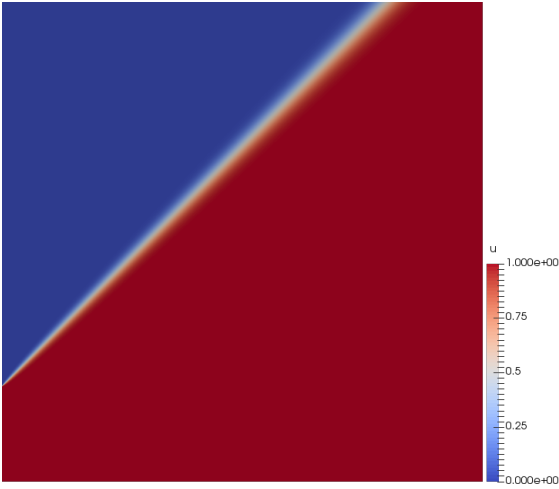
(b) Numerical solution.

Figure 11.14.: Problem 11.1.3. Geometrical setting and numerical solution.

shown in fig. 11.14a, *i.e.*

$$u(x, y) = \begin{cases} 1, & \text{on } \Gamma = \{x = 0, 0 \leq y \leq 0.2\} \cup \{y = 0\}, \\ 0, & \text{on } \partial\Omega \setminus \Gamma. \end{cases}$$

The numerical solution and the meshes obtained with the adaptation procedure using the metric-based techniques are shown in figs. 11.14 and 11.15 respectively.

We also compare the results with those in [Sch+12], relying on a gradient-based adaptation: first, the authors compute the integral average of the solution gradient at each mesh element:

$$\gamma_k = \frac{\|\nabla u_h\|_{L^2(\Omega^{(k)})}}{\left|\Omega^{(k)}\right|}. \tag{11.1}$$

Then, the elements are marked for adaptation or coarsening depending on the following conditions:

$$\gamma_k \geq \frac{c_1}{N_{el}} \sum_{k=1}^{N_{el}} \gamma_k, \qquad \gamma_k \leq \frac{c_2}{N_{el}} \sum_{k=1}^{N_{el}} \gamma_k,$$

respectively, where c_1, c_2 are empirically set tuning parameters. The results obtained through this procedure are shown in fig. 11.16. The mesh obtained is fully comparable with the one in fig. 11.15, which is remarkable taking into account that the estimator based on eq. (11.1) is specifically set to detect steep gradients.

Finally the histogram of the element sizes estimated by the metrics in fig. 11.17 shows a distribution that is concentrated at a specific value, so that most elements have a small size and are distributed in a very narrow region of the domain corresponding to the boundary discontinuities and the boundary and interior layers.

11.2. Weak scaling test

The performance of the numerical code implemented in `bim++` was tested on a Poisson equation with a discontinuous diffusion coefficient. The unit square is firstly meshed and then hierarchically refined based on an *a priori* criterion, namely marking those quadrants intersecting a specified arbitrary set of segments corresponding to the coefficient discontinuities. Then the resulting linear system is assembled and solved using the parallel sparse linear solver `MUMPS`[1].

The time needed for creating, refining the mesh, assembling the discrete operators and assigning the boundary conditions was computed for different runs of the same

---

[1] `http://mumps.enseeiht.fr/`

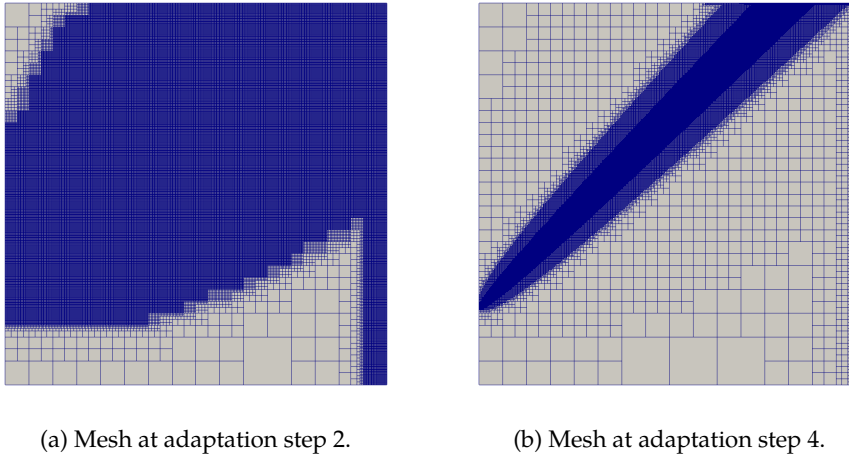| (a) Mesh at adaptation step 2. | (b) Mesh at adaptation step 4. |

Figure 11.15.: Problem 11.1.3. Metric-based adaptation.

problem with varying numbers of processors. Then, the speedup associated with the *weak scaling* for n Central Processing Units (CPUs) was determined as

$$s(n) = \frac{\text{time(1 CPU)}}{\text{time}(n \text{ CPUs})}.$$

The resulting speedup, compared to the desirable linear one, is shown in fig. 11.18, confirming that attaining an extremely scalable user-friendly software is possible if using proper data structures and algorithms, as enabled by quadtrees, together with advanced HPC techniques relying on low-level calls for parallel communication.
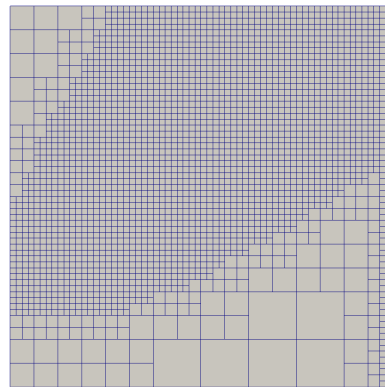
11.3. Time-dependent quadtree adaptation

The adaptation procedure described in section 10.4 was applied to a time-dependent framework to simulate the following problem, consisting of a diffusion-advection equation for a solute concentration n in a parallel plate flow [FDS09], coupled with a Poisson equation describing the potential φ corresponding to the advection field to recall the same structure as the DD system. The equations, solved in the rectangle
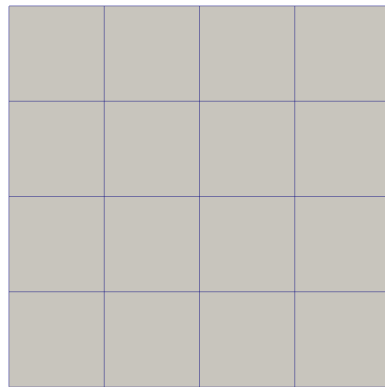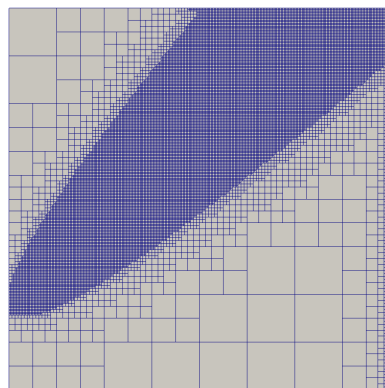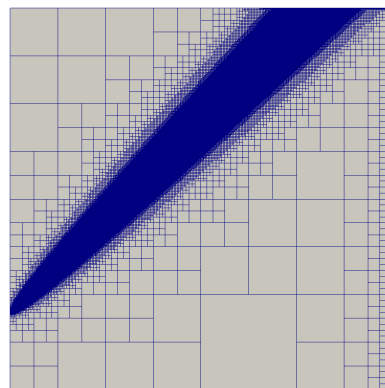
(a) Initial mesh.

(b) Mesh at adaptation step 4.

(c) Mesh at adaptation step 6.

(d) Mesh at adaptation step 10.

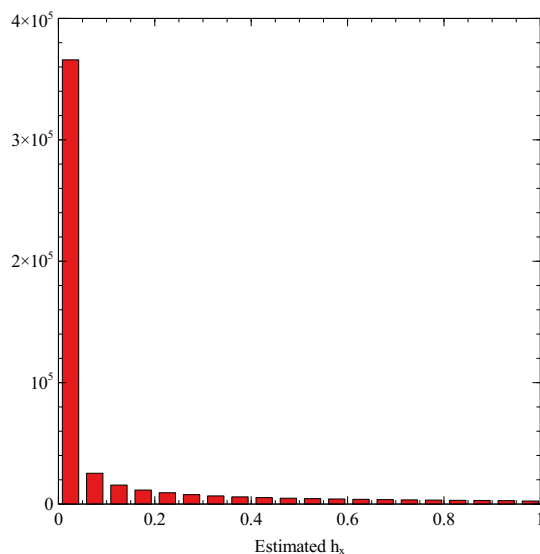Figure 11.16.: Problem 11.1.3. Gradient-based adaptation.

Figure 11.17.: Problem 11.1.3. Histogram of the element size $h_x^{(k)}$ estimated by the metrics.

$\Omega = (-5, 30) \times (0, 0.1)$ and over the timespan $(0, 4]$, read

$$\begin{cases} -\nabla \cdot (\nabla \varphi) = 0, \\ \dfrac{\partial n}{\partial t} - \nabla \cdot (\nabla n - n \nabla \varphi) = 0, \end{cases} \tag{11.2}$$

with initial datum given by

$$\begin{cases} \varphi(\boldsymbol{x}, 0) = 5(x_1 + 5) - 20 x_2, \\ n(\boldsymbol{x}, 0) = \dfrac{1}{2} \exp\left(-\dfrac{x_1^2}{2}\right), \end{cases}$$

so that the advection field is $\nabla \varphi (\boldsymbol{x}, t) = [5, -20]^\mathsf{T}$.

The problem was solved following the same time, space discretization and linearization strategies presented in part III and the mesh was adapted at the beginning of every time step according to the extrapolated initial guess.

The initial guess and mesh are shown in fig. 11.19, while the propagating wave and the corresponding adapted meshes across the simulated timespan are displayed in

149
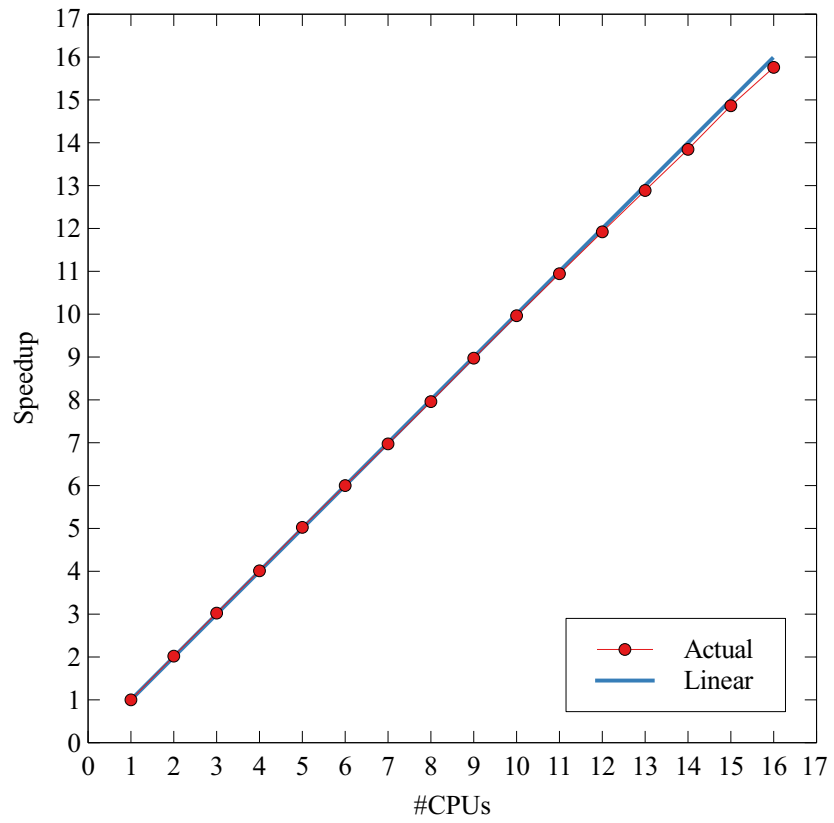
Figure 11.18.: Problem 11.2. Actual vs. theoretical speedup.

(a) Initial guess n at time t = 0.

(b) Initial mesh at time t = 0.

Figure 11.19.: Problem 11.3. Initial guess n and mesh.

fig. 11.20: the adaptation procedure is able to generate meshes that automatically follow the propagating front and detect error-prone regions so that, given a desired accuracy, the overall computational costs are reduced with respect to the uniform mesh case.
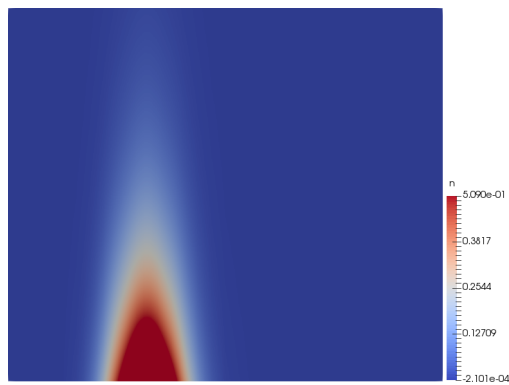
(a) Solution n at time t = 1.25.
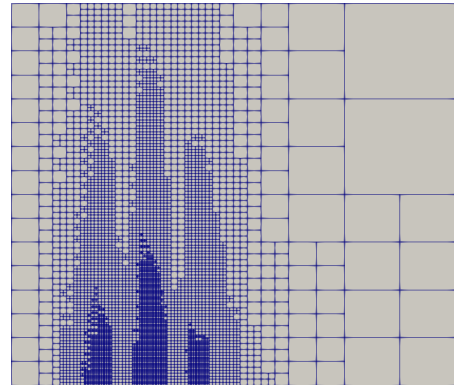
(b) Adapted mesh at time t = 1.25.
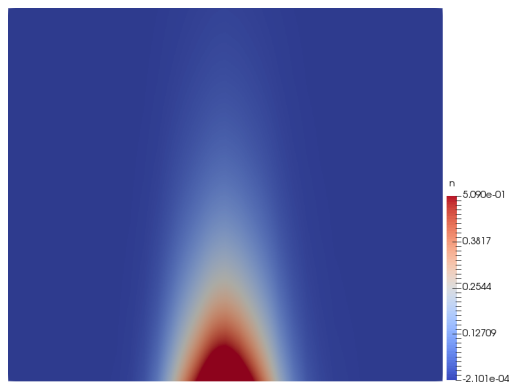
(c) Solution n at time t = 2.5.
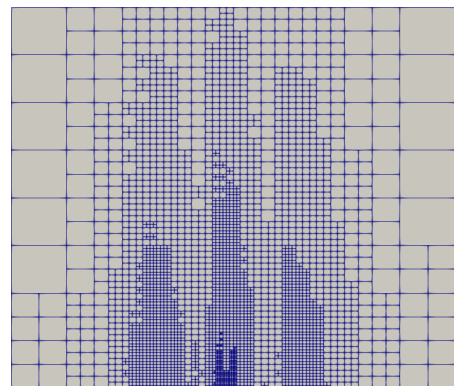
(d) Adapted mesh at time t = 2.5.
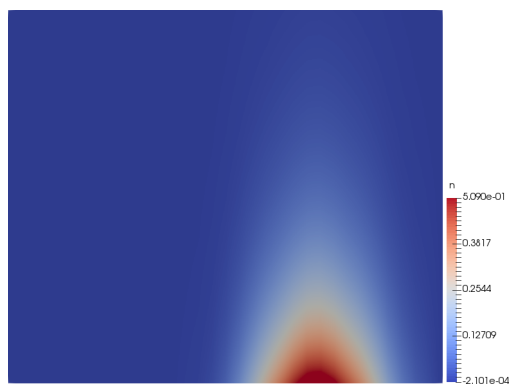
(e) Solution n at time t = 4.
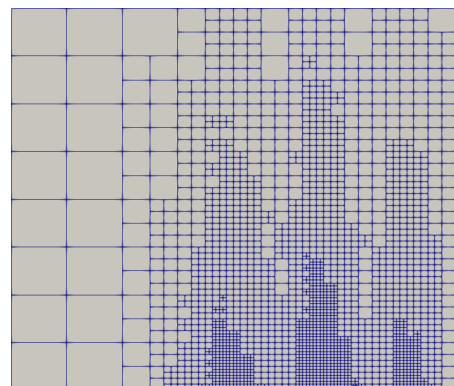
(f) Adapted mesh at time t = 4.

Figure 11.20.: Problem 11.3. Solution n and adapted meshes computed at different time steps.

12. Consistent formulation

In this chapter we present the results of the application of the thermodynamic consistent discrete formulation presented in section 6.1.1 to the solution of a DD-like system to the propagation of charge packets in semiconductor characterized by different DOS shapes.

We aim at solving the following equations:

$$
\begin{cases}
-\nabla \cdot (\varepsilon \nabla \varphi) + qn = 0, & \text{in } \Omega, \\[2mm]
\dfrac{\partial n}{\partial t} - \dfrac{1}{q} \nabla \cdot \mathbf{J}_n = 0, & \text{in } \Omega, \\[2mm]
\mathbf{J}_n = q\mu_n n \nabla \varphi_n = -qV_{th}\mu_n \left(\nabla n - n\nabla \left(\dfrac{\varphi + \psi}{V_{th}} \right) \right), \\[2mm]
n - \mathcal{N} \left(V_{th} \log \left(\dfrac{n}{N_0} \right) - \psi \right) = 0, & \text{in } \Omega,
\end{cases}
\tag{12.1}
$$

over a rectangular domain Ω for different choices for the DOS function $\mathcal{N}$.

We focus on DOS shapes, parametrized on α and σ, that are a generalization of the Gaussian case described in section 5.4:

$$
n = \frac{N_0}{K\sigma} \int_{-\infty}^{\infty} \frac{\exp\left(-\left| \dfrac{\mathcal{E} - \mathcal{E}_{\mathrm{LUMO}}}{\Lambda \, \sigma} \right|^{\alpha} \right)}{1 + \exp\left(\dfrac{\mathcal{E}_{\mathrm{LUMO}} - \mathcal{E}_F}{k_B T} \right)} \, d\mathcal{E}.
\tag{12.2}
$$

The quantities $K = K(\alpha, \sigma)$ and $\Lambda = \Lambda(\alpha, \sigma)$ are computed in such a way that

$$
\frac{1}{K\sigma} \int_{-\infty}^{\infty} \exp\left(-\left| \frac{\mathcal{E} - \mathcal{E}_{\mathrm{LUMO}}}{\Lambda \, \sigma} \right|^{\alpha} \right) d\mathcal{E} = 1
$$

and

$$
\frac{1}{K\sigma} \int_{-\infty}^{\infty} (\mathcal{E} - \mathcal{E}_{\mathrm{LUMO}})^2 \exp\left(-\left| \frac{\mathcal{E} - \mathcal{E}_{\mathrm{LUMO}}}{\Lambda \, \sigma} \right|^{\alpha} \right) d\mathcal{E} = \sigma^2,
$$

which leads to

$$K = 2\Lambda\,\Gamma\left(1 + \frac{1}{\alpha}\right)$$

and

$$\Lambda = \sqrt{\frac{3\,\Gamma\left(1 + \dfrac{1}{\alpha}\right)}{\Gamma\left(\dfrac{3 + \alpha}{\alpha}\right)}},$$

where

$$\Gamma(z) = \int_0^\infty t^{z-1}\exp(-t)\,dt.$$

In order to numerically compute the integral in eq. (12.2), it is convenient to apply the change of the integration variable

$$\eta = \frac{\mathcal{E} - \mathcal{E}_{\mathrm{LUMO}}}{\Lambda\sigma} = \frac{-q(\varphi - \varphi_n)}{\Lambda\sigma} = \frac{-q\phi}{\Lambda\sigma},$$

where we have used eq. (5.10) and (5.13), and rewrite it as

$$n(\phi) = \frac{N_0\Lambda}{K}\int_0^\infty \exp(-\eta)\exp\left(\eta - \eta^\alpha\right)\cdot$$

$$\cdot\left(\frac{1}{1 + \exp\left(\Lambda\eta\hat{\sigma} - \dfrac{\phi}{V_{\mathrm{th}}}\right)} + \frac{1}{1 + \exp\left(-\Lambda\eta\hat{\sigma} - \dfrac{\phi}{V_{\mathrm{th}}}\right)}\right)d\eta, \tag{12.3}$$

where $\hat{\sigma} = \sigma/k_B T$, that can be approximated by means of Gauss-Laguerre quadrature formulas.

Notice that, although the density of states function may not be differentiable for every value of α, the charge density n in eq. (12.3) has a continuous derivative with respect to

(a) $n(\phi)$. (b) $dn/d\phi(\phi)$.
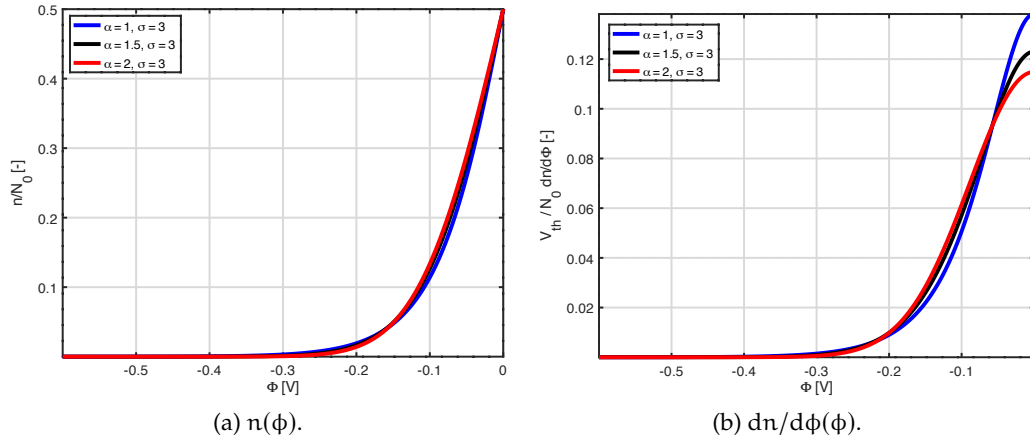
Figure 12.1.: Electron density and derivative for $\hat{\sigma} = 3$ and different values of α.

ϕ which can be expressed as

$$\frac{\partial n}{\partial \phi}(\phi) = \frac{N_0 \Lambda}{K V_{th}} \int_0^\infty \exp(-\eta) \exp\left(\eta - \eta^\alpha\right) \cdot$$

$$\cdot \left(\frac{1}{\left[\exp\left(\frac{1}{2}\left(-\Lambda\eta\hat{\sigma} + \frac{\phi}{V_{th}}\right)\right) + \exp\left(\frac{1}{2}\left(\Lambda\eta\hat{\sigma} - \frac{\phi}{V_{th}}\right)\right)\right]^2} + \frac{1}{\left[\exp\left(\frac{1}{2}\left(\Lambda\eta\hat{\sigma} + \frac{\phi}{V_{th}}\right)\right) + \exp\left(\frac{1}{2}\left(-\Lambda\eta\hat{\sigma} - \frac{\phi}{V_{th}}\right)\right)\right]^2} \right) d\eta.$$

Figure 12.1 and 12.2 show the quantities $n(\varphi - \varphi_n)$ and its derivative $dn/d\phi$ as a function of α and for $\hat{\sigma} = 3$ and $\hat{\sigma} = 8$, respectively. The diffusion enhancement factor $g_D(n)$, defined as in eq. (5.17), and the enhancement potential ψ are shown in figs. 12.3 and 12.4, respectively.

Equation (12.1) has been simulated with a Gaussian initial guess for n for different values of

The resulting n and ψ for $\alpha = 1, 2$ and $\hat{\sigma} = 3.5, 6$ at different time steps are shown in fig. 12.5, fig. 12.6, fig. 12.7, respectively.

(a) $n(\phi)$.
(b) $dn/d\phi(\phi)$.
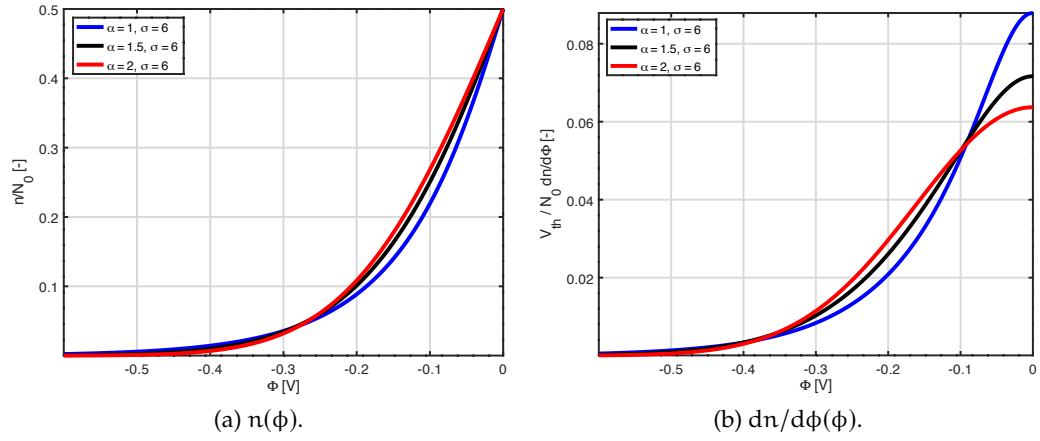
Figure 12.2.: Electron density and derivative for $\hat{\sigma} = 6$ and different values of α.

(a) $\hat{\sigma} = 3$.
(b) $\hat{\sigma} = 6$.
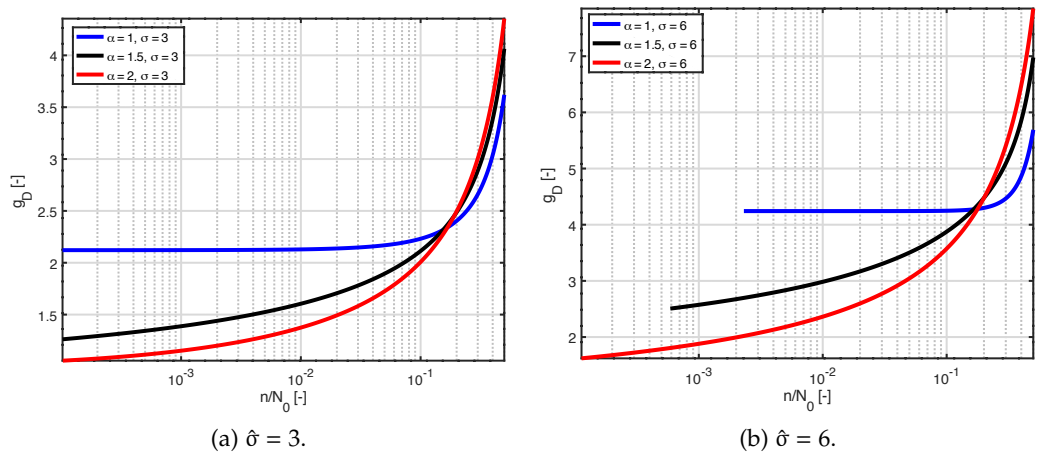
Figure 12.3.: Diffusion enhancement as a function of α.

(a) $\hat{\sigma} = 3$.

(b) $\hat{\sigma} = 8$.
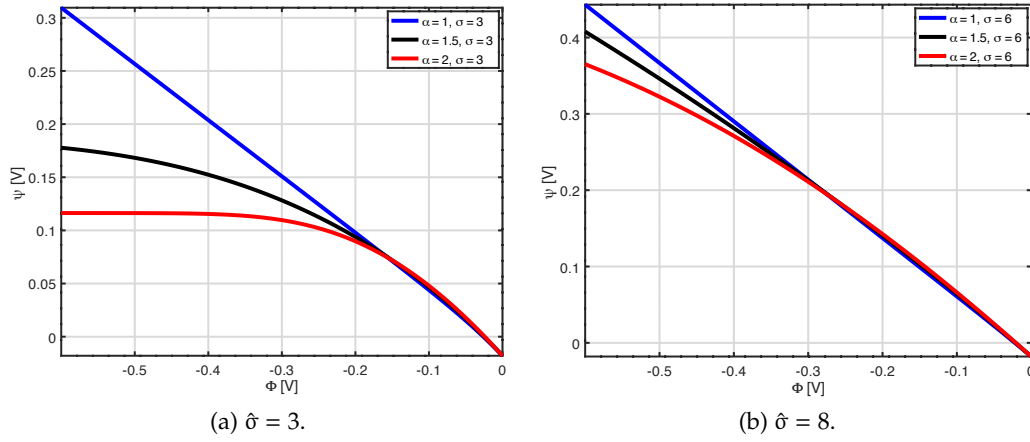
Figure 12.4.: Enhancement potential as a function of α.

All the results show that the enhancement factor g_D not only depends on φ, φ_n and n, but also from the shape of the considered DOS distribution through the parameters α and σ. Therefore, the choice for the function $\mathcal{N}$ strongly affects the properties of charge transport in semiconductors. In particular, results of simulations of charge transport, such as computing the mobility and the diffusivity coefficients, can be exploited to determine the corresponding DOS shape associated with the molecular properties of the material considered, as discussed for example in [OHB12].

(a) $\alpha = 1$, $\hat{\sigma} = 3.5$

(b) $\alpha = 1$, $\hat{\sigma} = 6$

(c) $\alpha = 2$, $\hat{\sigma} = 3.5$

(d) $\alpha = 2$, $\hat{\sigma} = 6$
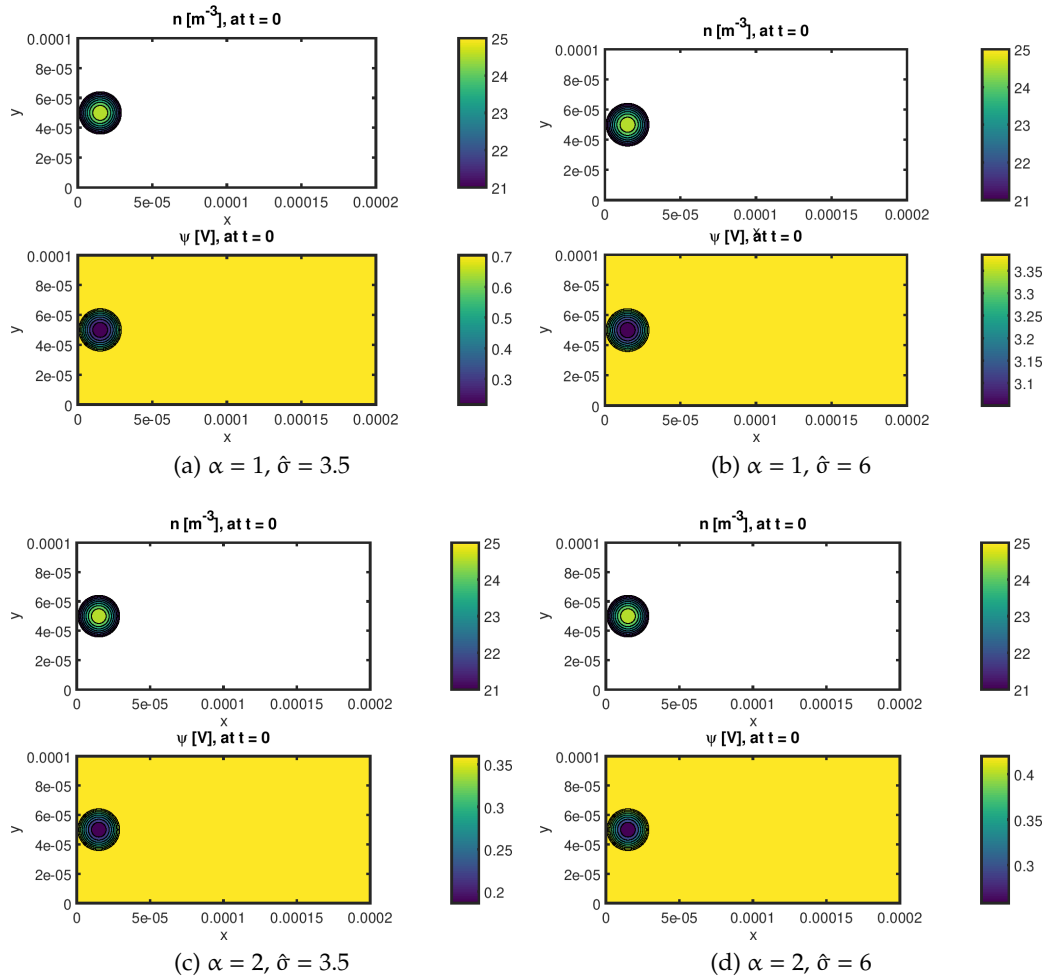
Figure 12.5.: Problem 12. Solution n and ψ at $t = 0$.
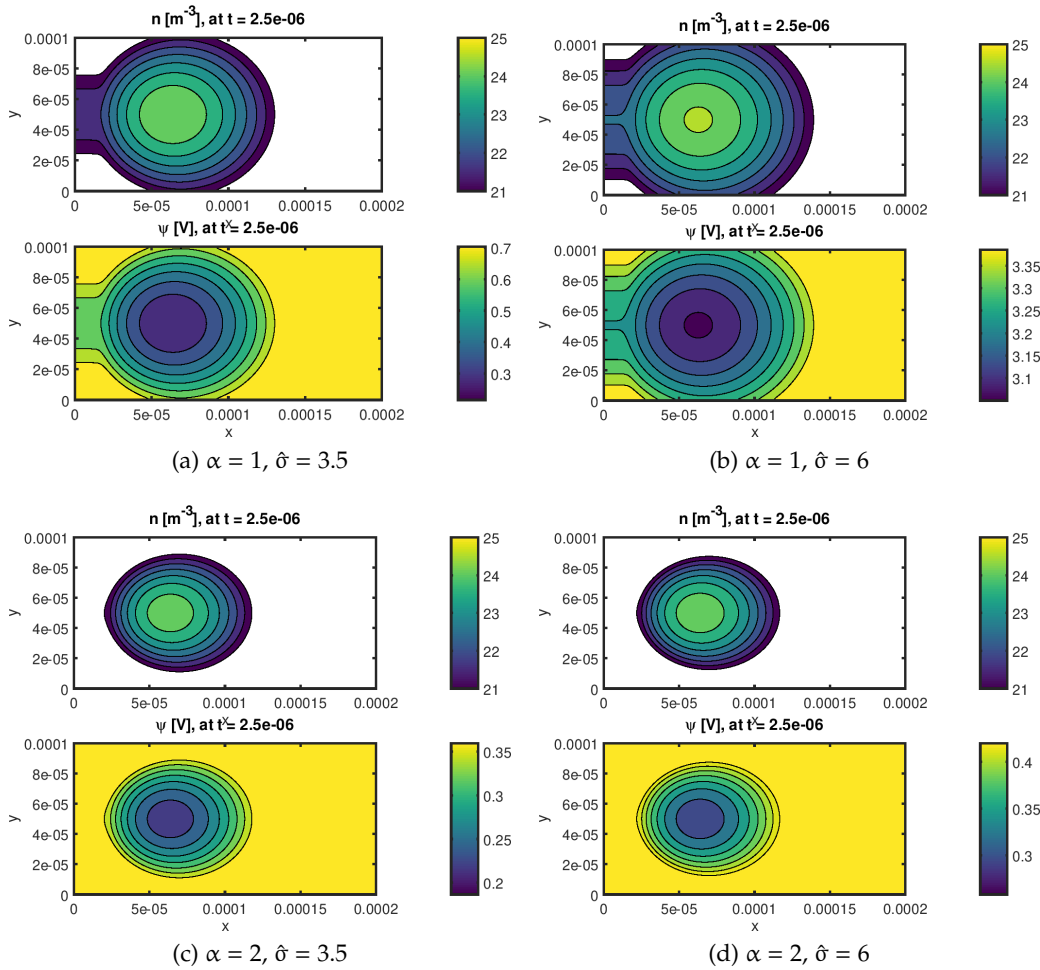
Figure 12.6.: Problem 12. Solution n and ψ at $t = 2.5 \cdot 10^{-6}$.
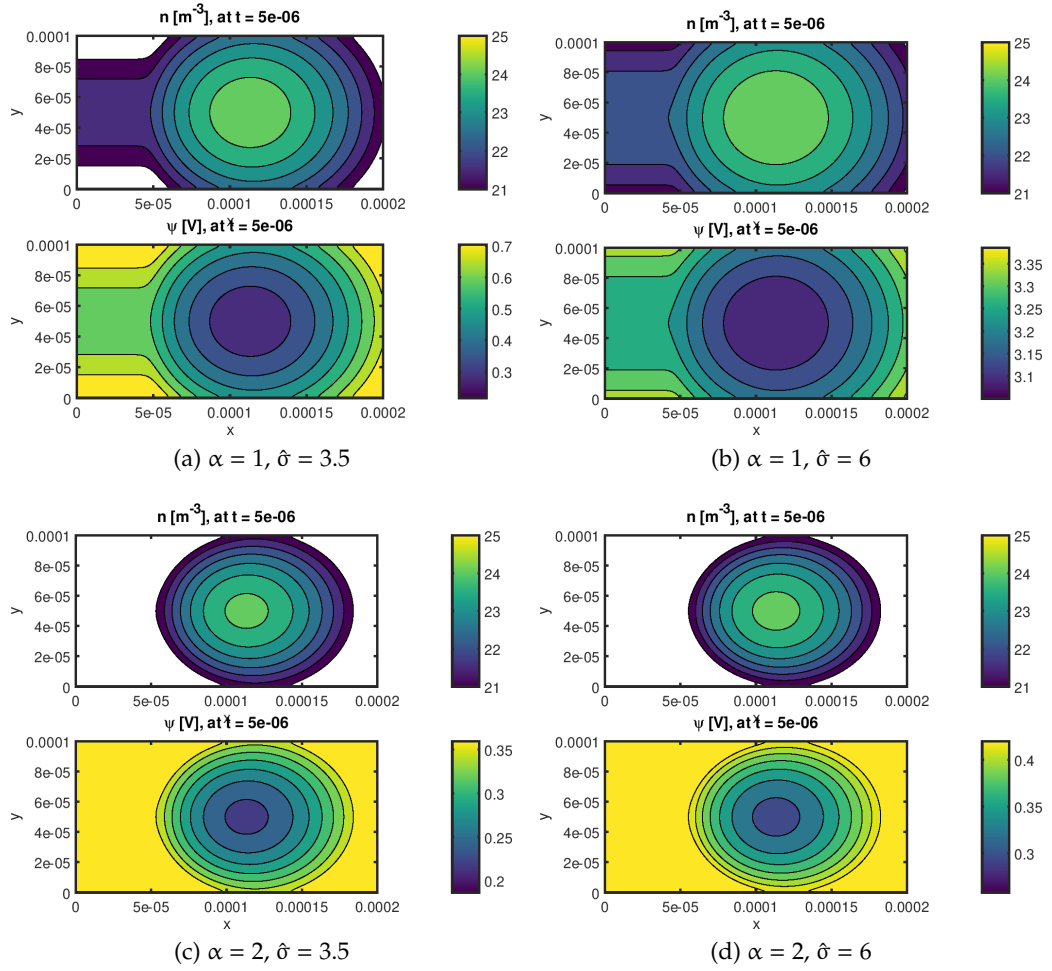
Figure 12.7.: Problem 12. Solution n and ψ at $t = 5 \cdot 10^{-6}$.

13. Parameter estimation in organic semiconductor devices

The results presented in this chapter are the main subject of [Afr+17].

Despite the technological progress in the field of organic electronics, many fundamental questions are still debated and there is a strong need for simple yet reliable approaches to extract physical parameters from experimental measurements [Vri+13b].

The predictive accuracy of state-of-the-art continuum models for charge transport in organic semiconductors is highly dependent on the accurate tuning of a set of parameters whose values cannot be effectively estimated either by direct measurements or by first principles. Fitting the complete set of model parameters at once to experimental data requires to set up extremely complex multi-objective optimization problems whose solution is, on the one hand, overwhelmingly computationally expensive, and on the other it provides no guarantee of the physical soundness for the value obtained for each individual parameter. In [Afr+17] we presented a step-by-step procedure that enables to determine the most relevant model parameters, namely the density of states width, the carrier mobility and the injection barrier height by fitting experimental data from a sequence of relatively simple and inexpensive measurements to suitably devised numerical simulations. At each step of the proposed procedure only one parameter value is sought for, thus highly simplifying the numerical fitting and enhancing its robustness, reliability and accuracy. As a case study we consider a prototypical n-type organic polymer in section 13.1 and a p-type polymer in section 13.2. Very satisfactory fittings of experimental measurements are obtained, and physically meaningful values for the aforementioned parameters are extracted.

13.1. P(NDI2OD-T2)

13.1.1. Introduction

In [Mad+15] the authors showed that, by fitting CV measurements of MIS capacitors, it is possible to extract the width of the DOS – assuming it is a superposition of Gaussian functions – exploiting the sensitivity of CV curves to the semiconductor disorder degree
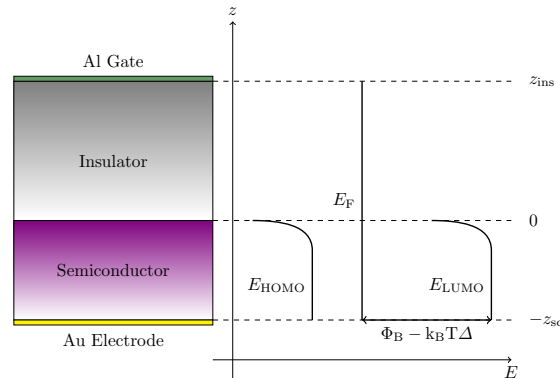
Figure 13.1.: One-dimensional schematic of the MIS capacitor used for the analysis and related energy levels.

[Sun+16]. By operating MIS capacitors at suitably low frequency, quasi-equilibrium is ensured which implies that simulations can be performed in the static regime and that phenomena specifically related to carrier transport are negligible in order to fit experimental measurements, which leads to advantages in terms of both computational cost and accuracy. In addition, the DOS extraction is disentangled from carrier transport properties, which makes the fitting procedure substantially simpler and more robust.

If a DOS consisting of a single Gaussian provides a reasonable fit, the carrier mobility can be predicted in the framework of the EGDM [Coe+05], and used to successfully fit the transfer characteristic curves of OTFTs in the linear regime. The schematic of the simulated and measured MIS capacitor is depicted in fig. 13.1.

The extraction of the DOS width requires the accurate knowledge of the device geometrical dimensions, of the insulator and semiconductor permittivities, of the total density of available states and, most notably, of the Φ_B between the bottom metal and the semiconductor. The latter parameter is the one that suffers from the highest level of uncertainty: indeed, metal-semiconductor interfaces are still a subject of debate in the scientific community [OKH14]; due to the various phenomena which may be involved (pillow effect, interface dipoles, charge transfer, chemisorption) the prediction of Φ_B is a hard task, and its measurement requires very dedicated equipment such as XPS/UPS [Koc07] or Kelvin Probe [BSF09; BSF02; Bür+03].

The uncertainty in Φ_B results in an uncertainty in determining the DOS width, as shown in [Mad+15] and reported in fig. 13.2: for each value of Φ_B a value for the DOS width can be fitted. Unfortunately, the fittings obtained by varying Φ_B are all of comparable quality. The uncertainty is not negligible indeed: by varying Φ_B from 1 [eV]
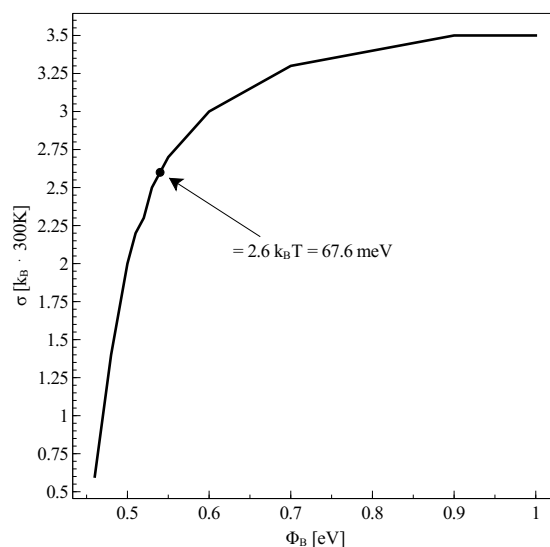
Figure 13.2.: P(NDI2OD-T2). Dependence of the fitted Gaussian DOS width σ on the injection barrier Φ_B. The dot on the curve identifies the σ value that simultaneously yields in the best fitting of OTFT transfer characteristic curves and of MIS capacitor Capacitance-Frequency (CF) curves. Experimental data are taken from [Mad+15] and refer to MIS capacitors based on the prototypical n-type polymer Poly{[N,N'-bis(2-octyldodecyl)-naphthalene-1,4,5,8-bis(dicarboximide)-2,6-diyl]-alt-5,5'-(2,2'-bithiophene)} (P(NDI2OD-T2)).

down to 0.5 [eV], the DOS width reduces from about 3.5 [k_BT] down to about 0.5 [k_BT], which appears to be a rather unphysical value.

In the present work we demonstrate that this uncertainty can be drastically reduced by cooperatively exploiting MIS CV curves, MIS CF curves and OTFT transfer characteristic curves in the linear regime. To this end, we have simulated out-of-equilibrium conditions in the framework of the DD scheme. This enabled us to simulate the whole CF curve of the MIS capacitor. In addition, in the modeling and fitting of OTFT transfer characteristic curves we have taken into account the contact resistance in the context of the current crowding regime [NC12; Jun+08].

As a case study we choose as in [Mad+15]. P(NDI2OD-T2), a printable, prototypical n-type polymer with a high mobility, exceeding 1 $\left[\text{cm}^2\text{V}^{-1}\text{s}^{-1}\right]$ when processed from suitable pre-aggregating solvents [Buc+15; Yan+09]. We find that the best fit to CV, CF and OTFT curves is obtained by assuming a Gaussian DOS width of 2.6 [k_BT] and a

barrier for electron injection from gold contacts of 0.54 [eV]. As to the former, the DOS width turns out to be slightly (13%) smaller than the former prediction in [Mad+15]. As to the latter, Φ_B is considerably smaller than the nominal barrier, which is as large as 1 [eV] assuming that the LUMO lies at 4.0 [eV] and that the gold Fermi level lies at around 5 [eV]. The origin of such a small value for the barrier, which has already been postulated in other studies, is discussed.

13.1.2. Results and discussion

By fitting CV experimental data and assuming the nominal 1 [eV] barrier, we extract $\sigma = 3.5\,k_BT$ (fig. 13.2). We note that this value is slightly (about 15%) larger than what reported previously [Mad+15]. The difference can be ascribed to the more accurate modeling of the metal-semiconductor interface used in the present study, which accounts for the Schottky barrier lowering effect as previously discussed in section 5.6.1. But by fitting OTFT IV characteristics (see section 13.1.4.3) we obtain $\mu_{0,n} \simeq 33\,[\text{cm}^2\text{V}^{-1}\text{s}^{-1}]$ (fig. 13.3), which is a completely unphysical value for P(NDI2OD-T2), whose low-field, low-density mobility should be around $10^{-1} \div 10^{-2}\,[\text{cm}^2\text{V}^{-1}\text{s}^{-1}]$. The large difference with respect to [Mad+15] arises because the OTFT fitting takes into account the effect of R_C in the framework of the current crowding model [NC12; Jun+08]. Also the contact resistance value extracted, in the range of hundreds of [$k\Omega\,\text{cm}$], is in contrast to the literature value of tens of [$k\Omega\,\text{cm}$] for P(NDI2OD-T2) transistors with gold contacts [Cai+10]. With such a large barrier, contacts are poorly injecting: to compensate this phenomenon and to fit the experimental OTFT transfer characteristic curves the algorithm has to admit an exceedingly high value for $\mu_{0,n}$. Nonetheless, the transistor is severely contact limited and the fitting very bad (see fig. 13.4). The nominal barrier leads to results in contrast with experimental measurements also in the simulation of the CF curve of the MIS capacitor. Results are reported in fig. 13.5 together with the experimental curve. The simulated curve shows a low frequency region and a high frequency region, separated by a transition region. In the former frequency region the MIS capacitor operates in the quasi-equilibrium regime; it does not appear as a plateau because with Poly(methyl methacrylate) (PMMA) dielectric ε_{ins} is frequency-dependent (in fact by simulating a CF curve with a constant ε_{ins} at low frequency a flat curve would be obtained, see fig. 13.6). A neater information can be gained by looking at the phase of the carrier density at the semiconductor-insulator interface, reported in fig. 13.7 (its modulus is shown in fig. 13.8): at low frequency the phase is 0, implying that the accumulated channel is able to follow the modulation imposed by the small sinusoidal signal on the gate; but when the frequency raises, a local minimum occurs in $\angle n(0)$, followed by a strong decrease, indicating that the channel lags behind the sinusoidal
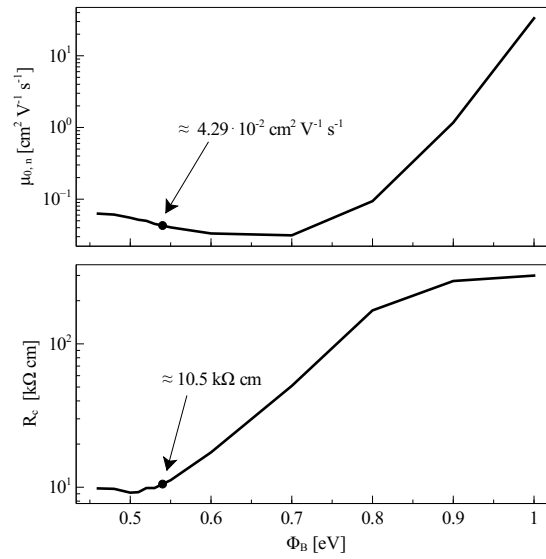
Figure 13.3.: P(NDI2OD-T2). Low-field, low-density mobility $\mu_{0,n}$ (top) and contact resistance R_C (at $V_{gate} = +35\,[V]$, bottom), for different values of the injection barrier Φ_B. The dots on the curves identify the Φ_B value that simultaneously yields in the best fitting of OTFT transfer characteristic curves and of MIS capacitor CF curves.

modulation.

We choose the CF curve inflection point as the demarcation frequency between the quasi-equilibrium and the out-of-equilibrium regions (see inset of fig. 13.5). With a barrier of 1 [eV] the simulated curve does not reproduce the experimental one: the former has an inflection point of about 10 [kHz], the latter an inflection point that, albeit not clearly resolved in the measurement, is for sure in excess of 100 [kHz].

It is consequently clear that the nominal barrier does not produce consistent results either in terms of OTFT contact resistance or in terms of MIS capacitor CF curves, and that the real Au-P(NDI2OD-T2) interface has to be indeed more effective in injecting charge carriers.

We then tried to reduce Φ_B. For each value of Φ_B, a value of σ is extracted by fitting CV curves; related values for $\mu_{0,n}$ and for the R_C are obtained from OTFT measurements and a new CF curve is simulated. The extracted DOS width is an increasing function of Φ_B. In fact, the smaller the barrier, the larger the concentration of carriers at the metal-semiconductor interface. The population of thermal carriers close to
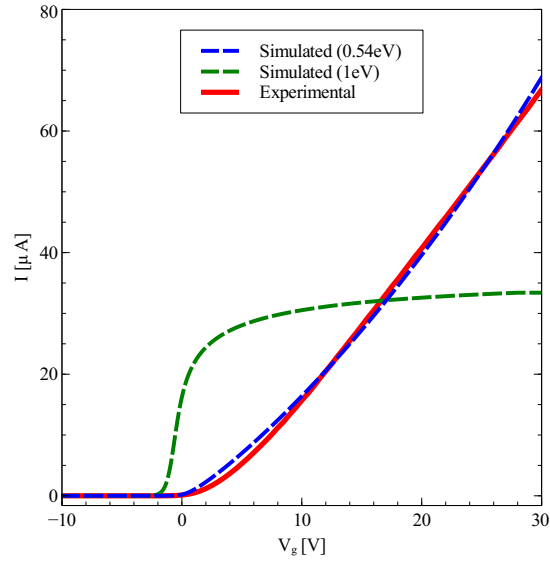
Figure 13.4.: P(NDI2OD-T2). Comparison between experimental (red) and simulated OTFT transcharacteristics. Simulated curves are shown for the nominal barrier value $\Phi_B = 1\,[eV]$ (green) and the extracted optimum $\Phi_B = 0.54\,[eV]$ (blue). The simulation with the nominal barrier results in a severely contact-limited transistor, in fact the transfer characteristic curve becomes flat for high values of V_{gate}.

the metal-semiconductor interface interferes with the gate attraction of charge close to semiconductor-insulator interface, thus making the CV curve less steep. This effect is sizable because the semiconductor film is relatively thin. Therefore, in order to fit experimental data, the smaller Φ_B, the smaller σ.

As expected, the reduction of Φ_B fixes the aforementioned problems. The low-field, low-density carrier mobility is an increasing function of Φ_B and lies in the correct range ($\mu_{0,n} \simeq 10^{-1} \div 10^{-2}\,[cm^2V^{-1}s^{-1}]$) for $\Phi_B < 0.8\,[eV]$. The contact resistance R_C is an increasing function of Φ_B (see figs. 13.3 and 13.9), and for barriers lower than about $0.6 - 0.7\,[eV]$ it lies in the expected range of tens of $[k\Omega\,cm]$. R_C becomes independent of Φ_B for $\Phi_B < 0.55\,[eV]$, since it starts to be dominated and limited by carrier mobility rather than by carrier injection. As to CF curves, the inflection frequency is a decreasing function of Φ_B: its dependence on Φ_B is correlated with the dependence of R_C on Φ_B, meaning that the capacitor is contact limited rather than transport limited. A good agreement with experimental data is obtained for barriers smaller than about $0.6\,[eV]$.
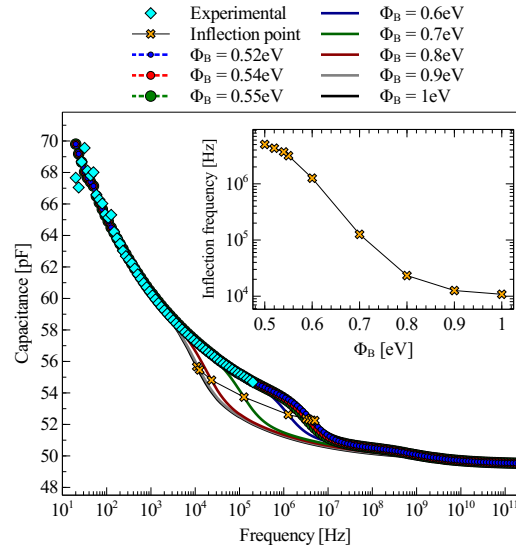
Figure 13.5.: P(NDI2OD-T2). CF curves in the accumulation regime (V_{gate} = +35 [V]), for different values of the injection barrier Φ_B. The inset shows the dependence of the inflection frequency on Φ_B. Experimental CF characteristics shown for comparison (cyan diamonds).

Unfortunately by looking at the dependence of CV and CF curves on Φ_B, only an upper bound for Φ_B can be found, but an optimum value for the barrier cannot be identified. Firstly, the various CV curves are all of comparable quality. In fact, the fitting procedure minimizes the distance between the peaks of measured and simulated dC/dV curves. Irrespective of Φ_B, fittings are very good: peak distances (see fig. 13.10) are comparable for all the barrier values (being almost 3 orders of magnitude smaller than the peak heights themselves) and a clear minimum is not present. Secondly, the relative error between simulated and experimental CF curves is an increasing function of Φ_B but saturates for $\Phi_B < 0.6$ [eV] (see fig. 13.11). This occurs because CF curves tend to become independent of Φ_B for $\Phi_B < 0.55$ [eV] and the inflection frequency tends to saturate at about 5 [MHz]. The situation is further complicated by the fact that in the very range of barrier values which is giving the best agreement between experimental and simulated CF curves and the most plausible value for R_C, viz. $\Phi_B < 0.6$ [eV], the dependence of the DOS width on the barrier becomes very steep and hence the uncertainty on σ very large.

To identify the optimal barrier value we take advantage of OTFT transfer characteristic
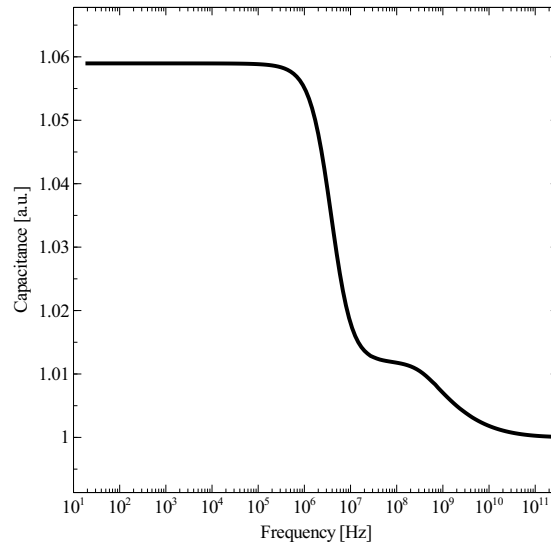
Figure 13.6.: P(NDI2OD-T2). CF characteristic at the optimal barrier $\Phi_B = 0.54\,[eV]$, simulated with a constant insulator permittivity ε_{ins}.

curves. These latter are sensitive to the DOS disorder degree through the dependence of the mobility on the carrier density: the higher is σ, the stronger the dependence of μ on the carrier density, the higher the (positive) curvature of transfer characteristic curves. If we look at the fit residuals of the experimental transfer characteristic curves, reported in Figure 13.12, it can be appreciated that two relative minima exist: one for $\Phi_B = 0.7\,[eV]$ and one for $\Phi_B = 0.54\,[eV]$. The former can be excluded because for a barrier of $0.7\,[eV]$ the simulated CF curve does not reproduce the experimental one, while the latter value lies in the region where CF curves fit the experimental curve and where $\mu_{0,n}$ and R_C values are in agreement with the literature. The DOS width turns out to be $2.6\,k_B T$ and $\mu_{0,n} \simeq 4 \times 10^{-2}\,[cm^2 V^{-1} s^{-1}]$.

With respect to the results reported in [Mad+15], the DOS width is slightly (about 15%) reduced and $\mu_{0,n}$ 30% larger.

The optimum value for Φ_B of $0.54\,[eV]$ is sizeably smaller than the nominal barrier which assumes for gold a work function of $5.0\,[eV]$. But this latter value indeed refers to an atomically clean gold surface. In this case, the gold contact is solvent cleaned and processed in ambient air. As a consequence hydrocarbons are adsorbed on the gold surface, and reduce the metal surface dipole (which significantly contributes to the work function) by means of the so-called push-back effect. It has been demonstrated that

Figure 13.7.: P(NDI2OD-T2). Phase of the carrier density at the semiconductor-insulator interface $\angle n(0)$ in the accumulation regime ($V_{gate} = +35\,[V]$), for different values of the injection barrier Φ_B.

in polymer-gold interfaces gold behaves as it had an *effective* work function of $4.5\,[eV]$ [BSF09]. With a P(NDI2OD-T2) LUMO level of $4.0\,[eV]$ and considering such effective gold work function, the value for Φ_B of $0.54\,[eV]$ we extract is perfectly conceivable.

13.1.3. Conclusions

Experimental CV curves of a MIS capacitor in quasi-equilibrium can be equally well fitted by a relatively large set of values for the DOS width σ and for the Schottky barrier Φ_B. This occurs because a small barrier produces – to a certain extent – the same smoothing effect on the CV curve of a large DOS width. As a consequence, uncertainties on Φ_B result in uncertainties on determining σ.

But if the dynamic, out-of-equilibrium behavior of the MIS capacitor and the transfer characteristic curve in the linear regime of the OTFT are additionally considered, such uncertainty can be drastically reduced. Based on the above considerations we presented a step-by-step procedure to determine the values of the DOS width σ, of the injection barrier Φ_B and of the low-field, low-density mobility $\mu_{0,n}$. In the first step a coarsely spaced set of possible values for Φ_B is selected and for each of those values σ and $\mu_{0,n}$
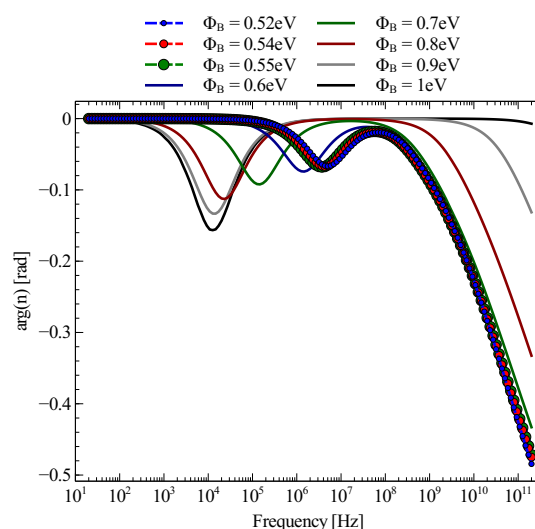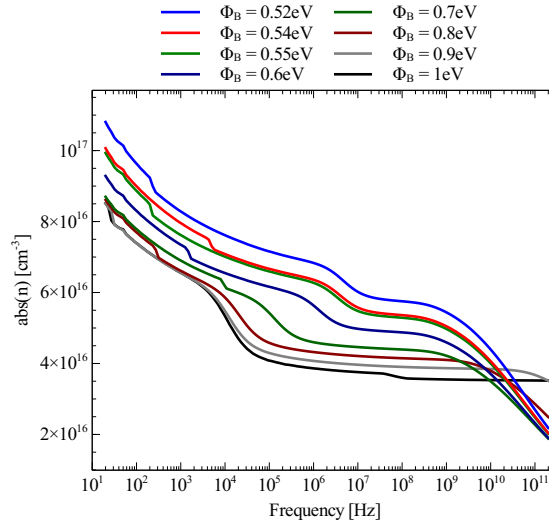
Figure 13.8.: P(NDI2OD-T2). Modulus of the carrier density at the semiconductor-insulator interface $|n(0)|$ in the high accumulation regime ($V_{\text{gate}} = +35\,[\text{V}]$).

are determined by fitting CV curves for a MIS device and the transfer characteristics of an OTFT device respectively. This first step is performed using the fitting procedure defined in [Mad+15], but with a refined model for metal-semiconductor interfaces including field induced barrier lowering. Once the values of σ and $\mu_{0,n}$ corresponding to each assumed value of the barrier height Φ_B are known, the CF curves of the MIS device can be simulated. These latter simulations can be used to restrict the range of acceptable Φ_B values by eliminating those values for which the frequency response of the device is inconsistent with respect to experiments. The set of candidate values for Φ_B within this restricted range is refined and the best fitting value is selected based on the residual of the least-squares distance of experimental to numerical curves.

When applied to the prototypical n-type polymer P(NDI2OD-T2), the proposed strategy results in a value for σ of 2.6k$_B$T, for $\mu_{0,n}$ of $4 \times 10^{-2}\,[\text{cm}^2\text{V}^{-1}\text{s}-1]$ and for Φ_B of 0.54 [eV]. In particular, this latter can be rationalized considering that the polymer LUMO lies at 4.0 [eV] and the gold work function, taking into account its contamination by ambient air hydrocarbons, lies at 4.5 [eV]. This barrier permits to correctly estimate the OTFT contact resistances and to nicely reproduce MIS capacitor CF curves.

We expect that a wide class of materials can be analyzed using the proposed method. Firstly, the involved experimental setup and electrical measurements are simple, requir-
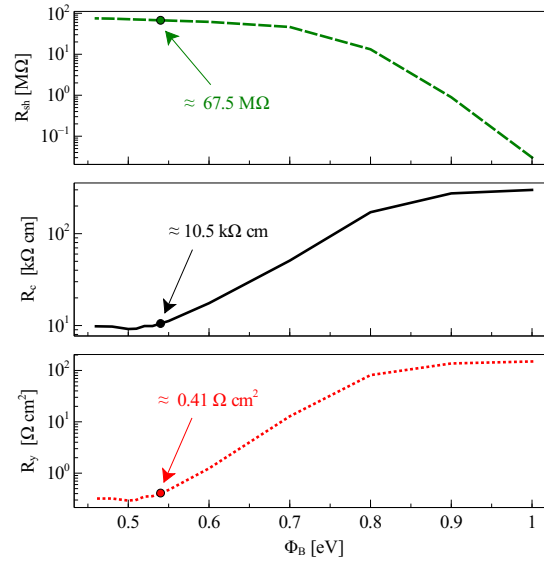
Figure 13.9.: P(NDI2OD-T2). Sheet resistance R_{sh}, access resistance R_y and the resulting contact resistance R_c, extracted at $V_{gate} = +35$ [V] for different values of the injection barrier Φ_B. The dots on the curves identifies the Φ_B value which simultaneously yields in the best fitting of OTFT transfer characteristic curves and of MIS capacitor CF curves.

ing the characterization of the capacitance as a function of frequency in MIS structures and linear transfer characteristics in OTFTs. The requisite on the patterning of the semiconductor in MIS capacitors does not hamper the method applicability: indeed, in this work we have met this requirement through a subtractive, wet-based approach, but should the associated chemistry prove harmful for the semiconductor, other solutions could be devised, such as subtractive, dry etching (e.g. laser patterning) or additive deposition. Secondly, the fitting procedure relies on the description of the DOS as a single Gaussian and of carrier transport according to the analytical formulation given in the framework of the EGDM; in case the spatial correlations are shown to be significant, the closely-related Extended Correlated Disorder Model (ECDM) [Bou+09] could be implemented as well. As to the DOS shape, it has been recognized that only a DOS steeper than the exponential can reproduce the experimentally-observed mobility independence on carrier density at low concentration [Bar14]. Actually, the experimental critical concentration at which the mobility starts to show density-dependence can only be explained assuming a DOS shape very close to the Gaussian one [OHB12]. In general
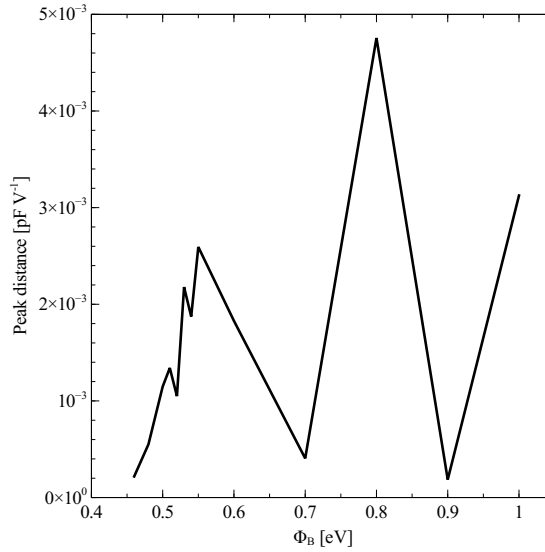
Figure 13.10.: P(NDI2OD-T2). Distance between the peaks of measured and simulated dC/dV curves at different values of the injection barrier Φ_B.

terms, it is possible that a single energy scale cannot effectively describe the real DOS (due to the superposition of inhomogeneously broadened, electronically inequivalent molecular states) [Bar14], as we actually verified for a recently synthesized n-type polymer [Sun+16] that required two Gaussians in order to satisfactorily fit CV curves. In such case, to our knowledge, neither the EGDM nor any other analytical model is able to accurately describe carrier transport. As to the EGDM, we implemented the compact, analytical form for the mobility that is the result of a 1D parametrization of a 3D numerical modeling based on the Master Equation approach. As a consequence, we inherit the limits of such parametrization: the disorder parameter σ cannot substantially exceed about $8k_BT$ [CB12], so that highly disordered materials are excluded. In addition, the model accuracy diminishes at very high concentrations (above $0.1N_0$) and fields (above $2\sigma/qa$, with a the inter-site distance) [VC08], but this has no actual impact: the highest carrier concentration in MIS structures does not exceed a few $0.001N_0$, and longitudinal fields are in the range of a few thousands of $2\sigma/qa$ in OTFTs biased in the linear regime. Thirdly, thanks to the proper modeling of the metal-semiconductor interface, there is no strict need for a perfectly ohmic contact as long as the width of the quasi-static frequency plateau of the MIS capacitor is sufficiently large to be easily measured and identified.

To summarize, the combined exploitation of MIS CV and CF curves and OTFT transfer
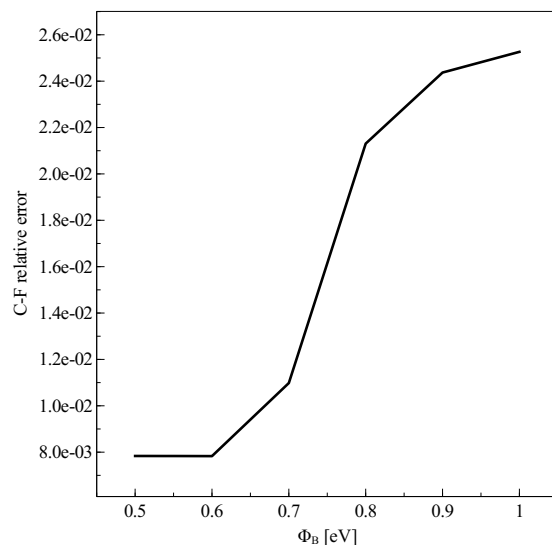
Figure 13.11.: P(NDI2OD-T2). Relative error between experimental and simulated CF characteristics for each barrier value Φ_B.

characteristic curves, enables the simultaneous assessment of the width of the Gaussian DOS, of the carrier mobility and of the metal-semiconductor injection barrier. The possibility to extract these three quantities by means of simple electrical measurements is extremely valuable, especially considering that the assessment of injection barriers usually requires dedicated and non-trivial experimental setups. The presented approach can thus easily empower a more detailed knowledge of organic semiconductors and foster further fundamental studies.

13.1.4. Methods

13.1.4.1. Experimental

Experimental data have been taken from [Mad+15], where MIS capacitors were developed by spin-coating P(NDI2OD-T2) upon a gold bottom contact. The semiconductor was patterned [Cha+10] to suppress the spurious effect of lateral carrier spreading [TA08; Ull+09; Jun+07]. PMMA was then spin coated as insulator and Aluminum was evaporated as gate contact. MIS capacitors were measured by means of an Agilent E4980A Precision LCR Meter, applying to the gate an oscillation amplitude of 100 [mV] of variable frequency superimposed to a biasing constant voltage.
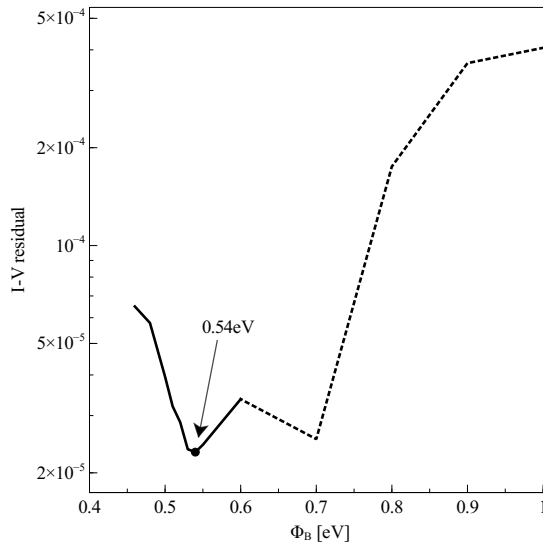
Figure 13.12.: P(NDI2OD-T2). Residual of the least-squares fit of the OTFT transfer characteristic curves with contact resistance effects taken into account, at different values of the injection barrier Φ_B. The solid line represents the range of barrier values that correspond to acceptable CF curves, as shown in fig. 13.5, while the dotted line is used for the range of barrier height values for which it is not possible to fit experimental CF curves and thus are to be considered unacceptable.

On the same substrate OTFTs were realized in a staggered, top-gate bottom-contact configuration with gold source and drain contacts and Al gate and a channel width and length of $10\,[\text{mm}]$ and $10\,[\mu m]$. Transfer characteristic curves were measured applying a drain-to-source voltage of $5\,[\text{V}]$ by means of Agilent B1500A Semiconductor Parameter Analyzer.

13.1.4.2. Models for Numerical Simulations

Charge transport in the considered devices is modeled, in transient regime, by the Drift-Diffusion model presented in section 6.1.

Transient simulations are used to compute the voltage and frequency dependence of the small-signal capacitance of the MIS capacitor, according to the numerical methods presented in section 6.3. The DD model features that are more important for this study
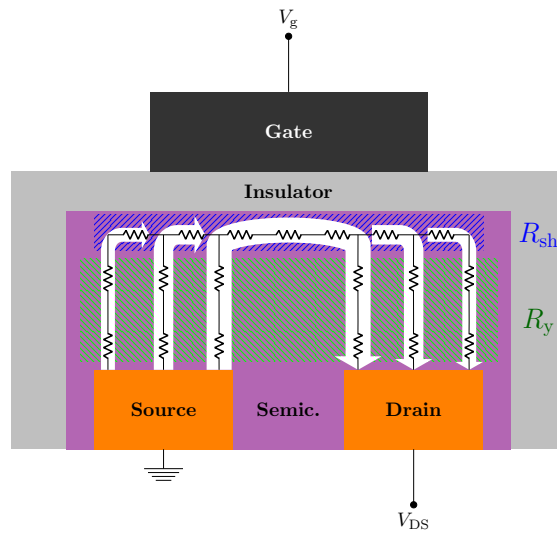
Figure 13.13.: Sketch of the OTFT under current crowding effects.

are: *i)* the boundary condition representing charge injection through the Schottky barrier at the metal-semiconductor interface, and *ii)* the dependence of the mobility and of the diffusion coefficient on the DOS width. While useful for computing the capacitance over a wide range of frequencies, the full DD model turns out to be of too high complexity and of insufficient numerical accuracy for efficiently fitting measured low-frequency CV curves. For this reason the NLP model, described in section 6.2, which includes an accurate description of the contact injection barrier with respect to the previous work [Mad+15] and is therefore fully consistent with the zero-frequency limit of the complete DD model, was simulated.

The latter extended NLP model naturally describes the effect of the deviation from Einstein's relation but, as it is derived for the quasi-static regime, it does not require to model the mobility coefficient.

13.1.4.3. Modeling the OTFT

We will describe hereafter the models used for computing the transfer characteristics curve of the OTFT, shown in fig. 13.13, in a one-dimensional setting.

Once the DOS width σ has been extracted by fitting static CV curves, the low-field, low-density mobility $\mu_{0,n}$ can be determined by computing OTFT transfer characteristics

in the linear regime. The drain-to-source current is expressed as

$$I_{DS}(V_{gate}) = \frac{V_{DS}}{R_{tot}(V_{gate})},$$

where V_{DS} is the potential drop across the channel and R_{tot} is the total device resistance, accounting for both the channel and the contact resistance contributions:

$$R_{tot} = R_{ch} + R_C,$$

where the channel resistance R_{ch} is given by:

$$R_{ch} = \left[\frac{W}{L} \int_{\Omega_{semic}} q\mu_n n \right]^{-1}, \tag{13.1}$$

W and L being the channel width and length respectively. As for R_C, we followed the physical description provided in [NC12; Jun+08] in the framework of current crowding regime. By considering the contributions due to the current flow across the accumulated channel and along the semiconductor layer, characterized by a sheet resistance R_{sh} and a resistance per unit area R_y respectively, the contact resistance is computed as:

$$R_C = \frac{R_y}{WL_0 \tanh(L_{ov}/L_0)},$$

where L_{ov} is the overlap length between the gate and the source-drain electrodes, $L_0 = \sqrt{R_y/R_{sh}}$ and

$$R_{sh} = \left(\int_{\Omega_{semic}} q\mu_n n \right)^{-1}, \tag{13.2}$$

$$R_y = \int_{\Omega_{semic}} \left(q\,\mu_n n \right)^{-1}, \tag{13.3}$$

where Ω_{semic} is the semiconductor region of the computational domain.

The integrand functions in equations (13.1), (13.2), (13.3) are computed by simulating, as highlighted in fig. 13.13, two different one-dimensional vertical cross-sections corresponding to the middle of the channel (R_{ch}, R_{sh}) and to the source contact (R_y) respectively.

The mobility coefficient $\mu_n(z)$ is expressed through the EGDM model (5.24), where the enhancement factors $g_1(n)$ and $g_2(\mathcal{E})$ ($\mathcal{E} = V_{DS}/L$ is the drain-to-source field) can be easily computed once σ is known, as described in section 5.5. Therefore, the total

current I_{DS} is known up to the multiplicative constant $\mu_{0,n}$, which is then extracted by fitting numerical and experimental IV curves through a least-squares procedure. The fitting residual has been exploited to determine the optimal value of Φ_B, as shown in fig. 13.12.

13.2. PBTTT

The parameter estimation procedure described in the previous section was also tested to characterize the physical properties of the p-type Poly(2,5-bis(3-tetradecylthiophen-2-yl)thieno[3,2-b]thiophene) (PBTTT) semiconductor, starting from experimental data on a MIS capacitor and an OTFT based on this polymer.

Experimental data taken from [Mad+15] would lead to estimate a nominal injection barrier $\Phi_B = 0.9$ [eV]. As described in the previous section, the uncertainty in determining a physically meaningful value of Φ_B affects other physical properties as obtained by fitting the MIS experimental CV curve, which leads to the dependence of σ and the contact resistance R_C on Φ_B shown in figs. 13.14 and 13.15 respectively.
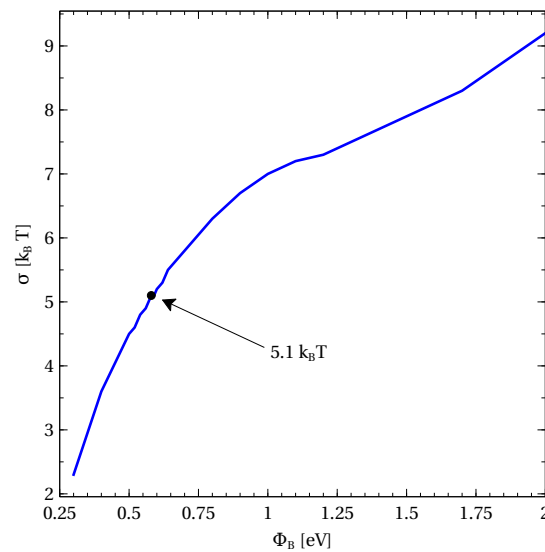
Figure 13.14.: PBTTT. Dependence of the fitted Gaussian DOS width σ on the injection barrier Φ_B. The dot on the curve identifies the σ value that simultaneously yields in the best fitting of OTFT transfer characteristic curves and of MIS capacitor CF curves.
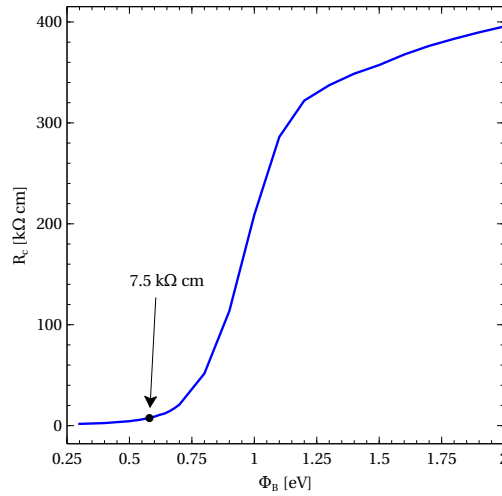
Figure 13.15.: PBTTT. Contact resistance R_C (at $V_{gate} = +35\,[V]$) for different values of the injection barrier Φ_B. The dots on the curves identify the Φ_B value that simultaneously yields in the best fitting of OTFT transfer characteristic curves and of MIS capacitor CF curves.

However, the uncertainty can be reduced by fitting IV transfer characteristics of the OTFT. The procedure yields to the residual in fig. 13.16 that has a unique minimum, corresponding to the optimal barrier value $\Phi_B = 0.58\,[eV]$ and, accordingly, $\sigma = 5.1 k_B T$ and $\mu_{0,n} = 7.84 \cdot 10^{-8}\,[cm^2 V^{-1} s^{-1}]$. The resulting fitted IV curve, compared to experimental data, is shown in fig. 13.17.

In this case experimental CF curves are limited to a narrow range of frequencies. Therefore, the validation of the values extracted is not as clear as in the case of P(NDI2OD-T2) since both the nominal and the optimal set of parameters seem to provide a good agreement to experimental measurements, as reported in fig. 13.18. Anyhow, the ratio between the capacitance computed in the accumulation and in the depletion regime shows that the nominal barrier leads to a capacitance drop at a low frequency of about $10^3\,[Hz]$ that is not seen in experimental data, while the optimal barrier results in a plateau extending to a range that perfectly matches the one seen in experiments.

178
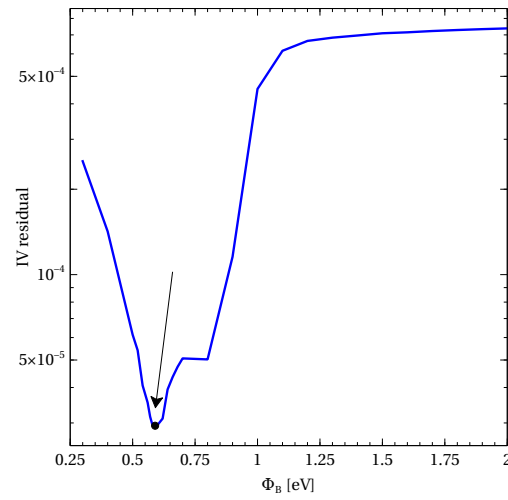
Figure 13.16.: PBTTT. Residual of the least-squares fit of the OTFT transfer characteristic curves with contact resistance effects taken into account, at different values of the injection barrier Φ_B.
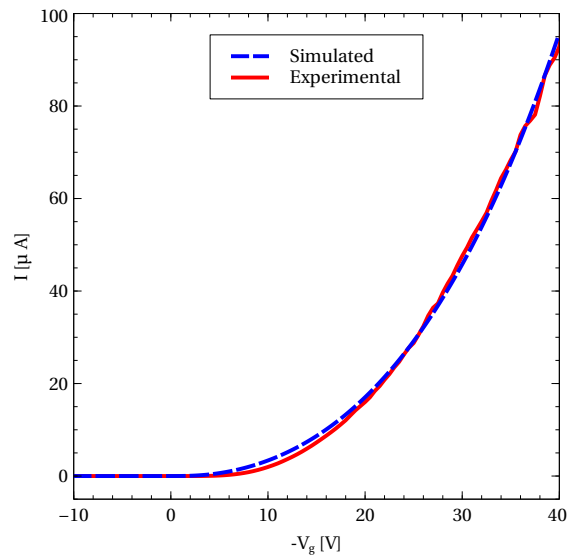
Figure 13.17.: PBTTT. Comparison between experimental (red) and simulated OTFT transcharacteristics at the optimal barrier value $\Phi_B = 0.58$ [eV].
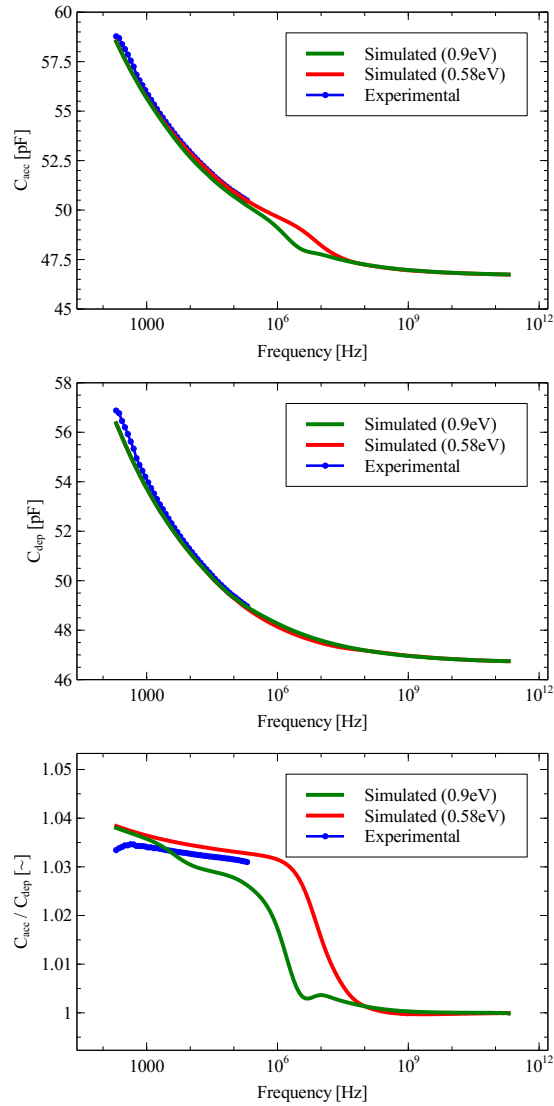
Figure 13.18.: PBTTT. CF curves in the accumulation regime ($V_{\text{gate}} = +35\,[\text{V}]$), the depletion regime ($V_{\text{gate}} = -15\,[\text{V}]$) and normalized, computed for the nominal injection barrier $\Phi_B = 0.9\,[\text{eV}]$ and for the optimal barrier $\Phi_B = 0.58\,[\text{eV}]$. Experimental CF characteristics shown for comparison.

14. Stationary 2D simulations of OTFTs

The equilibrium model presented in section 6.2 has been used to simulate the OTFT geometry for different applied gate voltages V_{gate} in the interval $[-5V, 20V]$.

Figure 14.1 shows the solution to the NLP equation and the corresponding adapted mesh at $V_{gate} = -5\,[V]$, while results corresponding to different gate voltages are displayed in fig. 14.2.

(a) Solution φ at gate voltage $V_{gate} = -5\,[V]$.　　(b) Initial mesh at gate voltage $V_{gate} = -5\,[V]$.
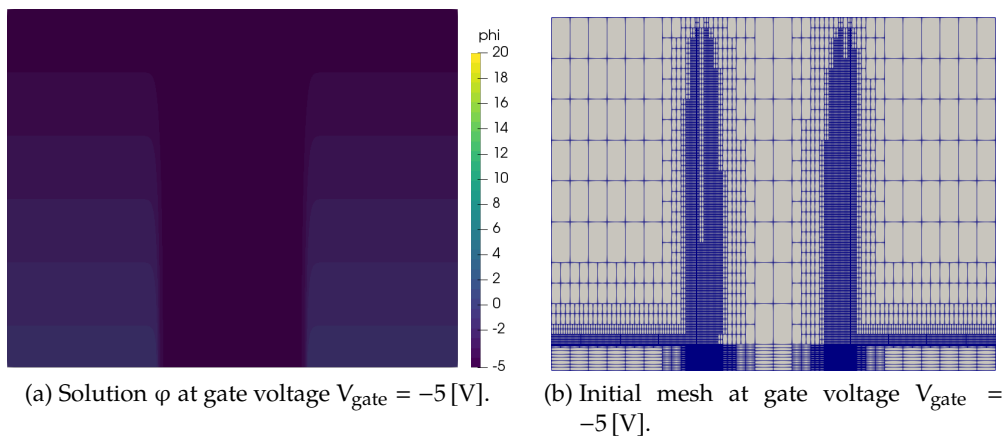
Figure 14.1.: Problem 14. Solution and mesh at gate voltage $V_{gate} = -5\,[V]$.

The previous results have been used to compute the device capacitance, in fig. 14.3. The figure shows the comparison of the CV curve simulated using the adaptation procedure and a uniform mesh with about $6 \cdot 10^4$ degrees of freedom, that empirical evidence has proved to be the coarsest possible mesh required to reach the specified level of accuracy. The benefits provided by the adaptive mesh in terms of computational costs are noticeable: the same level of accuracy in the computation of the CV curve can be attained with about 75% less degrees of freedom by taking advantage of the adaptation algorithm.

Numerical simulations have also been exploited to compute the mid-channel potential shown in fig. 14.4, that is the electric potential φ evaluated at the semiconductor-

(a) Solution φ at gate voltage $V_{\text{gate}} = -2.5\,[\text{V}]$.

(b) Adapted mesh at gate voltage $V_{\text{gate}} = -2.5\,[\text{V}]$.

(c) Solution φ at gate voltage $V_{\text{gate}} = -0.7\,[\text{V}]$.

(d) Adapted mesh at gate voltage $V_{\text{gate}} = -0.7\,[\text{V}]$.

(e) Solution φ at gate voltage $V_{\text{gate}} = 20\,[\text{V}]$.

(f) Adapted mesh at gate voltage $V_{\text{gate}} = 20\,[\text{V}]$.

Figure 14.2.: Problem 14. Solution φ and adapted meshes computed at different gate voltages.
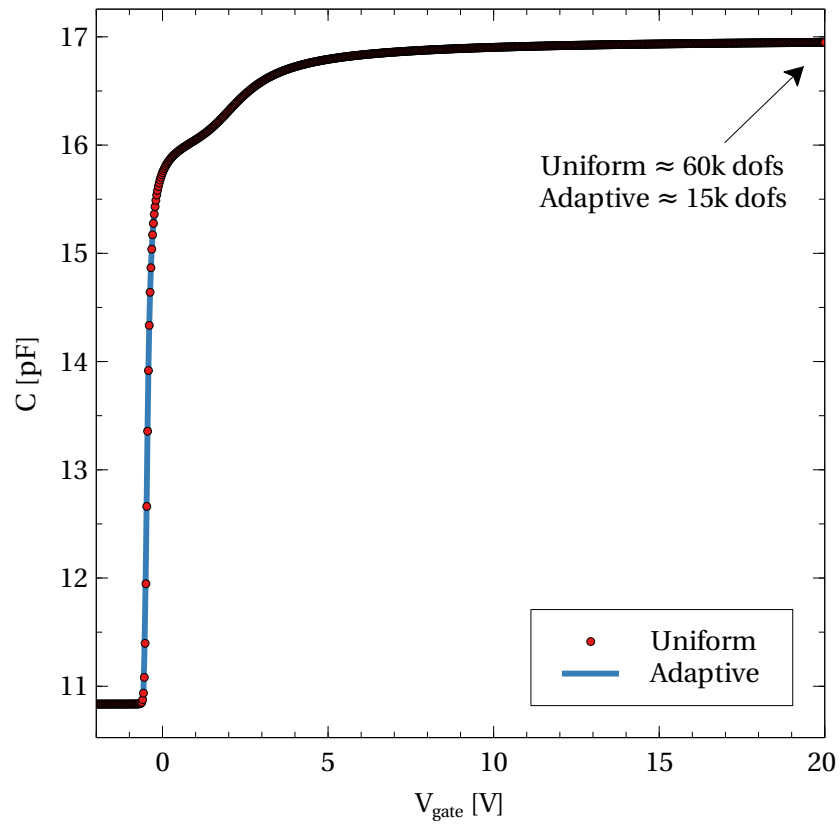
Figure 14.3.: Problem 14. Comparison of the CV curve simulated using uniform and adaptive meshes.

Figure 14.4.: Problem 14. Mid-channel potential for different applied gate voltages.

substrate interface, *i.e.* the midpoint of the substrate between the source and drain contacts. The results confirm that the assumptions made in chapter 13 to compute the OTFT IV curve based on 1D models is verified, since the midpoint potential in the accumulation regime – *i.e.* when current actually flows – is constant with respect to the applied gate voltage.

15. Transient 2D simulations of OTFTs

Once the application of the procedure illustrated in chapter 13 has provided the intrinsic parameters of an OTFT, transient simulations of the full DD system presented in section 6.1 can be performed in a predictive fashion to understand the device behavior under specific working regimes.

This chapter aims at presenting the results of the simulation of an OTFT to reproduce the same setting used for the experimental computation of the transfer characteristic curve. Let the simulation timespan be the interval $(0, 350s]$. The gate and the drain contacts are connected to ramp voltage generators: firstly, the desired drain voltage of $5\,[V]$ is applied through

$$V_D(t) = \begin{cases} 0, & t \in (0, 50], \\ 5 \cdot \dfrac{t - 50}{100}, & t \in [50, 150], \\ 5, & t \in [150, 350]. \end{cases}$$

Then, the gate voltage is increased up to $50\,[V]$:

$$V_{gate}(t) = \begin{cases} 0, & t \in (0, 200], \\ 50 \cdot \dfrac{t - 200}{100}, & t \in [200, 300], \\ 50, & t \in [300, 350]. \end{cases}$$

The source contact is kept grounded, *i.e.* $V_S(t) = 0$.

The considered geometry is the one depicted in fig. 13.13, where both the contact and channel length are set equal to $10\,\big[\mu m\big]$. The computational domain is further extended from both sides of an additional $10\,\big[\mu m\big]$ length accounting for the fingered structure of a realistic OTFT, as in fig. 3.1.

The computed electric potential φ and electron density n in the semiconductor region at $t = 150$, *i.e.* when $V_D = 5\,[V]$ and $V_{gate} = 0\,[V]$, are shown in fig. 15.1: under such conditions, the channel is pinched off as the region surrounding the drain contact is depleted of carriers – the minimum electron density is of about $10^{-58}\,\big[m^{-3}\big]$ – and the transistor is still off.

(a) Electric potential φ [V].

(b) Electron density n $[m^{-3}]$.
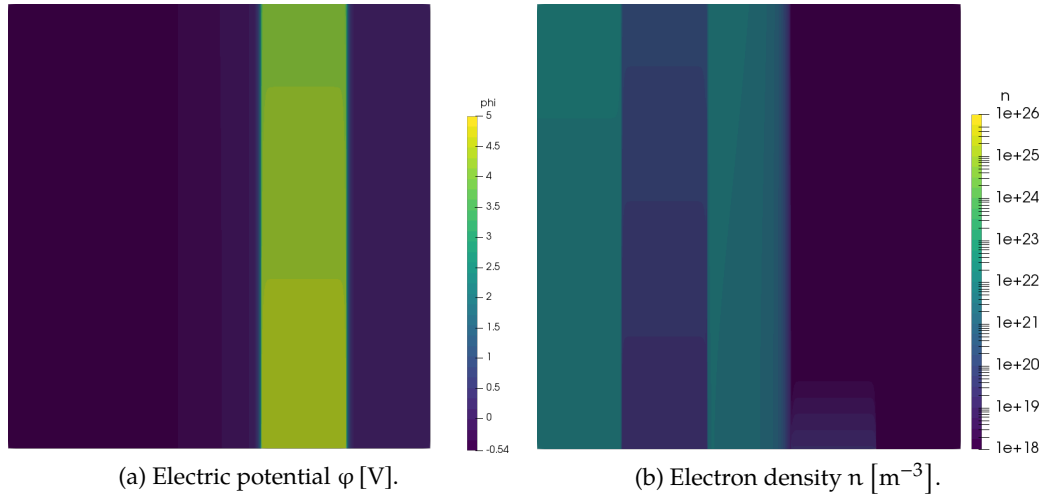
Figure 15.1.: Problem 15. Solution at $V_D = 5$ [V], $V_{gate} = 0$ [V]. Only the semiconductor region is shown.

(a) Electric potential φ [V].

(b) Electron density n $[m^{-3}]$.
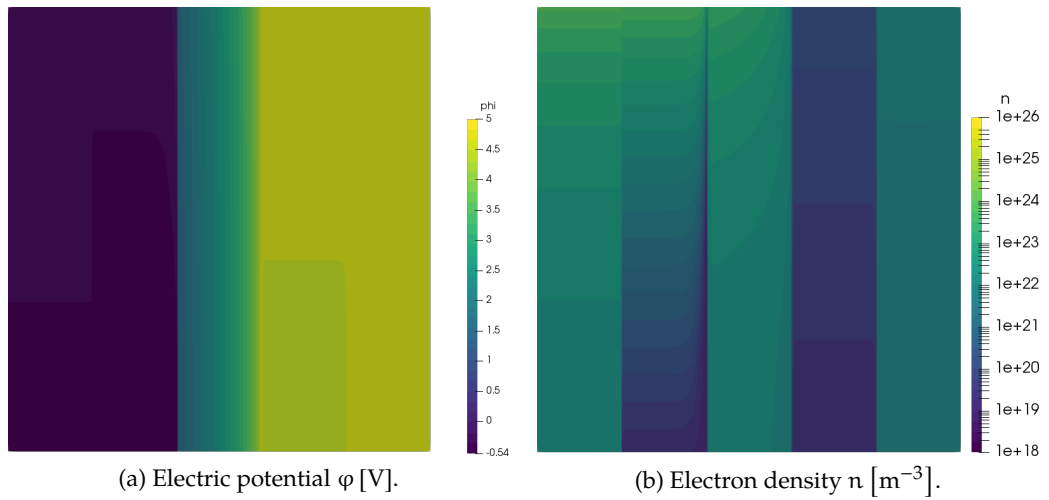
Figure 15.2.: Problem 15. Solution at $V_D = 5$ [V], $V_{gate} = 5$ [V]. Only the semiconductor region is shown.

A channel is created by increasing the gate voltage to a value $V_{gate} > V_D + V_T$ that turns the transistor on, V_T being the threshold voltage described in section 3.1: as shown in fig. 15.2 the charge carrier concentration in the lateral region next to the drain contact grows up to a value of about $10^{19}\,[m^{-3}]$. The transition between these two regimes is delicate from a numerical perspective, as dealing with a variation of n of about 77 orders of magnitude demands for a remarkably robust scheme.

The current flow in the OTFT can be tuned by properly adjusting the gate voltage: the computed φ, n and the vector field $\mathbf{J}_n$ for $V_{gate} = 15.5\,[V]$ and $V_{gate} = 50\,[V]$ are shown in figs. 15.3 and 15.4, respectively. Such results provide a numerical proof of the current crowding phenomenon: the current flow originating to/from the source/drain contacts is non-negligible only in correspondence of thin regions alongside the channel. It is also remarkable that the crowding is asymmetric, as it is restricted to a much narrower region at the drain side rather than at the source contact.

Due to the thinness of the semiconductor film, the channel depth extends far beyond the semiconductor-insulator interface, as a non-negligible drain-to-source current flows also at the substrate. We also remark that the zero normal current condition at the interface is matched.

Finally, at the drain side the current vanishes at a short distance from the channel, which is not the case at the source side. This suggests that electrons, going in the opposite way as the current density $\mathbf{J}_n$, follow a path that extends also beyond the source contact: a carrier moving from the source contact towards the semiconductor-insulator interface initially gets driven away from the channel. Then, when close to the interface, the electron turns back and moves parallel to the interface to reach the drain region, where it is collected by the drain contact.

(a) Electric potential φ [V].

(b) Electron density n $\left[m^{-3}\right]$.

(c) Current density J_n $\left[A \cdot m^{-2}\right]$, colored based on its modulus.
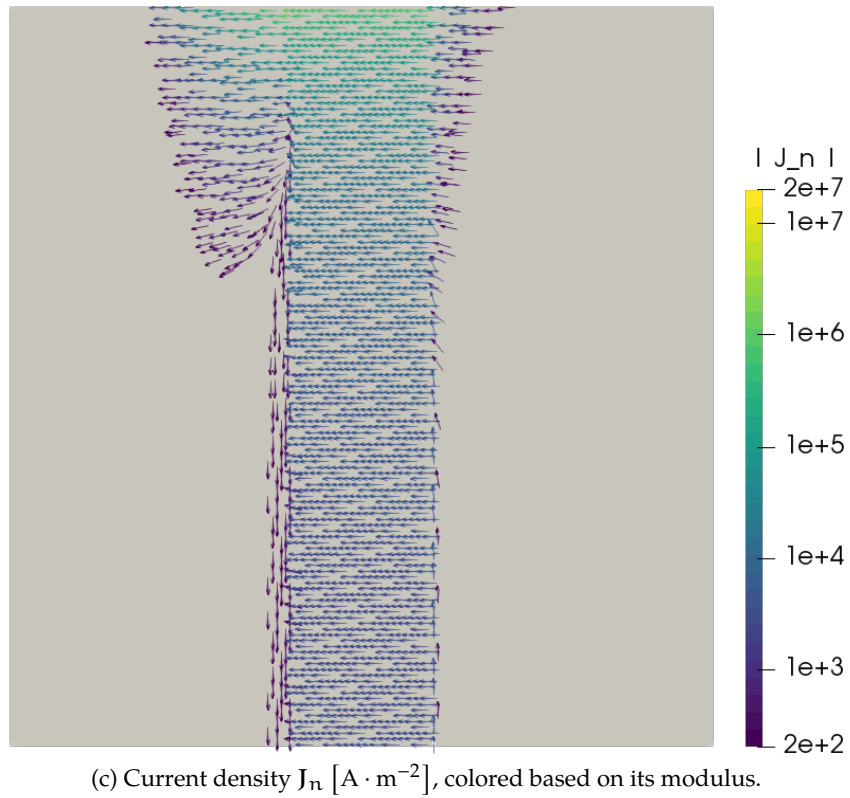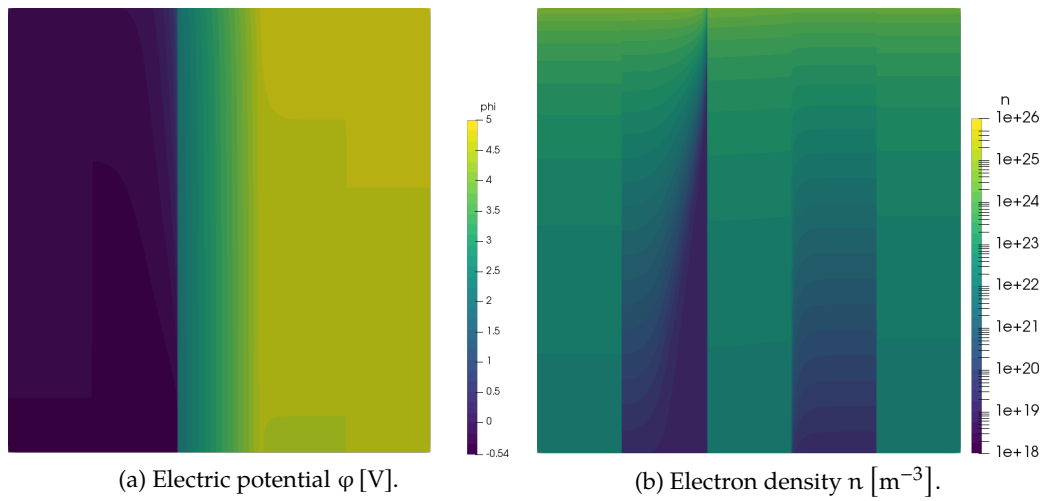
Figure 15.3.: Problem 15. Solution at $V_D = 5$ [V], $V_{gate} = 15.5$ [V]. Only the semiconductor region is shown.

(a) Electric potential φ [V].

(b) Electron density n $\left[m^{-3}\right]$.

(c) Current density J_n $\left[A \cdot m^{-2}\right]$, colored based on its modulus.
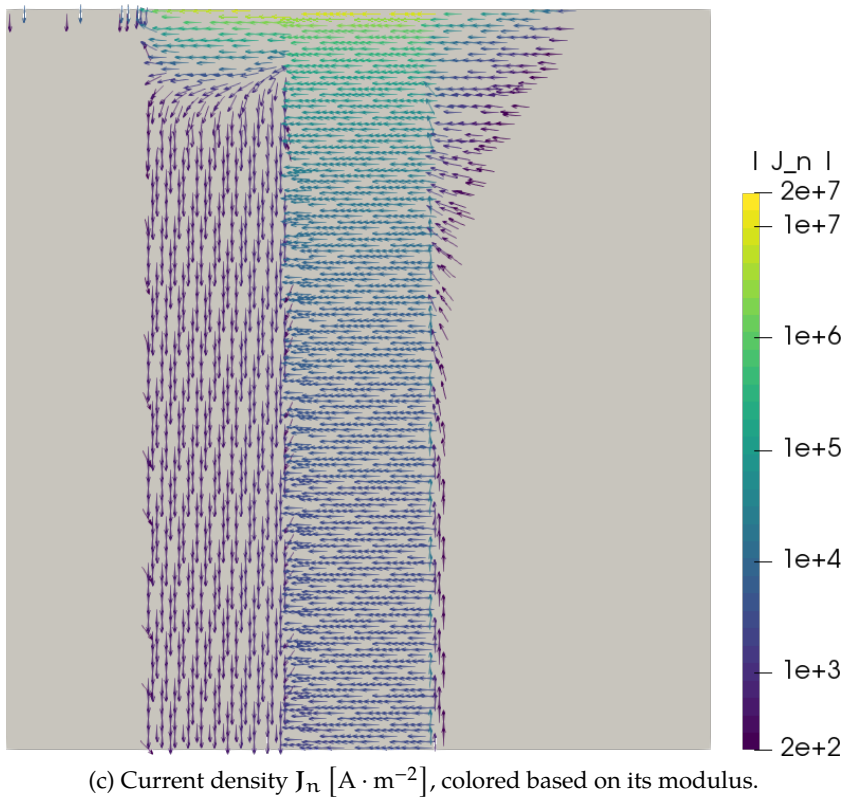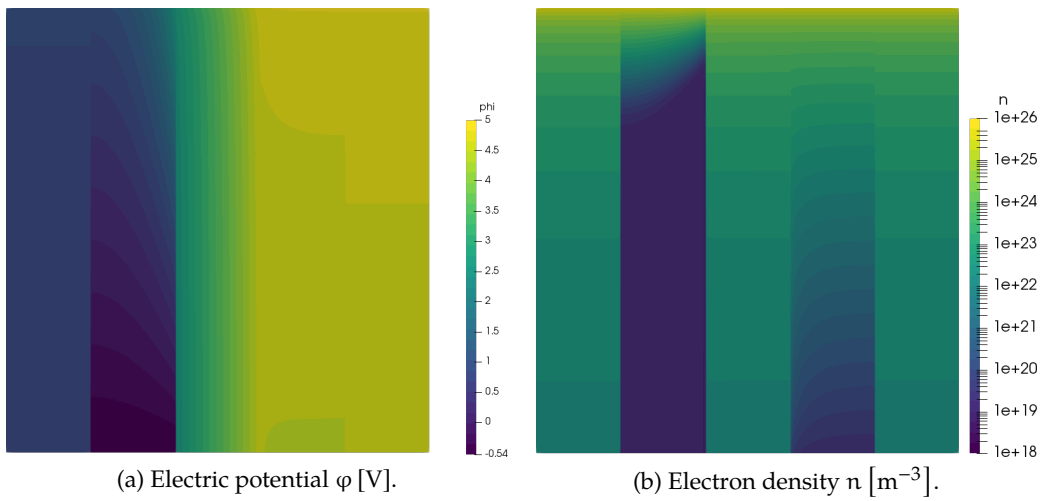
Figure 15.4.: Problem 15. Solution at $V_D = 5\,[V]$, $V_{gate} = 50\,[V]$. Only the semiconductor region is shown.

16. Conclusions and future work

In this Ph.D. thesis we have addressed the problem of mathematical modeling and numerical simulating organic semiconductor devices, with a particular focus on Organic Thin-Film Transistors (OTFTs), a key component for electronic circuits.

The applicative relevance and impact of the above ambition has prompted our research towards

1. deriving an accurate mathematical description of the several complex physical phenomena involved in charge transport in organic semiconductors;

2. proposing and implementing robust, stable, accurate and high-performance numerical schemes for the analysis of the proposed models on the solution of both academic and application-motivated test problems.

More specifically, the first issue has been addressed by embracing state-of-the-art differential models describing charge transport in the devices under consideration. Indeed, accurate models of the physics of energy barrier lowering and charge injection at metal-semiconductor interfaces and constitutive relations that are representative of the molecular disorder of organic semiconductor materials have been included in the framework of the DD equations. Moreover, we have derived a hierarchy of mathematical formulations that has been shown to provide a consistent representation of the considered physical systems under equilibrium, transient and time harmonic regimes of operation. The DD system has been coupled with a proper additional algebraic equation to be solved for the *enhancement potential* that provides discrete consistency.

Dealing with the peculiarities of charge transport in OTFTs, such as the disordered morphology and energetic structure, and with the typically extreme form-factors of such devices constituted a challenge demanding high level of accuracy and properties of robustness and stability for the schemes employed in the numerical treatment of the systems under analysis. In this regard, we have presented a modification of the Scharfetter-Gummel discretization method, relying on the above mentioned enhancement potential, that has been shown to provide discrete consistence with the thermodynamic limit for arbitrary DOS shapes – even those that don't match with the classical Einstein relation. This scheme satisfies in particular a discrete maximum principle that

makes it positivity-preserving, as required by the constraint of non-negative electron density. This strategy has been combined with an adaptive time-advancing scheme and a robust linearization method.

The need to account for a set of inherently multi-dimensional phenomena – namely the non-planarity of semiconductor-insulator interfaces (due to the solution processing of the materials), parasitic capacitances (due to the coupling between metal layers), the bending of energy bands at the semiconductor-substrate interface away from contacts and the contact resistance (due to current-crowding effects) – has motivated the extension of the above described numerical scheme to 2D geometries on meshes of quadtrees. The accuracy has also been increased by deriving a new recovery metric-based mesh adaptation procedure.

In the framework of HPC, the goal of achieving extreme scalability has driven the development of an efficient, parallel, scalable finite element code that has resulted in the in-house software `bim++`, a high-level `C++` interface to `p4est`, the dynamic back-end manager of quadtree data structures.

Despite our endeavors, not all possible issues concerning the mathematical modeling in the field of organic semiconductor devices have been settled. The presented work still warrants for further extensions.

First of all, the implementation of a DD code performing out-of-equilibrium 2D numerical simulations with automatic mesh adaptation is still a delicate task from a robustness perspective.

Moreover, the boundary condition imposed at metal-semiconductor interfaces, as described in section 5.6.1, suffers from coefficient discontinuities arising from extending physical models that are known to be valid only in asymptotic regimes also to transition regions. This justifies a deeper investigation of the physical phenomena involved in correspondence of such interfaces. In particular, a multiscale coupling of the DD system with a molecular model at the interface is desirable.

References

[AFP19]   P. C. Africa, C. de Falco, and S. Perotto. "Scalable Recovery-based Adaptation on Quadtree Meshes". In: *In preparation* (2019) (cit. on pp. 24, 97, 133).

[Afr+17]   P. C. Africa, C. de Falco, F. Maddalena, M. Caironi, and D. Natali. "Simultaneous Extraction of Density of States Width, Carrier Mobility and Injection Barriers in Organic Semiconductors". In: *Scientific Reports* 7.1 (2017), p. 3803 (cit. on pp. 23, 54, 55, 161).

[Bar14]   S. D. Baranovskii. "Theoretical Description of Charge Transport in Disordered Organic Semiconductors". In: *Physica Status Solidi (b)* 251.3 (2014), pp. 487–525 (cit. on pp. 51, 171, 172).

[BH82]   A. N. Brooks and T. J. R. Hughes. "Streamline Upwind/petrov-galerkin Formulations for Convection Dominated Flows with Particular Emphasis on the Incompressible Navier-Stokes Equations". In: *Computer Methods in Applied Mechanics and Engineering* 32 (1982), pp. 199–259 (cit. on p. 144).

[Bou+09]   M. Bouhassoune, S. L. M. v. Mensfoort, P. A. Bobbert, and R. Coehoorn. "Carrier-density and Field-dependent Charge-carrier Mobility in Organic Semiconductors with Correlated Gaussian Disorder". In: *Organic Electronics: Physics, Materials, Applications* 10.3 (2009), pp. 437–445 (cit. on pp. 44, 53, 171).

[BSF02]   L. Bürgi, H. Sirringhaus, and R. H. Friend. "Noncontact Potentiometry of Polymer Field-effect Transistors". In: *Applied Physics Letters* 80.16 (2002), pp. 2913–2915 (cit. on p. 162).

[BSF09]   S. Braun, W. R. Salaneck, and M. Fahlman. "Energy-level Alignment at Organic/metal and Organic/organic Interfaces". In: *Advanced Materials* 21.14-15 (2009), pp. 1450–1472 (cit. on pp. 162, 169).

[Buc+15]   S. G. Bucella, A. Luzio, E. Gann, L. Thomsen, C. R. McNeill, G. Pace, A. Perinot, Z. Chen, A. Facchetti, and M. Caironi. "Macroscopic and High-throughput Printing of Aligned Nanostructured Polymer Semiconductors for Mhz Large-area Electronics". In: *Nature Communications* 6 (2015), p. 8394 (cit. on p. 163).

References

[Bür+03]   L. Bürgi, T. J. Richards, R. H. Friend, and H. Sirringhaus. "Close Look at Charge Carrier Injection in Polymer Field-effect Transistors". In: *Journal of Applied Physics* 94.9 (2003), pp. 6129–6137 (cit. on p. 162).

[Cai+10]   M. Caironi, C. Newman, J. R. Moore, D. Natali, H. Yan, a. Facchetti, and H. Sirringhaus. "Efficient Charge Injection from a High Work Function Metal in High Mobility N-type Polymer Field-effect Transistors". In: *Applied Physics Letters* 96.18 (2010), p. 183303 (cit. on p. 164).

[CB12]   R. Coehoorn and P. A. Bobbert. "Effects of Gaussian Disorder on Charge Carrier Transport and Recombination in Organic Semiconductors". In: *Physica Status Solidi (a)* 209.12 (2012), pp. 2354–2377 (cit. on pp. 38, 172).

[Cha+10]   J.-F. Chang, M. C. Gwinner, M. Caironi, T. Sakanoue, and H. Sirringhaus. "Conjugated-polymer-based Lateral Heterostructures Defined by High Resolution Photolithography". In: *Advanced Functional Materials* 20.17 (2010), pp. 2825–2832 (cit. on p. 173).

[Coe+05]   R. Coehoorn, W. F. Pasveer, P. A. Bobbert, and M. A. J. Michels. "Charge-carrier Concentration Dependence of the Hopping Mobility in Organic Materials with Gaussian Disorder". In: *Physical Review B* 72.15 (15 2005), p. 155206 (cit. on pp. 53, 162).

[FDS09]   M. H. Flamm, S. L. Diamond, and T. Sinno. "Lattice Kinetic Monte Carlo Simulations of Convective-diffusive Systems". In: *The Journal of Chemical Physics* 130.9 (2009), p. 094904 (cit. on p. 147).

[FO09]   C. de Falco and E. O'Riordan. "A Patched Mesh Method for Singularly Perturbed Reaction-diffusion Equations". In: *BAIL 2008-Boundary and Interior Layers*. Springer, 2009, pp. 117–127 (cit. on p. 134).

[FO10]   C. de Falco and E. O'Riordan. "Interior Layers in a Reaction-Diffusion Equation with a Discontinuous Diffusion Coefficient". In: *International Journal of Numerical Analysis & Modeling* 7.3 (2010), pp. 444–461 (cit. on p. 137).

[Jun+07]   K.-D. Jung, C. A. Lee, D.-W. Park, B.-G. Park, H. Shin, and J. D. Lee. "Admittance Measurements on Ofet Channel and Its Modeling with R-c Network". In: *IEEE Electron Device Letters* 28.3 (2007), pp. 204–206 (cit. on p. 173).

[Jun+08]   K.-D. Jung, Y. C. Kim, B.-J. Kim, B.-G. Park, H. Shin, and J. D. Lee. "An Analytic Current-voltage Equation for Top-contact Organic Thin Film Transistors Including the Effects of Variable Series Resistance". In: *Japanese Journal of Applied Physics* 47.4S (2008), p. 3174 (cit. on pp. 163, 164, 176).

[Koc07]   N. Koch. "Organic Electronic Devices and Their Functional Interfaces". In: *ChemPhysChem* 8.10 (2007), pp. 1438–1455 (cit. on p. 162).

[Mad+15]   F. Maddalena, C. de Falco, M. Caironi, and D. Natali. "Assessing the Width of Gaussian Density of States in Organic Semiconductors". In: *Organic Electronics* 17 (2015), pp. 304–318 (cit. on pp. 30, 47, 51, 161–164, 168, 170, 173, 175, 177).

[NC12]   D. Natali and M. Caironi. "Charge Injection in Solution-processed Organic Field-effect Transistors: Physics, Models and Characterization Methods". In: *Advanced Materials* 24.11 (2012), pp. 1357–1387 (cit. on pp. 163, 164, 176).

[OHB12]   J. O. Oelerich, D. Huemmer, and S. D. Baranovskii. "How to Find Out the Density of States in Disordered Organic Semiconductors". In: *Physical Review Letters* 108.22, 226403 (May 29, 2012), p. 226403 (cit. on pp. 157, 171).

[OKH14]   M. Oehzelt, N. Koch, and G. Heimel. "Organic Semiconductor Density of States Controls the Energy Level Alignment at Electrode Interfaces". In: *Nature Communications* 5 (2014), p. 4174 (cit. on p. 162).

[RBI18]   A. Raeli, M. Bergmann, and A. Iollo. "A Finite-difference Method for the Variable Coefficient Poisson Equation on Hierarchical Cartesian Meshes". In: *Journal of Computational Physics* 355 (2018), pp. 59–77 (cit. on pp. 140, 143).

[Sch+12]   D. Schillinger, L. Dede', M. A. Scott, J. A. Evans, M. J. Borden, E. Rank, and T. J. R. Hughes. "An Isogeometric Design-through-analysis Methodology Based on Adaptive Hierarchical Refinement of Nurbs, Immersed Boundary Methods, and T-spline Cad Surfaces". In: *Computer Methods in Applied Mechanics and Engineering* 249 (2012), pp. 116–150 (cit. on p. 146).

[Sun+16]   M. J. Sung et al. "High-mobility Naphthalene Diimide and Selenophene-vinylene-selenophene-based Conjugated Polymer: n-channel Organic Field-effect Transistors and Structure-property Relationship". In: *Advanced Functional Materials* 26.27 (2016), pp. 4984–4997 (cit. on pp. 162, 172).

[TA08]   D. M. Taylor and N. Alves. "Separating Interface State Response from Parasitic Effects in Conductance Measurements on Organic Metal-insulator-semiconductor Capacitors". In: *Journal of Applied Physics* 103.5 (2008), p. 054509 (cit. on p. 173).

[Ull+09]   M. Ullah, D. M. Taylor, R. Schwödiauer, H. Sitter, S. Bauer, N. S. Sariciftci, and T. B. Singh. "Electrical Response of Highly Ordered Organic Thin Film Metal-insulator-semiconductor Devices". In: *Journal of Applied Physics* 106.11 (2009), p. 114505 (cit. on p. 173).

References

[VC08]   S. L. M. Van Mensfoort and R. Coehoorn. "Effect of Gaussian Disorder on the Voltage Dependence of the Current Density in Sandwich-type Devices Based on Organic Semiconductors". In: *Physical Review B* 78.8 (2008), p. 085207 (cit. on pp. 53, 172).

[Vri+13b]   R. J. de Vries, a. Badinski, R. a. J. Janssen, and R. Coehoorn. "Extraction of the Materials Parameters That Determine the Mobility in Disordered Organic Semiconductors from the Current-voltage Characteristics: Accuracy and Limitations". In: *Journal of Applied Physics* 113.11 (2013), p. 114505 (cit. on p. 161).

[Yan+09]   H. Yan, Z. Chen, Y. Zheng, C. Newman, J. R. Quinn, F. Dötz, M. Kastler, and A. Facchetti. "A High-mobility Electron-transporting Polymer for Printed Transistors". In: *Nature* 457.7230 (2009), pp. 679–686 (cit. on p. 163).

Bibliography

[ABG05]   G. Alì, A. Bartel, and M. Günther. "Parabolic Differential-Algebraic Models in Electrical Network Design". In: *Multiscale Modeling & Simulation* 4.3 (2005), pp. 813–838 (cit. on p. 56).

[AFN19]   P. C. Africa, C. de Falco, and D. Natali. "A Note on Thermodynamically Consistent Flux Discretization". In: *In preparation* (2019) (cit. on pp. 23, 59, 93).

[AFP19]   P. C. Africa, C. de Falco, and S. Perotto. "Scalable Recovery-based Adaptation on Quadtree Meshes". In: *In preparation* (2019) (cit. on pp. 24, 97, 133).

[Afr+17]   P. C. Africa, C. de Falco, F. Maddalena, M. Caironi, and D. Natali. "Simultaneous Extraction of Density of States Width, Carrier Mobility and Injection Barriers in Organic Semiconductors". In: *Scientific Reports* 7.1 (2017), p. 3803 (cit. on pp. 23, 54, 55, 161).

[Alì+03]   G. Alì, A. Bartel, M. Günther, and C. Tischendorf. "Elliptic Partial Differential-Algebraic Multiphysics Models in Electrical Network Design". In: *Mathematical Models and Methods in Applied Sciences* 13.09 (2003), pp. 1261–1278 (cit. on p. 56).

[AM88]   N. W. Ashcroft and N. D. Mermin. *Solid State Physics*. Holt, Rinehart and Winston, New York, 1988 (cit. on p. 49).

[And78]   P. W. Anderson. "Local Moments and Localized States". In: *Reviews of Modern Physics* 50.2 (1978), p. 191 (cit. on p. 39).

[AR00]   A. M. Anile and V. Romano. "Hydrodynamical Modeling of Charge Carrier Transport in Semiconductors". In: *Meccanica* 35.3 (2000), pp. 249–296 (cit. on p. 38).

[AR99]   A. M. Anile and V. Romano. "Non Parabolic Band Transport in Semiconductors: Closure of the Moment Equations". In: *Continuum Mechanics and Thermodynamics* 11.5 (1999), pp. 307–325 (cit. on p. 38).

[Bar14]   S. D. Baranovskii. "Theoretical Description of Charge Transport in Disordered Organic Semiconductors". In: *Physica Status Solidi (b)* 251.3 (2014), pp. 487–525 (cit. on pp. 51, 171, 172).

Bibliography

[Bäs93] H. Bässler. "Charge Transport in Disordered Organic Photoconductors, a Monte Carlo Simulation Study". In: *Physica Status Solidi (b)* 175 (1993) (cit. on p. 44).

[BCC98] R. E. Bank, W. M. Coughran Jr, and L. C. Cowsar. "The Finite Volume Scharfetter-Gummel Method for Steady Convection Diffusion Equations". In: *Computing and Visualization in Science* 1.3 (1998), pp. 123–136 (cit. on pp. 93, 101).

[Ben+14] A. J. Ben-Sasson, M. Greenman, Y. Roichman, and N. Tessler. "The Mechanism of Operation of Lateral and Vertical Organic Field Effect Transistors". In: *Israel Journal of Chemistry* 54.5-6 (2014), pp. 568–585 (cit. on pp. 25, 29).

[BH82] A. N. Brooks and T. J. R. Hughes. "Streamline Upwind/petrov-galerkin Formulations for Convection Dominated Flows with Particular Emphasis on the Incompressible Navier-Stokes Equations". In: *Computer Methods in Applied Mechanics and Engineering* 32 (1982), pp. 199–259 (cit. on p. 144).

[BMM03] S. Bellavia, M. Macconi, and B. Morini. "An Affine Scaling Trust-region Approach to Bound-constrained Nonlinear Systems". In: *Applied Numerical Mathematics* 44.3 (2003), pp. 257–280 (cit. on p. 90).

[BMP89] F. Brezzi, L. D. Marini, and P. Pietra. "Two-dimensional Exponential Fitting and Applications to Drift-diffusion Models". In: *Siam Journal on Numerical Analysis* 26.6 (1989), pp. 1342–1355 (cit. on p. 101).

[Boc11] P. Bochev. *Control Volume Finite Element Method with Multidimensional Edge Element Scharfetter-Gummel Upwinding. Part 1. Formulation*. Tech. rep. Sandia National Laboratories, 2011 (cit. on p. 93).

[Bou+09] M. Bouhassoune, S. L. M. v. Mensfoort, P. A. Bobbert, and R. Coehoorn. "Carrier-density and Field-dependent Charge-carrier Mobility in Organic Semiconductors with Correlated Gaussian Disorder". In: *Organic Electronics: Physics, Materials, Applications* 10.3 (2009), pp. 437–445 (cit. on pp. 44, 53, 171).

[BP11] P. Bochev and K. Peterson. *Control Volume Finite Element Method with Multidimensional Edge Element Scharfetter-Gummel Upwinding. Part 2. Computational Study*. Tech. rep. Sandia National Laboratories, 2011 (cit. on p. 93).

[BR81] R. E. Bank and D. J. Rose. "Global Approximate Newton Methods". In: *Numerische Mathematik* 37.2 (1981), pp. 279–295 (cit. on p. 88).

[BRG03] J. A. Barker, C. M. Ramsdale, and N. C. Greenham. "Modeling the Current-voltage Characteristics of Bilayer Polymer Photovoltaic Devices". In: *Physical Review B* 67.7 (2003), p. 075205 (cit. on p. 55).

[BS90]   P. N. Brown and Y. Saad. "Hybrid Krylov Methods for Nonlinear Systems of Equations". In: *SIAM Journal on Scientific and Statistical Computing* 11.3 (1990), pp. 450–481 (cit. on pp. 87, 91).

[BSF02]   L. Bürgi, H. Sirringhaus, and R. H. Friend. "Noncontact Potentiometry of Polymer Field-effect Transistors". In: *Applied Physics Letters* 80.16 (2002), pp. 2913–2915 (cit. on p. 162).

[BSF09]   S. Braun, W. R. Salaneck, and M. Fahlman. "Energy-level Alignment at Organic/metal and Organic/organic Interfaces". In: *Advanced Materials* 21.14-15 (2009), pp. 1450–1472 (cit. on pp. 162, 169).

[Buc+15]   S. G. Bucella, A. Luzio, E. Gann, L. Thomsen, C. R. McNeill, G. Pace, A. Perinot, Z. Chen, A. Facchetti, and M. Caironi. "Macroscopic and High-throughput Printing of Aligned Nanostructured Polymer Semiconductors for Mhz Large-area Electronics". In: *Nature Communications* 6 (2015), p. 8394 (cit. on p. 163).

[Bür+03]   L. Bürgi, T. J. Richards, R. H. Friend, and H. Sirringhaus. "Close Look at Charge Carrier Injection in Polymer Field-effect Transistors". In: *Journal of Applied Physics* 94.9 (2003), pp. 6129–6137 (cit. on p. 162).

[But16]   J. C. Butcher. *Numerical Methods for Ordinary Differential Equations*. John Wiley & Sons, 2016 (cit. on p. 76).

[BWG11]   C. Burstedde, L. C. Wilcox, and O. Ghattas. "`p4est`: Scalable Algorithms for Parallel Adaptive Mesh Refinement on Forests of Octrees". In: *SIAM Journal on Scientific Computing* 33.3 (2011), pp. 1103–1133 (cit. on pp. 97, 99).

[Cai+10]   M. Caironi, C. Newman, J. R. Moore, D. Natali, H. Yan, a. Facchetti, and H. Sirringhaus. "Efficient Charge Injection from a High Work Function Metal in High Mobility N-type Polymer Field-effect Transistors". In: *Applied Physics Letters* 96.18 (2010), p. 183303 (cit. on p. 164).

[Căt05]   E. Cătinaş. "The Inexact, Inexact Perturbed, and Quasi-Newton Methods Are Equivalent Models". In: *Mathematics of Computation* 74.249 (2005), pp. 291–301 (cit. on p. 81).

[CB12]   R. Coehoorn and P. A. Bobbert. "Effects of Gaussian Disorder on Charge Carrier Transport and Recombination in Organic Semiconductors". In: *Physica Status Solidi (a)* 209.12 (2012), pp. 2354–2377 (cit. on pp. 38, 172).

[Cha+10]   J.-F. Chang, M. C. Gwinner, M. Caironi, T. Sakanoue, and H. Sirringhaus. "Conjugated-polymer-based Lateral Heterostructures Defined by High Resolution Photolithography". In: *Advanced Functional Materials* 20.17 (2010), pp. 2825–2832 (cit. on p. 173).

[Cho+14]   W. Choi, T. Miyakai, T. Sakurai, A. Saeki, M. Yokoyama, and S. Seki. "Non-contact, Non-destructive, Quantitative Probing of Interfacial Trap Sites for Charge Carrier Transport at Semiconductor-insulator Boundary". In: *Applied Physics Letters* 105.3, 033302 (July 22, 2014) (cit. on p. 51).

[CN15]   M. Caironi and Y.-Y. Noh. *Large Area and Flexible Electronics*. Wiley–VCH, 2015 (cit. on p. 25).

[Coe+05]   R. Coehoorn, W. F. Pasveer, P. A. Bobbert, and M. A. J. Michels. "Charge-carrier Concentration Dependence of the Hopping Mobility in Organic Materials with Gaussian Disorder". In: *Physical Review B* 72.15 (15 2005), p. 155206 (cit. on pp. 53, 162).

[CV17]   J. Chen and C. Vuik. "Globalization Technique for Projected Newton-Krylov Methods". In: *International Journal for Numerical Methods in Engineering* 110.7 (2017), pp. 661–674 (cit. on p. 88).

[Deu11]   P. Deuflhard. *Newton Methods for Nonlinear Problems: Affine Invariance and Adaptive Algorithms*. Vol. 35. Springer Science & Business Media, 2011 (cit. on p. 81).

[DIM17]   A. De Brauer, A. Iollo, and T. Milcent. "A Cartesian Scheme for Compressible Multimaterial Hyperelastic Models with Plasticity". In: *Communications in Computational Physics* 22.5 (2017), pp. 1362–1384 (cit. on p. 109).

[DM74]   J. E. Dennis and J. J. Moré. "A Characterization of Superlinear Convergence and Its Application to Quasi-Newton Methods". In: *Mathematics of Computation* 28.126 (1974), pp. 549–560 (cit. on p. 85).

[DM77]   J. E. Dennis Jr and J. J. Moré. "Quasi-Newton Methods, Motivation and Theory". In: *SIAM Review* 19.1 (1977), pp. 46–89 (cit. on p. 83).

[ES99]   A. Einstein and M. von Smoluchowski. "Untersuchungen über Die Theorie Der Brownschen Bewegung/abhandlungen über Die Brownsche Bewegung Und Verwandte Erscheinungen". In: *Harri Deutsch, Frankfurt* 3 (1999) (cit. on p. 50).

[EW94]   S. C. Eisenstat and H. F. Walker. "Globally Convergent Inexact Newton Methods". In: *SIAM Journal on Optimization* 4.2 (1994), pp. 393–422 (cit. on p. 85).

[EW96]   S. C. Eisenstat and H. F. Walker. "Choosing the Forcing Terms in an Inexact Newton Method". In: *SIAM Journal on Scientific Computing* 17.1 (1996), pp. 16–32 (cit. on p. 86).

[Far+18]   P. Farrell, M. Patriarca, J. Fuhrmann, and T. Koprucki. "Comparison of Thermodynamically Consistent Charge Carrier Flux Discretizations for Fermi-Dirac and Gauss-Fermi Statistics". In: *Optical and Quantum Electronics* 50.2 (2018), p. 101 (cit. on p. 60).

[FDS09]   M. H. Flamm, S. L. Diamond, and T. Sinno. "Lattice Kinetic Monte Carlo Simulations of Convective-diffusive Systems". In: *The Journal of Chemical Physics* 130.9 (2009), p. 094904 (cit. on p. 147).

[FO09]   C. de Falco and E. O'Riordan. "A Patched Mesh Method for Singularly Perturbed Reaction-diffusion Equations". In: *BAIL 2008-Boundary and Interior Layers*. Springer, 2009, pp. 117–127 (cit. on p. 134).

[FO10]   C. de Falco and E. O'Riordan. "Interior Layers in a Reaction-Diffusion Equation with a Discontinuous Diffusion Coefficient". In: *International Journal of Numerical Analysis & Modeling* 7.3 (2010), pp. 444–461 (cit. on p. 137).

[FT09]   J. A. Freire and C. Tonezer. "Density of States and Energetic Correlation in Disordered Molecular Systems Due to Induced Dipoles". In: *The Journal of Chemical Physics* 130.13, 134901 (Apr. 1, 2009) (cit. on p. 51).

[Fuh15]   J. Fuhrmann. "Comparison and Numerical Treatment of Generalised Nernst-Planck Models". In: *Computer Physics Communications* 196 (2015), pp. 166–178 (cit. on p. 60).

[Gri05a]   D. J. Griffiths. *Introduction to Electrodynamics*. AAPT, 2005 (cit. on p. 64).

[Gri05b]   D. J. Griffiths. *Introduction to Quantum Mechanics*. Pearson Education India, 2005 (cit. on p. 39).

[GS06]   R. Gusmeroli and A. S. Spinelli. "Accurate Boundary Integral Calculation in Semiconductor Device Simulation". In: *IEEE Transactions on Electron Devices* 53.7 (2006), pp. 1730–1733 (cit. on pp. 56, 57).

[GS55]   D. N. de G. Allen and R. V. Southwell. "Relaxation Methods Applied to Determine the Motion, in Two Dimensions, of a Viscous Fluid Past a Fixed Cylinder". In: *The Quarterly Journal of Mechanics and Applied Mathematics* 8.2 (1955), pp. 129–145 (cit. on p. 101).

[Hec11]   J. Hecht. *Understanding Lasers: An Entry-level Guide*. Vol. 21. John Wiley & Sons, 2011 (cit. on p. 38).

[HNW87]   E. Hairer, S. P. Norsett, and G. Wanner. *Solving Ordinary Differential Equations I, Computational Mathematics, Vol. 8*. 1987 (cit. on p. 79).

[Hug+00]   T. J. R. Hughes, G. Engel, L. Mazzei, and M. G. Larson. "The Continuous Galerkin Method Is Locally Conservative". In: *Journal of Computational Physics* 163.2 (2000), pp. 467–488 (cit. on pp. 56, 57).

[Hul+04]   I. N. Hulea, H. B. Brom, A. J. Houtepen, D. Vanmaekelbergh, J. J. Kelly, and E. A. Meulenkamp. "Wide Energy-window View on the Density of States and Hole Mobility in Poly(p-phenylene Vinylene)". In: *Physical Review Letters* 93.16, 166601 (Oct. 15, 2004) (cit. on p. 51).

[Jac99]   J. D. Jackson. *Classical Electrodynamics*. 3rd ed. John Wiley & Sons, 1999 (cit. on p. 45).

[Jer96]   J. W. Jerome. *Analysis of Charge Transport: A Mathematical Study of Semiconductor Devices*. 1996 (cit. on p. 38).

[Jun+07]   K.-D. Jung, C. A. Lee, D.-W. Park, B.-G. Park, H. Shin, and J. D. Lee. "Admittance Measurements on Ofet Channel and Its Modeling with R-c Network". In: *IEEE Electron Device Letters* 28.3 (2007), pp. 204–206 (cit. on p. 173).

[Jun+08]   K.-D. Jung, Y. C. Kim, B.-J. Kim, B.-G. Park, H. Shin, and J. D. Lee. "An Analytic Current-voltage Equation for Top-contact Organic Thin Film Transistors Including the Effects of Variable Series Resistance". In: *Japanese Journal of Applied Physics* 47.4S (2008), p. 3174 (cit. on pp. 163, 164, 176).

[Kat14]   S. Katsuaki. *Introduction to Printed Electronics*. Springer New York, 2014 (cit. on p. 25).

[Kax03]   E. Kaxiras. *Atomic and Electronic Structure of Solids*. Cambridge University Press, 2003 (cit. on p. 38).

[KB15]   A. Köhler and H. Bässler. *Electronic Processes in Organic Semiconductors: An Introduction*. John Wiley & Sons, 2015 (cit. on p. 47).

[Kel03]   C. T. Kelley. *Solving Nonlinear Equations with Newton's Method*. Vol. 1. Siam, 2003 (cit. on p. 87).

[KG13]   T. Koprucki and K. Gärtner. "Discretization Scheme for Drift-diffusion Equations with Strong Diffusion Enhancement". In: *Optical and Quantum Electronics* 45.7 (2013), pp. 791–796 (cit. on p. 59).

[Kit08]   C. Kittel. *Introduction to Solid State Physics*. Wiley, 2008 (cit. on p. 48).

[KK04]   D. A. Knoll and D. E. Keyes. "Jacobian-free Newton-Krylov Methods: A Survey of Approaches and Applications". In: *Journal of Computational Physics* 193.2 (2004), pp. 357–397 (cit. on p. 88).

[KKN14]   B. Kumar, B. K. Kaushik, and Y. S. Negi. "Perspectives and Challenges for Organic Thin Film Transistors: Materials, Devices, Processes and Applications". In: *Journal of Materials Science: Materials in Electronics* 25.1 (2014), pp. 1–30 (cit. on p. 30).

[Kna+10] E. Knapp, R. Häusermann, H. U. Schwarzenbach, and B. Ruhstaller. "Numerical Simulation of Charge Transport in Disordered Organic Semiconductor Devices". In: *Journal of Applied Physics* 108.5 (2010), p. 054504 (cit. on p. 54).

[Koc07]   N. Koch. "Organic Electronic Devices and Their Functional Interfaces". In: *ChemPhysChem* 8.10 (2007), pp. 1438–1455 (cit. on p. 162).

[Kop+14] T. Koprucki, M. Kantner, J. Fuhrmann, and K. Gärtner. "On Modifications of the Scharfetter-Gummel Scheme for Drift-diffusion Equations with Fermi-like Statistical Distribution Functions". In: *Numerical Simulation of Optoelectronic Devices, 2014.* 2014, pp. 155–156 (cit. on p. 59).

[Kop+15] T. Koprucki, N. Rotundo, P. Farrell, D. H. Doan, and J. Fuhrmann. "On Thermodynamic Consistency of a Scharfetter-Gummel Scheme Based on a Modified Thermal Voltage for Drift-diffusion Equations with Diffusion Enhancement". In: *Optical and Quantum Electronics* 47.6 (2015), pp. 1327–1332 (cit. on p. 59).

[Kwo+12] S. Kwon, K.-R. Wee, J. W. Kim, C. Pac, and S. O. Kang. "Effects of Intermolecular Interaction on the Energy Distribution of Valance Electronic States of a Carbazole-based Material in Amorphous Thin Films". In: *The Journal of Chemical Physics* 136.20, 204706 (2012) (cit. on p. 51).

[MA60]   A. Miller and E. Abrahams. "Impurity Conduction at Low Concentrations". In: *Physical Review* 120.3 (1960), p. 745 (cit. on p. 43).

[Mad+15] F. Maddalena, C. de Falco, M. Caironi, and D. Natali. "Assessing the Width of Gaussian Density of States in Organic Semiconductors". In: *Organic Electronics* 17 (2015), pp. 304–318 (cit. on pp. 30, 47, 51, 161–164, 168, 170, 173, 175, 177).

[Mad95]   O. Madelung. *Introduction to Solid-state Theory*. Vol. 2. Springer Science & Business Media, 1995 (cit. on p. 49).

Bibliography

[Mai+06]   G. Maisano, S. Micheletti, S. Perotto, and C. L. Bottasso. "On Some New Recovery-based a Posteriori Error Estimators". In: *Computer Methods in Applied Mechanics and Engineering* 195.37 (2006), pp. 4794–4815. ISSN: 0045-7825 (cit. on pp. 104, 105).

[Mar+09]   N. G. Martinelli, M. Savini, L. Muccioli, Y. Olivier, F. Castet, C. Zannoni, D. Beljonne, and J. Cornil. "Modeling Polymer Dielectric/pentacene Interfaces: On the Role of Electrostatic Energy Disorder on Charge Carrier Mobility". In: *Advanced Functional Materials* 19.20 (2009), pp. 3254–3261 (cit. on p. 51).

[Mar86]   P. A. Markowich. *The Stationary Semiconductor Device Equations*. Vol. 1. Springer Science & Business Media, 1986 (cit. on p. 46).

[Mei+06]   K. D. Meisel, W. F. Pasveer, J. Cottaar, C. Tanase, R. Coehoorn, P. A. Bobbert, P. W. M. Blom, D. M. de Leeuw, and M. A. J. Michels. "Charge-carrier Mobilities in Disordered Semiconducting Polymers: Effects of Carrier Density and Electric Field". In: *Physica Status Solidi (c)* 3.2 (2006), pp. 267–270 (cit. on p. 43).

[MN15]   S. Mandal and Y.-Y. Noh. "Printed Organic Thin-Film Transistor-based Integrated Circuits". In: *Semiconductor Science and Technology* 30.6 (2015), p. 064003 (cit. on p. 29).

[MRS90]   P. A. Markowich, C. A. Ringhofer, and C. Schmeiser. *Semiconductor Equations*. 1990 (cit. on p. 38).

[MW94]   J. J. H. Miller and S. Wang. "An Analysis of the Scharfetter-Gummel Box Method for the Stationary Semiconductor Device Equations". In: *Rairo-modélisation Mathématique Et Analyse Numérique* 28.2 (1994), pp. 123–140 (cit. on p. 93).

[MZ88]   P. A. Markowich and M. A. Zlámal. "Inverse-average-type Finite Element Discretizations of Selfadjoint Second-order Elliptic Problems". In: *Mathematics of Computation* 51.184 (1988), pp. 431–449 (cit. on p. 101).

[NC12]   D. Natali and M. Caironi. "Charge Injection in Solution-processed Organic Field-effect Transistors: Physics, Models and Characterization Methods". In: *Advanced Materials* 24.11 (2012), pp. 1357–1387 (cit. on pp. 163, 164, 176).

[Néd80]   J.-C. Nédélec. "Mixed Finite Elements in $\mathbb{R}^3$". In: *Numerische Mathematik* 35.3 (1980), pp. 315–341 (cit. on p. 105).

[OEA]   *OE - A Roadmap for Organic and Printed Electronics, 6th Edition*. White Paper. Organic and Printed Electronics Association, 2015. URL: http://www.oe-a.org (cit. on p. 25).

204

[OHB12]   J. O. Oelerich, D. Huemmer, and S. D. Baranovskii. "How to Find Out the Density of States in Disordered Organic Semiconductors". In: *Physical Review Letters* 108.22, 226403 (May 29, 2012), p. 226403 (cit. on pp. 157, 171).

[OKH14]   M. Oehzelt, N. Koch, and G. Heimel. "Organic Semiconductor Density of States Controls the Energy Level Alignment at Electrode Interfaces". In: *Nature Communications* 5 (2014), p. 4174 (cit. on p. 162).

[Pat+18]   M. Patriarca, P. Farrell, J. Fuhrmann, and T. Koprucki. "Highly Accurate Quadrature-based Scharfetter-Gummel Schemes for Charge Transport in Degenerate Semiconductors". In: *Computer Physics Communications* (2018) (cit. on p. 60).

[Poe+13]   C. Poelking, E. Cho, A. Malafeev, V. Ivanov, K. Kremer, C. Risko, J. Brédas, and D. Andrienko. "Characterization of Charge-carrier Transport in Semicrystalline Polymers: Electronic Couplings, Site Energies, and Charge-carrier Dynamics in Pbttt". In: *The Journal of Physical Chemistry C* 117.4 (2013), pp. 1633–1640 (cit. on p. 51).

[Pow70]   M. J. D. Powell. "A Hybrid Method for Nonlinear Equations". In: *Numerical Methods for Nonlinear Algebraic Equations* (1970) (cit. on p. 91).

[PS99]   M. Pope and C. E. Swenberg. *Electronic Processes in Organic Crystals and Polymers*. Oxford University Press on Demand, 1999 (cit. on p. 41).

[RBI18]   A. Raeli, M. Bergmann, and A. Iollo. "A Finite-difference Method for the Variable Coefficient Poisson Equation on Hierarchical Cartesian Meshes". In: *Journal of Computational Physics* 355 (2018), pp. 59–77 (cit. on pp. 140, 143).

[RE11]   M. Raja and B. Eccleston. "The Significance of Debye Length in Disordered Doped Organic Devices". In: *Journal of Applied Physics* 110.11, 114524 (Dec. 13, 2011) (cit. on p. 51).

[Riv+11]   J. Rivnay, R. Noriega, J. E. Northrup, R. J. Kline, M. F. Toney, and A. Salleo. "Structural Origin of Gap States in Semicrystalline Polymers and the Implications for Charge Transport". In: *Physical Review B* 83.12, 121306 (Mar. 16, 2011) (cit. on p. 51).

[SBS81]   G. Schönherr, H. Bässler, and M. Silver. "Dispersive Hopping Transport Via Sites Having a Gaussian Distribution of Energies". In: *Philosophical Magazine B* 44.1 (1981), pp. 47–61 (cit. on p. 44).

[Sch+12]   D. Schillinger, L. Dede', M. A. Scott, J. A. Evans, M. J. Borden, E. Rank, and T. J. R. Hughes. "An Isogeometric Design-through-analysis Methodology Based on Adaptive Hierarchical Refinement of Nurbs, Immersed Boundary Methods, and T-spline Cad Surfaces". In: *Computer Methods in Applied Mechanics and Engineering* 249 (2012), pp. 116–150 (cit. on p. 146).

[Sch70]   L. K. Schubert. "Modification of a Quasi-Newton Method for Nonlinear Equations with a Sparse Jacobian". In: *Mathematics of Computation* 24.109 (1970), pp. 27–30 (cit. on p. 85).

[Sel12]   S. Selberherr. *Analysis and Simulation of Semiconductor Devices*. Springer Science & Business Media, 2012 (cit. on p. 48).

[SG69]   D. L. Scharfetter and H. K. Gummel. "Large-signal Analysis of a Silicon Read Diode Oscillator". In: *IEEE Transactions on Electron Devices* 16.1 (1969), pp. 64–77 (cit. on p. 95).

[Sha99]   H. Shao. "Numerical Analysis of Meshing and Discretization for Anisotropic Convection-diffusion Equations with Applications". PhD thesis. Duke University, 1999 (cit. on p. 94).

[Sir14]   H. Sirringhaus. "25th Anniversary Article: Organic Field-Effect Transistors: The Path beyond Amorphous Silicon". In: *Advanced Materials* 26.9 (2014), pp. 1319–1335 (cit. on pp. 29, 31, 32).

[SM99]   J. C. Scott and G. G. Malliaras. "Charge Injection and Recombination at the Metal-organic Interface". In: *Chemical Physics Letters* 299.2 (1999), pp. 115–119 (cit. on p. 55).

[SS86]   Y. Saad and M. H. Schultz. "Gmres: A Generalized Minimal Residual Algorithm for Solving Nonsymmetric Linear Systems". In: *SIAM Journal on Scientific and Statistical Computing* 7.3 (1986), pp. 856–869 (cit. on p. 88).

[Sun+16]   M. J. Sung et al. "High-mobility Naphthalene Diimide and Selenophene-vinylene-selenophene-based Conjugated Polymer: n-channel Organic Field-effect Transistors and Structure-property Relationship". In: *Advanced Functional Materials* 26.27 (2016), pp. 4984–4997 (cit. on pp. 162, 172).

[TA08]   D. M. Taylor and N. Alves. "Separating Interface State Response from Parasitic Effects in Conductance Measurements on Organic Metal-insulator-semiconductor Capacitors". In: *Journal of Applied Physics* 103.5 (2008), p. 054509 (cit. on p. 173).

[TM11]   A. K. Tripathi and Y. N. Mohapatra. "Correlation of Photocurrent and Electroabsorption Spectra and Their Temperature Dependence for Conjugated Light Emitting Polymers: The Origin of the Corresponding Density of States". In: *Physical Review B* 84.20, 205213 (Nov. 18, 2011) (cit. on p. 51).

[Tun14]   R. T. Tung. "The Physics and Chemistry of the Schottky Barrier Height". In: *Applied Physics Reviews* 1.1 (2014), p. 011304 (cit. on p. 54).

[Ull+09]   M. Ullah, D. M. Taylor, R. Schwödiauer, H. Sitter, S. Bauer, N. S. Sariciftci, and T. B. Singh. "Electrical Response of Highly Ordered Organic Thin Film Metal-insulator-semiconductor Devices". In: *Journal of Applied Physics* 106.11 (2009), p. 114505 (cit. on p. 173).

[VC08]   S. L. M. Van Mensfoort and R. Coehoorn. "Effect of Gaussian Disorder on the Voltage Dependence of the Current Density in Sandwich-type Devices Based on Organic Semiconductors". In: *Physical Review B* 78.8 (2008), p. 085207 (cit. on pp. 53, 172).

[VDM73]   R. J. Van Overstraeten, H. J. DeMan, and R. P. Mertens. "Transport Equations in Heavy Doped Silicon". In: *IEEE Transactions on Electron Devices* 20.3 (1973), pp. 290–298 (cit. on pp. 59, 60).

[Vri+13a]   R. J. de Vries, A. Badinski, R. A. J. Janssen, and R. Coehoorn. "Extraction of the Materials Parameters That Determine the Mobility in Disordered Organic Semiconductors from the Current-voltage Characteristics: Accuracy and Limitations". In: *Journal of Applied Physics* 113.11, 114505 (Mar. 19, 2013) (cit. on p. 51).

[Vri+13b]   R. J. de Vries, a. Badinski, R. a. J. Janssen, and R. Coehoorn. "Extraction of the Materials Parameters That Determine the Mobility in Disordered Organic Semiconductors from the Current-voltage Characteristics: Accuracy and Limitations". In: *Journal of Applied Physics* 113.11 (2013), p. 114505 (cit. on p. 161).

[VW09]   N. Vukmirović and L.-W. Wang. "Charge Carrier Motion in Disordered Conjugated Polymers: A Multiscale Ab Initio Study". In: *Nano Letters* 9.12 (Nov. 13, 2009), pp. 3996–4000 (cit. on p. 51).

[VW11]   N. Vukmirović and L.-W. Wang. "Density of States and Wave Function Localization in Disordered Conjugated Polymers: A Large Scale Computational Study". In: *The Journal of Physical Chemistry B* 115.8 (Feb. 3, 2011), pp. 1792–1797 (cit. on p. 51).

Bibliography

[Wei+06]   D. S. Weiss, M. Abkowitz, S. Kasap, and P. Capper. *Handbook of Electronic and Photonic Materials*. Springer, 2006. Chap. 9 (cit. on pp. 39, 40, 51).

[Wey17]   L. Weynans. "Convergence of a Cartesian Method for Elliptic Problems with Immersed Interfaces". PhD thesis. INRIA Bordeaux; Univ. Bordeaux, 2017 (cit. on p. 109).

[Wey18]   L. Weynans. "Super-convergence in Maximum Norm of the Gradient for the Shortley-Weller Method". In: *Journal of Scientific Computing* 75.2 (2018), pp. 625–637 (cit. on p. 107).

[Yan+09]   H. Yan, Z. Chen, Y. Zheng, C. Newman, J. R. Quinn, F. Dötz, M. Kastler, and A. Facchetti. "A High-mobility Electron-transporting Polymer for Printed Transistors". In: *Nature* 457.7230 (2009), pp. 679–686 (cit. on p. 163).

[Zho+14]   K. Zhou, H. Dong, H.-l. Zhang, and W. Hu. "High Performance N-type and Ambipolar Small Organic Semiconductors for Organic Thin Film Transistors". In: *Physical Chemistry Chemical Physics* 16.41 (2014), pp. 22448–22457 (cit. on p. 26).

[Zlá86]   M. A. Zlámal. "Finite Element Solution of the Fundamental Equations of Semiconductor Devices. I". In: *Mathematics of Computation* 46.173 (1986), pp. 27–43 (cit. on p. 101).